Modelling and Performance Evaluation of a Pseudo-Random Impulse Sequence for *In situ* Parameter Estimation in Energy Applications

by

Fredrick Mukundi Mwaniki

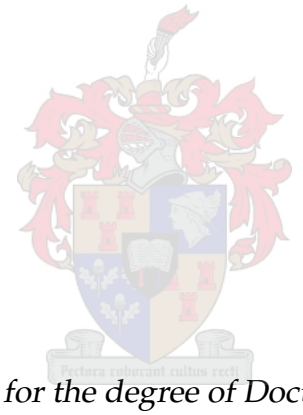

Dissertation presented for the degree of Doctor of Philosophy in the Faculty of Engineering at Stellenbosch University

Supervisor: Prof. H. J. Vermeulen

March 2020

Declaration

By submitting this dissertation electronically, I declare that the entirety of the work contained therein is my own, original work, that I am the sole author thereof (save to the extent explicitly otherwise stated), that reproduction and publication thereof by Stellenbosch University will not infringe any third party rights and that I have not previously in its entirety or in part submitted it for obtaining any qualification.

Date: March 2020 .....

Abstract

Modelling and Performance Evaluation of a Pseudo-Random Impulse Sequence for *In situ* Parameter Estimation in Energy Applications

FM Mwaniki

Promotor: Prof. H. J. Vermeulen
Faculty of Engineering
Department of Electrical & Electronic Engineering

Dissertation: PhD (Electrical Engineering)

March 2020

System identification and parameter estimation procedures involve the use of experiments to find an accurate model for a target s ystem. These experiments typically involve excitation of the target system with a perturbation signal and recording and analysing the system's input and output waveforms. The time- and frequency-domain characteristics of the perturbation signal can have a significant influence on the system response and the accuracy of the parameter estimation experiment. An optimal perturbation signal should persistently excite all the relevant modes of the target system. Although a significant amount of research has been carried out on perturbation signals, the case of a suitable signal for high power, high voltage, *in situ* applications has not been thoroughly investigated.

This study discusses the novel concept of a Pseudo-Random Impulse Sequence (PRIS) as a wideband perturbation signal for *in situ* parameter estimation in energy field applications. The time- and frequency-domain properties of the PRIS are analyzed and the effects of the various model parameters, including the time constants, sequence length and clock frequency are investigated through mathematical analysis and simulations to determine the suitability of the signal for system identification and parameter estimation a pplications. It is demonstrated that the time- and frequency-domain properties of the PRIS can be controlled by manipulating the associated clock frequency, time constants and sequence length. This controllability of the PRIS is highly desirable as it allows the user to focus the perturbation energy to suit a wide range of applications.

Perturbation signals for use in the high power applications should be generated efficiently using circuit topologies that are compatible with the associated high voltage environment. A perturbation source circuit topology for generating the proposed PRIS signal is developed and analysed. It is shown that the PRIS can be generated using a compact and efficient design with highly reduced average losses compared to conventional sources such as the Pseudo-Random Binary Sequence (PRBS) topologies. The circuit topology is, furthermore, demonstrated to be optimal for *in situ* high power, high voltage applications. The circuit design considerations for the proposed PRIS source are discussed in detail.

Accurate information on the grid impedance characteristics, especially from a particular Point of Connection (POC) is essential for harmonic penetration studies, compliance with harmonic limits for the grid integration of renewable energy sources, transient analysis, harmonic filter design and controller design. The performance of the PRIS signal is demonstrated successfully for an *in situ* case study application involving wideband characterization of the Thevenin equivalent grid impedance of a supply network. A novel experimental approach is proposed to improve the grid impedance estimation results by minimizing the effects of the non-stationary nature of the grid.

Uittreksel

Modellering en prestasiebeoordeling van 'n pseudo-ewekansige impulsreeks vir textit In situ Parameterberaming in energietoepassings

FM Mwaniki
Promotor: Prof. H. J. Vermeulen
Fakulteit Ingenieurswese
Departement Elektriese & Elektroniese Ingenieurswese

Proefskrif: PhD (Elektriese Ingenieurswese)
Maart 2020

Stelselidentifikasie en parameterberamingsprosedures behels die gebruik van eksperimente om 'n akkurate model vir 'n teikensisteem te vind. Hierdie eksperimente behels tipies die aandryf van die teikenstelsel met 'n steursein en die opname en ontleding van die stelsel se intree- en uittreegolfvorms. Die tyd- en frekwensiegebied eienskappe van die steursein kan 'n beduidende invloed hê op die stelselweergawe en die akkuraatheid van die parameterestimasie eksperiment. 'n Optimale steursein moet al die relevante modusse van die teikenstelsel volhoudend aktiveer. Alhoewel 'n beduidende hoeveelheid navorsing oor steurseine uitgevoer is, is die geval van 'n geskikte sein vir hoëdrywing, hoogspanning, in situ toepassings nie deeglik ondersoek nie. In hierdie studie word die nuwe konsep van 'n Kwasie-Lukrake Impuls Reeks (KLIR) as 'n wyeband steursein vir in situ parameter afskatting in energie toepassings bespreek. Die tyd- en frekwensiegebied eienskappe van die KLIR word ontleed en die uitwerking van die verskillende modelparameters, insluitende die tydkonstantes, reekslengte en klokfrekwensie, word ondersoek deur wiskundige analise en simulasies om die geskiktheid van die sein vir stelselidentifisering en parameterafskatting te bepaal. Daar word gedemonstreer dat die tyd- en frekwensiegebied eienskappe van die KLIR beheer kan word deur die gepaardgaande klokfrekwensie, tydkonstantes en reekslengte te manipuleer. Hierdie beheerbaarheid van die KLIR is uiters wenslik, aangesien dit die gebruiker in staat stel om die steurenergie te fokus om 'n wye verskeidenheid toepassings te pas.

Steurseine vir gebruik in die hoëdrywing toepassings moet doeltreffend opgewek word deur gebruik te maak van stroombaantopologieë wat versoenbaar is met die gepaardgaande hoogspanningsomgewing. 'n stroombaantopologie vir die opwekking van die voorgestelde KLIR sein word ontwikkel en ontleed. Daar word aangetoon dat die KLIR opgewek kan word met 'n kompakte en effektiewe ontwerp met hoogs verminderde gemiddelde verliese in vergelyking met konvensionele bronne soos die Kwasi-Lukrake Binêre Reeks (KLBR) topologieë. Verder word aangetoon dat die stroombaantopologie optimaal is vir in situ hoëdrywing, hoogspanning toepassings. Die stroombaan ontwerpsoorwegings vir die voorgestelde KLIR bron word breedvoerig bespreek.

Akkurate inligting oor die netwerk impedansie-eienskappe, veral vanuit 'n bepaalde punt van verbinding, is noodsaaklik vir harmoniese penetrasiestudies, die nakoming van harmoniese limiete vir die netwerkintegrasie van hernubare energiebronne, dinamiese analise, harmoniese filterontwerp en die ontwerp van beheerstelsels. Die gedrag van die KLIR sein word suksesvol gedemonstreer vir 'n in situ gevallestudie toepassing wat die wyebandkarakterisering van die Thevenin ekwivalente netwerkimpedansie van 'n toevoernetwerk behels. 'n Nuwe eksperimentele benadering word voorgestel om die afskatting van die netwerkimpedansie te verbeter deur die uitwerking van die nie-stasionêre aard van die netwerk te minimeer.

Acknowledgements

I would like to express my gratitude towards the following people whose support has been of great value to me:

- Prof. H. J. Vermeulen, my supervisor, for the remarkable guidance, advice and support.
- Colleagues especially Nelius Bekker, Willem Jordaan, Maarten Kamper, Arno Bernard and Herman Kamper for the motivation and willingness to assist whenever I needed help.
- Petro Petzer, André Swart, Murray Jumat and Brent Gideons for the assistance in the laboratory.
- My parents and siblings for the prayers and support I can always count on.
- Salome, Hope and Malaika for your love, support and understanding.
- God for His blessings and guidance.

Contents

List of Figures

List of Tables

Acronyms

AC Alternating current. x, 9, 16–19, 70, 77

BNC Bayonet Neill Concelman. 73

DC Direct current. xi, 9, 13, 18, 19, 45, 49, 57, 60–62

DIBS Discrete Interval Binary Sequence. 2

FACTS Flexible AC Transmission Systems. 3, 4

FFT Fast Fourier Transform. 70

FPGA Field Programmable Gate Array. 58

FRA Frequency Response Analysis. 5, 11, 12

HV High Voltage. 1

LFSR Linear Feedback Shift Register. 14, 57

MLB Maximum Length Binary. 14

MV Medium Voltage. 1, 7

NSP Network Service Provider. 4

PCC Point of Common Coupling. 2, 3

POC Point of Connection. 4

PRBS Pseudo Random Binary Sequence. viii, x, xi, 2, 5, 6, 14, 33, 34, 38–45, 49, 51, 56–63, 101

PRIS Pseudo Random Impulse Sequence. viii–xii, 1, 5–7, 30, 32–34, 36, 38–65, 68, 69, 75, 77–81, 86, 89, 91, 96, 97, 99, 101, 102

PSD Power Spectral Density. 34, 35

PV photovoltaic. 2

QOS Quality of Supply. 2

RMS Root Mean Square. 10

RPPs Renewable Power Producers. 3

SNR Signal to Noise Ratio. 1, 2, 9

STATCOMs Static Synchronous Compensators. 3

SVCs Static VAR Compensators. 3

CHAPTER 1

Introduction

1.1 Overview

System identification is the field of mathematical modelling of systems from experimental data [1]. In the field of electrical energy, system identification, parameter estimation and digital signal processing techniques are typically used for modelling power system grid impedance and apparatus such as motors, transformers, generators, excitation systems and power converters [2], [3].

This dissertation discusses the characterisation and application of a novel wideband perturbation signal, namely the Pseudo-Random Impulse Sequence (PRIS), for application in high power, High Voltage (HV) *in situ* system identification and parameter estimation applications. The time- and frequency-domain properties of the PRIS signal are analyzed and a suitable perturbation source topology is proposed. The performance of the proposed signal is evaluated for a case study involving *in situ* system identification and parameter estimation to characterise a wideband grid impedance model for a rural Medium Voltage (MV) network.

1.2 Project motivation

The classical experimental methodologies used in system identification and parameter estimation applications typically involve the application of an excitation signal with suitable time-and frequency-domain properties. The input waveforms and system responses are recorded over a time interval for subsequent processing, using signal analysis and parameter estimation algorithms to extract the relevant model parameters [4], [5]. The perturbation signal is selected based on the dynamic responses and frequency responses of the target system, and it is generally acknowledged that the time- and frequency-domain properties of perturbation signal can have a notable influence on the accuracies of the estimated model parameters [6], [7].

An optimal perturbation signal should, ideally, persistently excite all relevant modes of the target system [1], [6]. The parameters that need to be considered in selecting a perturbation signal include bandwidth, Signal to Noise Ratio (SNR), dynamic range and frequency resolution [6], [8], [9]. The ability to control the time-and frequency-domain properties of a perturbation signal is highly desirable, as it allows for the excitation energy to be focussed on the frequency

band of interest. Applications involving electromagnetic equipment such as transformers, for instance, require that the low frequency components of the perturbation signal be limited to avoid core saturation effects [10].

An extensive range of excitation signals has been proposed in literature for wideband parameter estimation applications [4] - [10], [11], [12]. These signals include periodic signals such as the stepped sine, swept sine and multi-sine, transient signals such as the random burst and impulse signals, pseudo-random signals such as the PRBS, periodic noise and the Discrete Interval Binary Sequence (DIBS) and aperiodic signals such as the random noise signal. Many of these conventional perturbation signals used in the field of system identification and parameter estimation are, however, unsuitable for high power, high voltage applications, especially in the sense that the signals are unsuitable for *in situ* application and due to the inefficient and impractical nature of the associated source topologies.

In situ measurements, i.e. without disconnecting the device under test from service, are highly desirable in power system applications [10], [13]. It allows for the effects of operating conditions to be tracked, whilst interruption of the supply network is avoided and downtimes are minimized. This is particularly important in an application such as characterising network impedance. In some cases, *In situ* perturbation is also important in distributed generation, where islanding conditions need to be detected through impedance variations [11].

In high power, high voltage applications, the perturbation signal must, furthermore, have appropriate voltage and current levels relative to the ratings of the target system to ensure an acceptable SNR. This implies that it is essential that the signal is generated using a compact, energy-efficient circuit topology.

Increased energy demand and global environmental degradation concerns are giving rise to increasing penetration of renewable energy sources such as utility-size wind and solar photovoltaic (PV) generation [14]. These distributed power sources are typically interfaced to the power grid through power electronic converters [15]. Due to the inherent switching behaviour of power electronics converters, the current waveforms injected into the grid include harmonic components that are superimposed on the fundamental frequency component [3], [12]. These harmonic current emissions induce harmonic voltage distortion, which impacts negatively on the overall Quality of Supply (QOS).

The grid connection codes that apply for renewable energy systems, therefore, include compliance standards for the harmonic current emissions and harmonic voltage distortion allowed at the Point of Common Coupling (PCC) [16]. In South Africa, for instance, the NRS 084 standard provides guidance on the technical procedures to be followed for the connection of new generators and users of electricity, as well as performance evaluation of existing customers,

regarding harmonic distortion and voltage quality parameters [17], [18], [19].

The harmonic emissions associated with power-electronic converters can be mitigated by implementing active or passive harmonic filters. In practice, however, the performance of these filters are affected by the interaction between the filter circuits and the grid impedance. This interaction gives rise to complex series and/or parallel resonant circuit topologies. When a minimally damped resonant point in the system's impedance is excited by a harmonic current or a transient event, current and/or voltage amplification results. Overvoltages and overcurrents may lead to damage to equipment connected to the grid. The dynamic and frequency response characteristics of the grid impedance, furthermore, influence both the inner current control loop and voltage control loop of the inverters connected to the grid [15], [20]. In severe cases, the overvoltages and overcurrents can cause instability in inverter operation [12]. It is generally accepted that the wideband properties of the grid, as reflected at the PCC, are becoming increasingly complex as the penetration of non-linear loads on the demand side and grid-tied converters on the supply side increases. This is compounded by the increasing diversity of energy sources, the stochastic nature of renewable generation and the time-variance of modern networks.

A good understanding of the wideband grid impedance characteristics, especially at a PCC, is of particular importance for the following applications:

- *Harmonic filter design:* Passive and active filters are used extensively in modern power systems to mitigate harmonic distortion, especially in the context of the power converters associated with wind and solar PV renewable energy sources [21]. The design of these filters requires good insight into the wideband characteristics and time-dependent behaviour of the system impedance at the PCC [12], [22].

- *Controller design:* The design of controllers for power electronics systems, including converters and Flexible AC Transmission Systems (FACTS) devices such as Static Synchronous Compensators (STATCOMs) and Static VAR Compensators (SVCs), must take cognisance of the wideband properties of the system impedance to guarantee system stability and appropriate dynamic behavior [12], [20], [23], [24].

- *Grid code compliance for Renewable Power Producers (RPPs):* RPPs can demonstrate grid code compliance by conducting impedance measurements in their network with the view to ensure that the interaction with the grid impedance does not give rise to harmful resonant points [12], [22], [25]. The maximum impedance resonance should not exceed the required base harmonic impedance indicated in the grid code. In South Africa, for instance,

the grid code [17] states that the resulting impedance at the Point of Connection (POC) should not exceed 3 times the base harmonic impedance limit for any frequency below the 50th harmonic. In this case, therefore, the RPP may not connect equipment, e.g. capacitor banks, that will cause resonance of more than 3 times at the POC at any frequency. In this regard, the Network Service Provider (NSP) is required to make available sufficient information about the grid to allow the RPP to design for grid code compliance. This includes information such as the network topology of the various lines, transformers, reactors, capacitors, and other relevant equipment [17].

- *Design of protection systems:* The design of protection systems requires accurate knowledge of the system impedance at the fundamental frequency to determine short-circuit power [12].

- *Detecting islanding conditions:* System impedance can be used to detect islanding conditions in a network with distributed generation [11], [14], [20], [25]. During an islanding condition, a distributed generator feeds a local sub-grid, while the main grid is switched off. In this case, islanding can be detected through sudden impedance variation.

The grid impedance at the fundamental system frequency is typically determined by calculations based on the short-circuit power observed at a given voltage level. Wideband modelling of grid impedance, however, has received considerable attention in recent years [12], [14], [21] - [26]. Power system simulation software, such as DIgSILENT PowerFactory, represents a convenient tool to simulate the frequency responses of system impedance [12], [27]. The accuracy of computer-based power system studies is, however, highly dependent on the accuracies of the model topologies and parameter sets used to represent the system components, such as lines, cables, transformers, rotating machines, etc. In practice, manufacturer specified values are used often in these studies. Many crucial parameter values are, however, often not specified. The available parameter values may, furthermore, be inaccurate as parameters may change over time or with operating conditions [28].

The development of methodologies and procedures for estimating the parameters of wideband models of power system apparatus is therefore of major importance in the context of grid impedance frequency response studies. The grid topology is, furthermore, nonstationary in nature, especially due to the presence of dynamic loads and the dynamic nature of the power electronic systems associated with modern FACTS devices, which further complicates the simulation approach. *In situ* system identification and parameter estimation investigations are therefore of importance in characterising the wideband characteristics of grid impedance.

The wideband modelling of power transformers is not only of major importance in the context of the modelling the frequency domain characteristics of grid impedance but also for applications such as condition monitoring. The behaviour of power transformers under transient conditions, or at frequencies other than the nominal frequency, are complex. The frequency responses of a transformer are determined by equivalent circuit elements such as the leakage inductances, winding resistances, winding capacitances and the non-linear core components [29]. Frequency response measurements have, therefore, found extensive application in determining parameter values for wideband lumped parameter equivalent circuit models of power transformers, potential transformers and current transformers [30], [31], especially in power quality studies. Frequency Response Analysis (FRA) has, furthermore, been used extensively for condition monitoring of power transformers for power network reliability applications [30], [32], [33].

The FRA approach typically makes use of measured frequency responses of the primary and secondary input impedances under open-circuited and/or short-circuited conditions, primary to secondary, and secondary to primary transformation ratios, etc. It has been shown that FRA is suitable for detecting a range of problems, including winding displacement or deformation due to physical damage to a transformer.

1.3 Research focus

1.3.1 Research objectives

This investigation focuses on the analysis and performance evaluation of a novel perturbation signal, namely the Pseudo-Random Impulse Sequence (PRIS), for *in situ* application in the field of high power, high voltage system identification and parameter estimation studies. This gives rise to the following research objectives:

- *Mathematical modelling and analysis of the time-domain properties of the PRIS signal:* Time-domain models are developed for the unipolar and bipolar PRIS signals with reference to the classical impulse signal and the PRBS signal. The effects of the various time-domain model parameters, including the impulse time constants and PRBS clock frequency, are investigated through mathematical analysis and simulations with the view to determine the suitability of the signal for *in situ* system identification and parameter estimation applications.

- *Mathematical modelling and analysis of the frequency-domain properties of the PRIS signal:* The frequency-domain properties of the proposed perturbation signal are explored through

mathematical analysis and simulations with the view to determine the suitability of the signal for persistent excitation in wideband system identification and parameter estimation applications. The controllability of the frequency spectrum in comparison with existing perturbation signals is investigated.

- *Development of a perturbation source circuit topology that is optimal for in situ high power, high voltage applications:* An energy-efficient circuit topology is proposed and the performance of the circuit for *in situ* excitation of active systems is investigated. A detailed mathematical analysis of the perturbation source is presented and important design considerations identified.

- *Performance evaluation of the proposed PRIS signal and perturbation source for wideband characterisation of grid impedance:* The PRIS signal is applied *in situ* for wideband characterisation of the grid impedance of a supply network. The effects of harmonic voltage distortion and the non-stationary nature of the Thevenin equivalent grid model are investigated.

1.3.2 Original contributions

The original contributions associated with the research can be summarised as follows:

- *Introduction of the PRIS waveform as wideband perturbation signal for high power, high voltage applications:* The proposed PRIS signal represents a novel concept, that combines a PRBS gate signal with the classical impulse excitation waveform used extensively in high voltage engineering.

- *Time-domain model and analysis of the PRIS signal:* The time-domain properties of the PRIS signal have not been investigated in the literature. It is shown that the signal is highly suitable for *in situ* application in high power, high voltage environment.

- *Frequency-domain model and analysis of the PRIS signal:* The frequency-domain properties of the PRIS signal have not been investigated in the literature. It is shown that the power spectrum of the PRIS has a good degree of controllability in comparison with the classical PRBS and impulse signals, especially in the sense that the frequency spectrum can be manipulated by adjusting the impulse time constants and PRBS clock frequency to focus the spectral energy in the frequency band of interest.

- *Development and performance evaluation of a PRIS source circuit topology:* A novel circuit topology, using a power electronic H-bridge in combination with a series RLC network, is proposed to generate the PRIS signal. It is shown that the circuit represents an efficient

and compact perturbation source that has the potential to operate at voltages in the kV range. The effects of the target system to be estimated on the PRIS perturbation current are investigated. The impedance of the target is shown to have considerable influence on the time- and frequency-domain characteristics of the perturbation current. The initial energy in the inductor and capacitor associated with a practical PRIS source are furthermore shown, through mathematical analysis of the PRIS source, to affect the shape of the chopped impulse waveforms that constitute the PRIS.

- *Application of the PRIS signal for wideband characterisation of grid impedance:* The proposed PRIS signal is applied for wideband characterisation of the grid impedance of a supply network, where the supply voltage exhibits a fair degree of harmonic voltage distortion and stochastic behaviour. A novel experimental approach is proposed to minimize the effects of voltage distortion and the time-dependent variation of the supply voltage on the estimated frequency responses and model parameters.

1.4 Dissertation layout

The remainder of this dissertation is organized as follows:

Chapter 2: The properties and performance metrics that typically apply for determining the suitability of a perturbation signal for system identification and parameter estimation experiments in the energy field are introduced and an overview of classical perturbation signals is presented. The circuit topologies typically used for *in situ* perturbation of active ac systems are reviewed and critically discussed.

Chapter 3: The time-domain modelling and analysis of the PRIS signal are presented. The results are discussed in the context of the suitability of the signal for system identification and parameter estimation applications in the field of power engineering.

Chapter 4: The frequency-domain modelling and analysis of the PRIS signal are presented. The results are discussed in the context of the suitability of the signal for system identification and parameter estimation applications in the field of power engineering.

Chapter 5: A practical circuit topology for a bipolar PRIS perturbation source is proposed. The design considerations of the source are discussed.

Chapter 6: The performance of the PRIS perturbation signal and perturbation source for conducting *in situ* frequency response measurements of the grid impedance of an MV

case study network is evaluated. Results are presented for the grid impedance frequency responses derived for the target network. A wideband lumped-parameter equivalent circuit model is proposed for the network and parameter estimation algorithms are applied to estimate the associated circuit parameters using the measured frequency responses of the grid impedance.

Chapter 7: The results of the investigation are critically reviewed and conclusions are presented with reference to the original research objectives. Proposals for further research are presented.

CHAPTER 2

Critical Overview of Signals and Topologies for *in situ* Perturbation of Energy Systems

2.1 Overview

System identification and parameter estimation methodologies typically involve excitation of a target system with a wideband perturbation signal, such that the input and output signals capture all relevant dynamic modes of the system under test [34], [35]. In non-parametric system identification, the measured response of the system is cross-correlated with the measured input signal, or a transfer function is estimated using the discrete Fourier transforms of the input and output signals [5], [36]. In the model-based parametric estimation, on the other hand, a system model is assumed and the identification involves estimation of the model parameters [35].

These experiments are affected in practice by disturbance noise, including environmental noise, digitizer noise, system noise, etc. The effects of noise on the estimated results are inversely proportional to the SNR of the measured signals. The spectral energy of the perturbation signal, therefore, needs to be sufficient throughout the frequency band of interest to achieve an acceptable SNR [4], [37]. In comparison with system identification and parameter estimation experiments targeting electronic circuitry and control systems, experiments targeting high power, high voltage AC applications present several unique additional challenges, including the following:

- The perturbation signal should not introduce bias such that the normal operating region of the device under test is disturbed excessively. This is particularly important for applications targeting electromagnetic components, where DC bias or high-amplitude, low-frequency excitation can give rise to core saturation effects.

- The perturbation signal should not result in excessive measurement times. This can lead to inaccurate results in cases where operating conditions are dynamic and change during the measurement period. This is of interest for systems operating *in situ* under dynamic conditions, such as machines and loads, or systems reflecting stochastic behaviour, such as grid impedance.

- The voltage and current ratings of the perturbation source must be compatible with the operating conditions that apply for the target system. This implies that the perturbation signal should ensure an acceptable SNR, but should not cause the voltage and current ratings of the system under test to be exceeded.

- The perturbation source should employ an energy-efficient, low-cost circuit topology.

The metrics that are commonly used in literature to characterise the signal quality of a perturbation signal include the following [6], [34]:

- **Crest factor**: The crest factor C_F of a signal x is defined as the ratio of the peak value x_{pk} to the effective RMS value x_{RMSe}. This yields

$$C_F = \frac{x_{pk}}{x_{RMSe}}. \tag{2.1}$$

  The Root Mean Square (RMS) value x_{RMSe} reflects the spectral power over the frequency band of interest. Signals with an impulse characteristic have a large crest factor. Although the peak amplitude x_{pk} may be high, the RMS value x_{RMSe} may be insufficient to ensure an acceptable SNR over the frequency band of interest.

- **Time factor:** The time factor of a perturbation signal represents the power distribution of the signal over the frequency band of interest. Unequal distribution of the spectral power of the perturbation signal with respect to the noise level results in poor measurement results at some frequencies. The SNR should, ideally, be constant over the frequency band of interest to achieve uniform accuracy. A system presenting noise with a flat power spectrum, for instance, should be excited with a perturbation signal with a flat amplitude spectrum.

It follows that an optimum perturbation signal should have a low crest factor and low time factor.

Schoukens *et al.* [4] divided the excitation signals used in system identification and parameter estimation applications into three categories, namely periodic signals, transient signals, and aperiodic signals. The excitation signals applied in the early 1960s focussed predominantly on the swept sine wave [4], [8], [34]. In this method, a sinusoidal signal with slowly varying frequency is injected into the target system, while measurements are conducted using a tracking filter. Various other excitation signals based on sinusoidal waveforms have been proposed in the literature, including the stepped-sine signal, periodic chirp signal and multi-sine signal. Perturbation signals based on sinusoidal signals are, however, not well suited for high power applications in practice. These signals require that the active components of the

perturbation source circuitry operate in linear mode. This gives rise to high voltage, current and power ratings for these components. Digital signal processing algorithms, however, have made it possible to use complex input signals. These signals have broadband spectrums, which allows for the required spectral information to be collected from a single measurement [4], [8]. This facilitates shorter measurement periods, but signal processing errors such as aliasing and leakage may be introduced if no precautions are taken [8].

2.2 Classical perturbation signals

2.2.1 Periodic signals

2.2.1.1 Stepped sine signal

The stepped sine signal implements a pure sinusoidal waveform, as defined by the relationship

$$x(t) = A\sin(\omega t), \tag{2.2}$$

where the radian frequency ω changes in discrete steps through the measurement period or from measurement to measurement. The stepped sine signal has been applied successfully to measure the impedance of energized grids for the frequency range between the fundamental grid frequency and frequencies in the kHz range [38]. The stepped sine has also been applied in transformer FRA for the detection of faults and wideband modelling [32], [39], [40]. The signal is characterised by good SNR, but the sequence of frequency changes gives rise to long measurement periods [8], i.e. of the order of several minutes. The measurement is likely to be a manual process, with magnitude and phase information collected after each frequency change. The transient responses associated with the instances where the frequency changes occur have, furthermore, to be omitted from the analysis to ensure accurate results. The methodology is thus not well suited for online measurements where the target system exhibits non-stationary stochastic behaviour over time [24].

2.2.1.2 Swept sine signal

In the case of the swept sine signal, the frequency of a sinusoidal excitation signal is swept up and/or down over the measurement period [4]. The signal is defined by the relationship

$$x(t) = \sin[(at + b)t] \qquad 0 \leq t \leq T, \tag{2.3}$$

where T denotes the period, $a = 2\pi(f_2 - f_1)/T$, $b = 2\pi(f_1)$, and f_1 and f_2 represent the lower and upper frequencies respectively of the frequency band that applies. If the frequency

is swept slowly, steady-state frequency response measurements are obtained over the measurement interval. The periodic chirp signal represents a swept sine signal where the sweeping is performed rapidly and repetitively such that a periodic signal is created with the same period as the measurement period.

The swept sine has been applied extensively in transformer FRA for the detection of faults and wideband modelling [30], [32], [39], [40].

2.2.1.3 Multi-sine signal

The multi-sine signal is represented by a sum of harmonically related sinusoidal signals [1], [4] [8]. It is defined by the relationship

$$x(t) = \sum_{k=1}^{m} A_k \sin(\omega_k t + \phi_k), \tag{2.4}$$

where A_k, ω_k and ϕ_k denote the amplitude, radian frequency and phase respectively of the k^{th} sinusoidal component. Perturbation using a multi-sine signal reduces the measurement time in comparison to the stepped sine and swept sine, whilst retaining good SNR. The amplitudes, frequencies, and phases of the harmonic components can, furthermore, be optimised using numerical optimisation routines to achieve an optimal power spectrum and crest factor. In this context, the amplitudes determine the power spectrum, while the phases influence the peak value of the signal [8]. Optimization of these signal parameters, however, complicates the design of the perturbation source [34]. Multi-sine signals are also not suitable for applications where the input transducers cannot cope with an infinite number of discrete amplitudes [7].

2.2.2 Transient signals

2.2.2.1 Random burst signal

The random burst signal is represented by a white noise sequence injected during a part of the measurement period, with zero input injected for the rest of the measurement duration [34]. Similar to other stochastic signals, a large number of averages are required to obtain acceptable accuracy. The signal is defined by the mathematical relationship

$$x(t) = g(t)h(t), \tag{2.5}$$

where

$$g(t) = \begin{cases} 1 & 0 \leq t < T_1 \\ 0 & T_1 \leq t < T, \end{cases}$$

and $g(t)$ and $h(t)$ denote a window function and a random variable respectively.

2.2.2.2 Impulse excitation signal

The ideal impulse signal contains spectral energy throughout the entire frequency band, and can, therefore, be used to extract information at all frequencies. The signal, therefore, represents the ideal perturbation signal. The ideal impulse signal can, however, not be generated in practice. The practical impulse signal used in system identification applications has a waveform that mimics the impulse waveshape that is widely used in high voltage testing, in the sense that it has a fast rise time and a slow fall time, thereby providing wideband excitation.

Impulse perturbation signals have been used extensively for identification of system impedance [3], [21], [23] and power transformers [30], [32], [41]. Impulse perturbation offers the advantage of short measurement periods, which makes the method suitable for applications of dynamic nature, such as grid impedance measurements. A relatively high voltage pulse impacts positively on the SNR, even in the presence of interference from nearby energized transformers in a substation environment. The signal, furthermore, ensures a relatively broad frequency spectrum [32].

Impulse excitation is, however, not ideal in some applications. Impulse perturbation in transformer FRA measurements, for instance, exhibits noisy results for the low-frequency range below 1 kHz [41]. In the case where a short impulse perturbation is applied to a transformer, the transformer core will not complete a full cycle through the B-H curve [41]. This results in insufficient information in the transformer response to achieve a good estimate of the time-varying magnetizing inductance. The spectral energy of the impulse signal cannot be easily controlled and decays rapidly with frequency [26]. The dynamic operation point of the system under test may also be compromised in measurements where a high impulse amplitude is injected to achieve a high SNR. The impulse signal is, furthermore, a unipolar signal. This introduces a degree of DC bias, which may impact negatively on the response of electromagnetic apparatus such as transformers and electrical machines.

2.2.3 Pseudorandom signals

2.2.3.1 Pseudo-random noise signals

The pseudo-random noise signal consists of a sum of sinusoids with random phase values [4]. The signal is similar to the multi-sine signal but differs in respect of the optimisation of the phase angles of the sine components. The signal is defined by the mathematical expression

$$x(t) = \sum_{k=1}^{m} A_k \sin(\omega_k t + \phi_k), \tag{2.6}$$

where the phase angle ϕ_k is a uniformly distributed and random in the interval $[0, 2\pi]$.

2.2.3.2 Periodic noise signal

A periodic noise signal is generated by periodically repeating a noise sequence. The measurements are conducted when the transients associated with the transitions between the noise periods and zero periods are damped out. The signal exhibits the same behaviour as random noise, except for the lack of leakage problems due to periodicity of the signal [4]. Due to the stochasticity of this signal, its amplitude spectrum is not flat. Averaging is necessary to obtain acceptable accuracy.

2.2.3.3 Pseudo-random binary sequence

A PRBS is a form of a deterministic and periodic white noise signal based on Maximum Length Binary (MLB) sequences. The signal can be readily generated using a Linear Feedback Shift Register (LFSR). It consists of a bitstream of ones and zeros that occur pseudo-randomly over a period T, after which the sequence is repeated. The binary transitions occur at discrete intervals, which are multiples of the PRBS clock period, T_{clk} [1], [34]. The repetition period, T, is defined by the number of clock periods, N, that occur before the sequence repeats, such that $T = N \times T_{ckl}$, where $N = 2^n - 1$ bits, with n an integer number greater than 1 representing the number of shift registers.

The power spectral density (PSD) of the PRBS is defined by the mathematical expression [13]

$$S(\omega) = \frac{a^2(N+1)T_{clk}}{N}\left[\frac{\sin(\omega\frac{T_{clk}}{2})}{\omega\frac{T_{clk}}{2}}\right]^2, \tag{2.7}$$

where a is the signal amplitude and ω is the frequency.

Figure 2.1 shows a plot of the PSD of the PRBS. The spectrum is composed of line spectral components with a harmonic separation or frequency resolution of $1/T$ [13], [42], [43]. The

signal exhibits an almost uniform PSD over the frequency band from $f = \frac{1}{T}$ to the upper -3dB cut-off frequency located at $\frac{1}{3} \times f_{clk}$. The upper frequency sidelobes are defined by the zeros occurring at $f = n/T_{clk}$, where n is an integer as shown in Figure 2.1. The PSD of a PRBS signal decays rapidly above the -3dB cut-off frequency, which might result in low SNR, especially in FRA measurements. This can, however, be mitigated by selecting a PRBS clock frequency, f_{clk}, such that the frequency range of interest is accommodated.

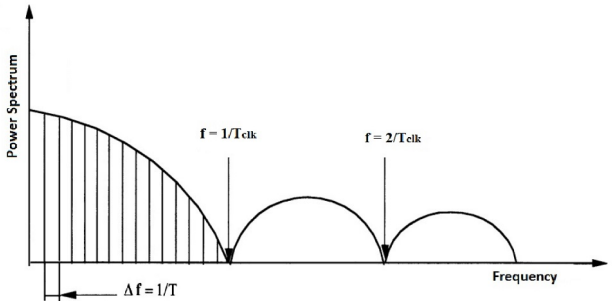

Figure 2.1: Power spectral density of the PRBS [43].

Measurements performed with the PRBS are repeatable due to the deterministic properties of the signal. The pseudo-random property associated with the PRBS signal ensures a wide-band frequency spectrum so that the target system dynamics can be excited uniformly over a predetermined frequency band [44]. Periodic averaging can, furthermore, be implemented to reduce the leakage problem associated with random signals.

The PRBS has been used for the testing of measurement transducers and system identification in the fields of acoustics and biology [43]. The use of PRBS signals has been extended to parameter estimation for the circuit models of electrical equipment such as generators, motors, transformers and power converters [2], [9], [10], [28], [41]. Jordan *et al.* [15] and Roinola *et al.* [26], [45] proposed the use of the PRBS and multilevel PRBS for grid impedance measurements. The proposed methodology presents some advantages in comparison to impulse excitation, including low signal amplitude requirements, cost-effectiveness, and ease of signal generation and data acquisition [26]. MLB based sequences have, furthermore, been shown to produce good results, even under low SNR conditions and tight restrictions on the amplitude of the perturbation signal.

The flat frequency spectrum exhibited by the PRBS makes it suitable for many applications that require excitation with a uniform PSD distribution [46]. Unipolar excitation is, however, not ideally suited for applications involving electromagnetic power system apparatus, such as transformers and electrical machines, due to the possibility of injecting low-frequency components that can result in core saturation. The unipolar PRBS signal may, furthermore, drive

the system under test towards a biased offset point from the operating point prevailing at the start of the perturbation [2]. This would typically occur if a long PRBS sequence is used [10]. In this context, Vermeulen *et al.* [2] proposed the use of a bipolar PRBS as a perturbation signal in a study aimed at online parameter estimation of a synchronous generator model.

2.2.3.4 Discrete-interval binary sequence

The discrete-interval binary sequence (DIBS) represents a class of pseudorandom sequences that can be optimised [26]. In the DIBS, the energy of a number of harmonic frequencies is maximized at the expense of the remainder of harmonic frequencies. The energy associated with the specified frequencies is increased without increasing the time-domain amplitude of the sequence, thereby giving rise to a low crest factor. The frequency resolution of such a sequence is, however, reduced. Roinila *et al.* [24] applied DIBS for online identification of grid impedance, by injecting the sequence into the reference signal of an inverter. As in the case of the PRBS, perturbation with a DIBS signal can result in nonlinear saturation, especially when used to identify power equipment with electromagnetic components.

2.2.4 Aperiodic signals

2.2.4.1 Random noise signal

The random noise signal basically consists of a sequence of white noise. The power spectrum of this signal can be controlled by using digital filters [34]. Random noise perturbation signals have the advantage of uniform excitation over the frequency band of interest. The signal is, furthermore, relatively easy and safe to implement. Random signals, however, have a disadvantage in the form of the leakage problem that occurs in the frequency domain after windowing. Averaging is necessary to eliminate non-coherent noise [47].

2.3 Overview system topologies for *in situ* application of PRBS perturbation signals

In situ identification implies that the system under test remains connected to the normal supply voltage while the perturbation signal is applied, and the input and output waveforms of interest are recorded. The target system thus does not need to be taken offline, which minimizes disruption and avoids production losses. The effects of the normal operating conditions are, furthermore, taken into account in the *in situ* approach. The perturbation signal is superimposed on the normal operating signal. Its amplitude has to be optimised such that it is low

enough to ensure that the target system is not disturbed too far from the optimum operating condition thus avoiding disturbance to connected equipment and customers, whilst it is also high enough to ensure an acceptable SNR.

Figure 2.2 illustrates a common system topology for applying a perturbation signal *in situ* to a system operating with a sinusoidal supply voltage waveform. The AC supply source is represented by a Thevenin equivalent circuit consisting of an AC voltage source, $v_{Th}(t)$, and series impedance, Z_{Th}. The perturbation source is connected in parallel with the target system. Due to the voltage drop induced across Z_{Th}, the perturbation current, $i_p(t)$, induces a voltage perturbation on the supply voltage waveform, $v_T(t)$, of the target system. System identification and parameter estimation are performed using the supply waveforms $v_T(t)$ and $i_T(t)$. The frequency response of the input impedance of the target system, $Z_T(w)$, is given by the relationship

$$Z_T(w) = \frac{\mathcal{F}\{v_T(t)\}}{\mathcal{F}\{i_T(t)\}}, \tag{2.8}$$

where $\mathcal{F}$ denotes the Fourier transform.

The topology shown in Figure 2.2 can, in principle, also be applied to characterise the Thevenin equivalent source impedance Z_{Th}. In this application, Z_{Th} is determined from the dynamic voltage and current responses of the supply network, i.e. $v_T(t)$ and $i_s(t)$, and the open-circuit waveform of the Thevenin equivalent source, $v_{Th}(t)$. The frequency response of the Thevenin equivalent source impedance, $Z_{Th}(w)$, is given by the relationship

$$Z_{Th}(w) = \frac{\mathcal{F}\{v_{Th}(t) - v_T(t)\}}{\mathcal{F}\{i_s(t)\}}. \tag{2.9}$$

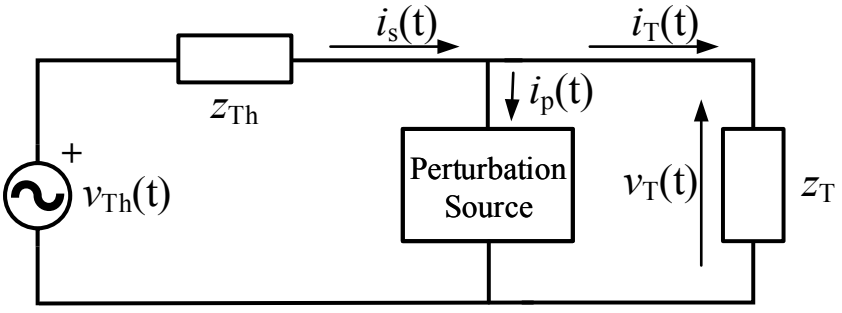

Figure 2.2: System topology for *in situ* application of a perturbation signal to an AC system.

Figure 2.3 shows the system topology typically used for *in situ* application of a PRBS current perturbation source to an AC target system. Van Rooijen *et al* [10] applied the topology shown in Figure 2.3, using a bi-directional PRBS current source, to derive a wideband model for a

magnetic voltage transformer. The bi-directional PRBS current source applied in the investigation consists of a uni-directional PRBS current source connected to the target system through an H-bridge, where the switches of the H-bridge are activated by PRBS gate signals. The topology offers the advantage of a controllable and well-defined PRBS current perturbation signal. The active elements of the current source, however, operate in linear mode, which gives rise to high power losses. This limits the scope of application of this approach in the high power, high voltage environment.

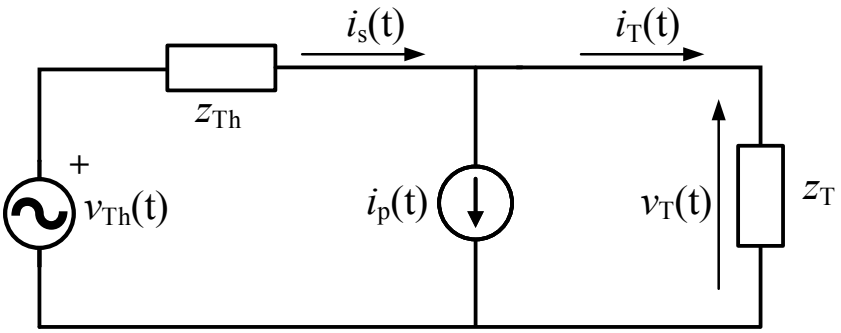

Figure 2.3: System topology for *in situ* application of a PRBS current source to an AC system.

Figure 2.4 shows a system topology for *in situ* application of a PRBS voltage perturbation source to an AC target system. The PRBS voltage source typically consists of a DC source connected through an H-bridge and a series impedance, Z, where the switches of the H-bridge are activated by PRBS gate signals, as shown in Figure 2.5. This topology has the advantage that the power electronic elements do not operate in linear mode, which reduces the power ratings of the associated source circuitry. The arrangement, however, also has a disadvantage in the sense that the waveform of the perturbation current, $i_p(t)$, is highly dependent on the series impedance Z and parallel impedance of the Thevenin equivalent AC source and the target.

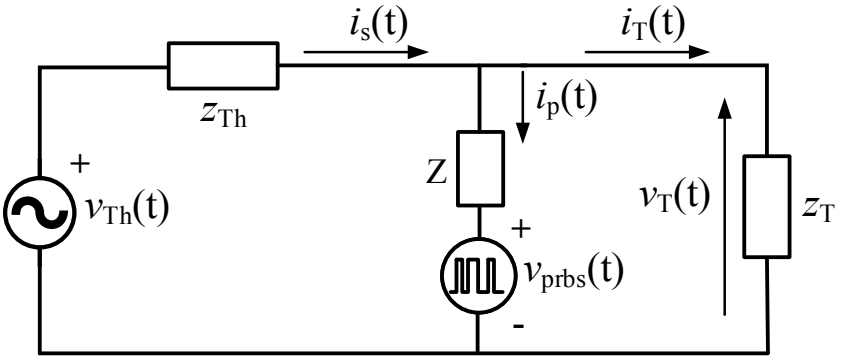

Figure 2.4: System topology for *in situ* application of a PRBS voltage source to an AC system.

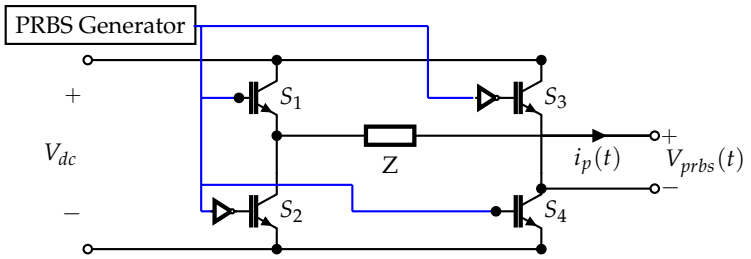

Figure 2.5: Circuit diagram of a H-bridge configuration controlled by PRBS gate signals.

In the PRBS voltage source perturbation applications reported in literature, the series impedance Z shown in Figure 2.4 is typically represented by a purely resistive element, as shown in Figure 2.6 [15], [48]. This arrangement offers limited control over the frequency spectrum characteristics of the perturbation current. It has the further disadvantage that the AC source can induce a large sinusoidal current component in the PRBS voltage source, especially in high power, high voltage applications. This increases the current ratings of the active elements comprising the H-bridge and DC voltage source. The topology can, furthermore, give rise to high losses in the series resistor.

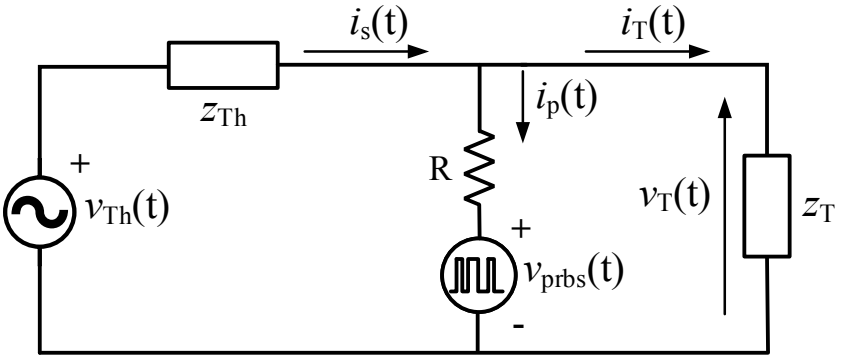

Figure 2.6: System topology *in situ* application of a PRBS voltage source to an AC system through series resistive element.

Figure 2.7 shows simulated results for the PRBS voltage signal $v_{prbs}(t)$, perturbation current $i_p(t)$ and target voltage $v_T(t)$ for the circuit topology shown in Figure 2.6. The simulation is conducted for $V_{prbs} = 50V$ and $R = 50\Omega$, and a 50 Hz single-phase supply network where $V_{Th} = 220V_{rms}$ and $Z_{Th} = 0.4 + j0.25\Omega$. The target is represented by a pure resistive load of 100Ω. The results confirm that the perturbation current $i_p(t)$ has a significant 50 Hz sinusoidal component. This gives rise to high power losses in resistor R and in the active elements associated with the PRBS voltage source. Overall, this increases the physical size of the perturbation source, especially in power applications [48]. The results, furthermore, show that the perturbation signal imposed on the voltage waveform applied to the target system, $v_T(t)$,

differs substantially from the ideal PRBS waveform. This impacts on the frequency-domain properties of the perturbation signal which can, in turn, be expected to impact on the overall success of the associated system identification or parameter estimation experiment.

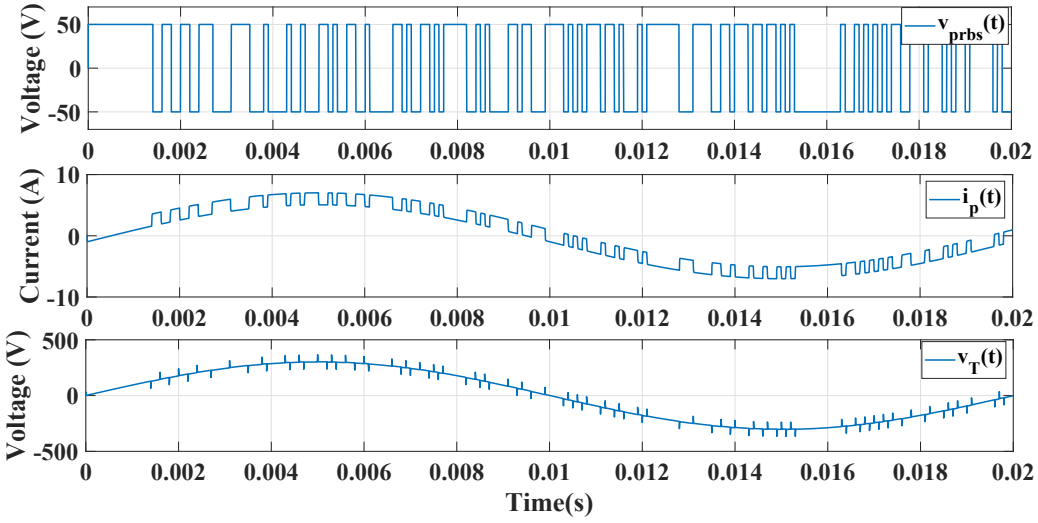

Figure 2.7: Simulated PRBS voltage signal $v_{prbs}(t)$, perturbation current $i_p(t)$ and target voltage $v_p(t)$ for the circuit topology shown in Figure 2.6.

2.4 Conclusion

The perturbation signals that are commonly used for system identification and parameter estimation are discussed. In the context of power system applications, it is desirable that the spectral characteristics of the perturbation signal can be controlled to suit various applications, for instance, to reduce or increase power in certain frequency bands to avoid saturation or increase SNR. Wideband signals such as random noise and PRBS have a flat spectrum below the -3dB point and offer limited control parameters. The multi-sine and DIBS signals have complex spectral optimisation techniques and are also not feasible for direct injection into an active source. In high power applications, a bipolar perturbation signal is desired as it ensures that the system under test is not driven towards a biased offset point from the operating point existing at the start of the excitation.

An overview of system topologies for *in situ* application of PRBS perturbation signals is also presented. These include the PRBS current source and the PRBS voltage source. It is noted that these two topologies have a limitation of high power losses and therefore unsuitable for high power applications. In the case of the PRBS current source, for example, the power electronic switching elements operate in linear mode, thereby giving rise to high losses. The PRBS voltage

source uses a resistive coupling to the system under test. This resistor increases power losses in the topology and reduces the controllability of this perturbation source. Furthermore, when used in *in situ* applications, the perturbation signal generated by this source has a high sinusoidal current component which increases power losses and current ratings of the perturbation source circuit.

CHAPTER 3

Time-Domain Modelling of the Pseudo-Random Impulse Sequence

3.1 Introduction

Section 2.2 reviewed a wide range of perturbation signals that have been successfully applied for system identification and parameter estimation applications in the literature. Overall, however, most of these signals are not ideally suited for application in the field of electrical energy systems, where the target systems typically reflect high power and high voltage operating conditions. These considerations are of particular importance in the case of *in situ* applications, where the perturbation signal is injected into an active high power, high voltage system. Although some of the classical signals have been applied successfully in high power applications, the range of application is often limited due to the inherent constraints that are imposed on the design of the associated perturbation sources. These constraints include design complexity, power losses and efficiency, controllability, etc.

This chapter introduces a novel perturbation signal for high power, high voltage system identification and parameter estimation applications, namely the pseudo-random impulse sequence (PRIS). The PRIS signal seeks to combine the most advantageous characteristics of the classical PRBS signal and the classical impulse waveform used in high voltage engineering. The time-domain properties of the PRIS signal, including the mathematical formulation, wave shape properties and source design considerations, are discussed.

3.2 Time-Domain modelling of the pseudo-random impulse sequence

3.2.1 Time-shifted chopped impulse waveform

The classical impulse waveform $f_i(t)$ is characterised by an exponential front and an exponentially decaying tail [49]. Figure 3.1 shows that the wave shape can be represented as the sum of a positive exponential component and negative exponential component, as defined by the expression

$$f_i(t) = U[e^{-(t)/\tau_2} - e^{-(t)/\tau_1}], \tag{3.1}$$

where U denotes the amplitude of the exponential functions, and τ_1 and τ_2 denote the time constants of the negative and positive exponential terms respectively. The rise time of the impulse is dominated by τ_1, while fall time is dominated by τ_2.

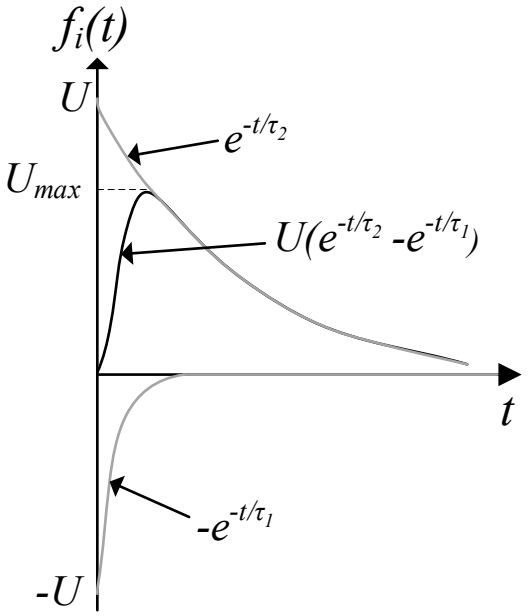

Figure 3.1: Representation of the impulse waveform as the sum of two exponential functions.

The impulse waveform defined by (3.1) can be shifted in time to yield the expression

$$f_i(t - t_i) = U[e^{-(t-t_i)/\tau_2} - e^{-(t-t_i)/\tau_1}], \tag{3.2}$$

where t_i denotes the time delay to the start of the impulse.

In order to derive a time-shifted, chopped impulse waveform, $f_{ic}(t - t_i)$, the time-shifted impulse waveform $f_i(t - t_i)$ is multiplied by a delayed finite-width pulse $f_{p,t_i,t_{i+1}}(t)$, where

$$f_{p,t_i,t_{i+1}}(t) = u(t - t_i) - u(t - t_{i+1}). \tag{3.3}$$

$u(t - t_i)$ and $u(t - t_{i+1})$ denote unit step functions delayed by $t = t_i$ and $t = t_{i+1}$ respectively. This yields a time-shifted chopped classical impulse waveform which can be expressed as

$$f_{ic}(t - t_i) = f_i(t - t_i) f_{p,t_i,t_{i+1}}(t) \tag{3.4}$$

The development of a time-shifted chopped impulse waveform defined by (3.4) is illustrated in Figure 3.2. The time-shifted chopped classical impulse waveform represents the main building block for the proposed PRIS signal.

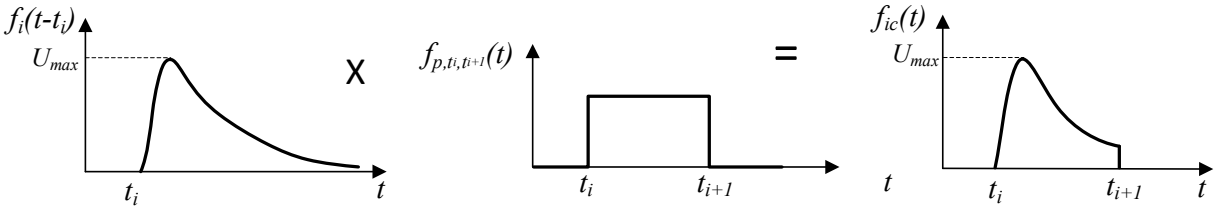

Figure 3.2: Development of the time-shifted chopped impulse waveform $f_{ic}(t - t_i)$.

Figure 3.3 shows the waveforms associated with the impulse waveform $f_i(t)$, the time-shifted impulse waveform $f_i(t - t_i)$ and the time-shifted chopped impulse waveform $f_{ic}(t - t_i)$. The maximum amplitude, U_{max}, of the time-shifted impulse function $f_i(t - t_i)$ occurs at time $t = t_{max}$.

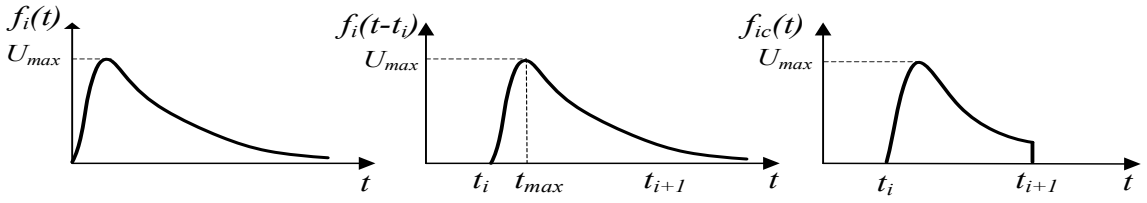

Figure 3.3: Impulse waveform, time-shifted impulse waveform and time-shifted chopped impulse waveform.

An expression can be derived for t_{max} by equating the first derivative of (3.2) to zero at time $t = t_{max}$. From (3.2), the derivative of $f_i(t - t_i)$ is given by the relationship

$$\frac{\mathrm{d}[f_i(t-t_i)]}{\mathrm{d}t} = U\Big[(-\frac{1}{\tau_2})e^{\frac{-(t-t_i)}{\tau_2}} - (-\frac{1}{\tau_1})e^{\frac{-(t-t_i)}{\tau_1}}\Big]. \tag{3.5}$$

Let $t = t_{max}$ and $\dfrac{\mathrm{d}[f_i(t-t_i)]}{\mathrm{d}t} = 0$ in (3.5). This yields

$$\frac{1}{\tau_1}e^{\frac{-(t_{max}-t_i)}{\tau_1}} = \frac{1}{\tau_2}e^{\frac{-(t_{max}-t_i)}{\tau_2}}, \tag{3.6}$$

which can be rearranged so that

$$e^{t_{max}\frac{(\tau_1-\tau_2)}{\tau_1\tau_2}} = \frac{\tau_1}{\tau_2}e^{t_i\frac{(\tau_1-\tau_2)}{\tau_1\tau_2}}. \tag{3.7}$$

This yields

$$t_{max} = \frac{\tau_1\tau_2}{\tau_1-\tau_2}\ln\left[\frac{\tau_1}{\tau_2}\right] + t_i. \tag{3.8}$$

The value of U_{max} for $t_{max} < t_{i+1}$ is obtained by substituting (3.8) into (3.2). This yields

$$U_{max} = U\Big[\big(\frac{\tau_2}{\tau_1}\big)^{\frac{\tau_1}{\tau_1-\tau_2}} - \big(\frac{\tau_2}{\tau_1}\big)^{\frac{\tau_2}{\tau_1-\tau_2}}\Big] \tag{3.9}$$

Equation (3.9) shows that the peak value of the time-shifted impulse signal is dependent on the peak value of the two exponential functions and the time constants τ_1 and τ_2.

3.2.2 Pseudo-random binary sequence waveform

Figure 3.4 shows the waveform of the PRBS signal, $f_{PRBS}(t)$, introduced in Section 2.2.3.3, together with the associated clock signal, $f_{clk}(t)$. The signal is generated by a deterministic algorithm, but emulates the statistical properties of a random sequence, since the occurrence and duration of the binary states are random. The PRBS is typically generated by a feedback shift register driven by a clock signal $f_{clk}(t)$. The PRBS is periodic in the sense that the random sequence repeats after several clock cycles, N, which is determined by the configuration of the feedback register. A PRBS with a repetition period of N clock cycles contains 2^{n-1} or $(N+1)/2$ logic one states and $2^{(n-1)} - 1$ logic zero states. The number of state transitions is 2^{n-1}. A single PRBS period incorporates 2^{n-1} or $(N+1)/2$ runs, where a run denotes the sequence between two successive state transitions. One-half of these runs are one clock period long, one quarter are two clock periods long, one eighth are three clock periods long, etc [13].

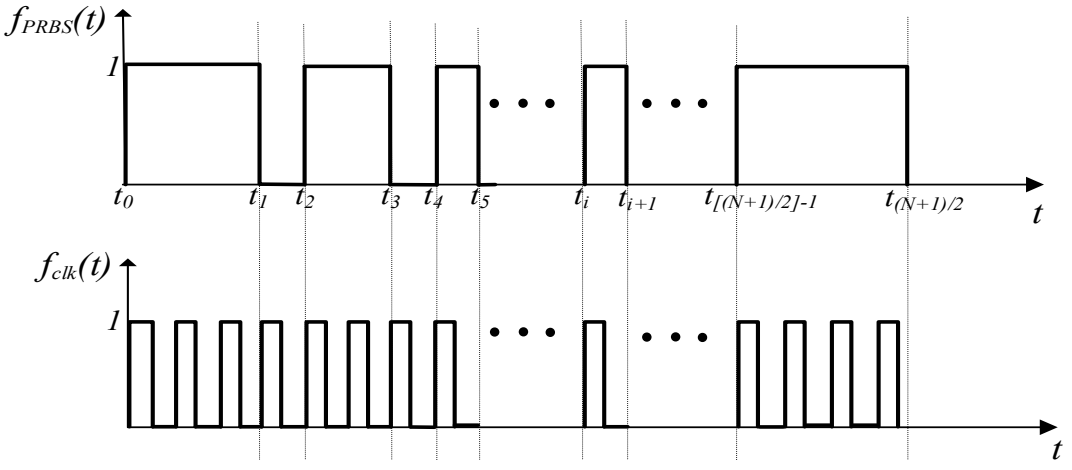

Figure 3.4: A pseudo-random binary sequence, $f_{PRBS}(t)$, and the associated PRBS clock signal, $f_{clk}(t)$.

The PRBS waveform can be considered as a sequence of pulses of the form defined by (3.3), where t_i and t_{i+1} are associated with two successive state transitions of the PRBS. In the context of the PRIS proposed in this investigation, pairs of successive state transitions of the PRBS are used to trigger and chop the time-delayed impulse wave shapes defined by (3.2). The state

transitions represented by t_i and t_{i+1} are pseudo-random variables, that are generated using the relationship

$$t_{i+1} = t_i + kT_{clk} \qquad 1 \leq k \leq n \tag{3.10}$$

where $T_{clk} = \frac{1}{f_{clk}}$ denotes the period of the PRBS clock signal, k denotes a random integer number and n denotes the number of stages in the shift register used to generate the PRBS. In this context, kT_{clk} represents the length of the i^{th} PRBS run and nT_{clk} represents the length of the longest PRBS run.

3.2.2.1 Unipolar pseudo-random impulse sequence

The unipolar pseudo-random impulse sequence, $f^{U}_{PRIS}(t)$, consists of a pseudo-random sequence of time-shifted, chopped impulse waveforms of the form defined by (3.4). The signal is derived by initiating a positive impulse waveform of the form defined by (3.2) at each state transition of the PRBS, which is chopped by the state transition that initiates the next impulse waveform, as illustrated in Figure 3.5.

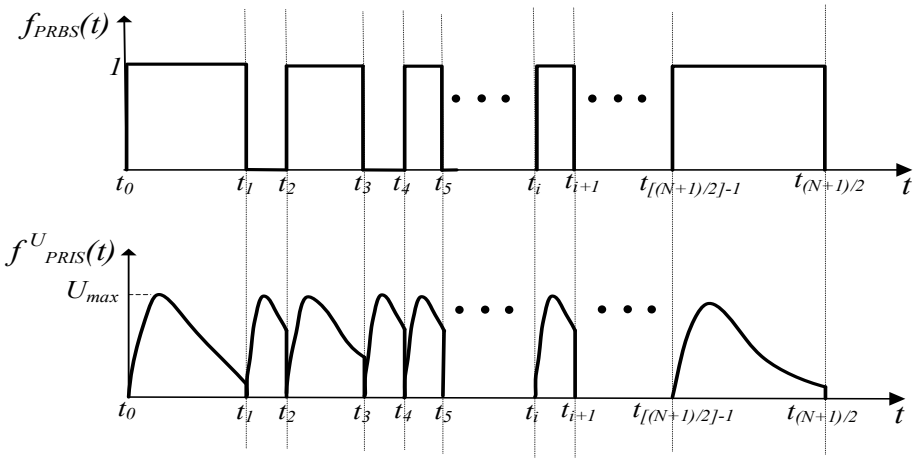

Figure 3.5: A pseudo-random binary sequence, $f_{PRBS}(t)$, and the associated unipolar pseudo-random impulse sequence, $f^{U}_{PRIS}(t)$.

The unipolar PRIS sequence is defined by the mathematical expression

$$f^{U}_{PRIS}(t) = \sum_{i=0,1,2\ldots}^{((N+1)/2)} f_i(t - t_i) f_{p,t_i,t_{i+1}}(t), \tag{3.11}$$

where $f_i(t - t_i)$ denotes the time-shifted impulse waveform defined in (3.2) and

$$f_{p,t_i,t_{i+1}}(t) = u(t - t_i) - u(t - t_{i+1}), \tag{3.12}$$

where t_i and t_{i+1} denote the time instances of the i^{th} and $(i+1)^{th}$ state transitions of the PRBS respectively.

The PRBS state transitions are pseudo-random variables. The impulses associated with the unipolar PRIS signal are therefore pseudo-randomly located and are also pseudo-randomly chopped. The shapes of the individual chopped impulse waveform are determined by the pulse lengths, i.e. $t_{i+1} - t_i$, of the PRBS and the time constants, τ_1, τ_2 of the impulse signal. Higher values of f_{clk} result in shorter pulse lengths, and consequently in early chopping of the impulses wave shapes. This may cause front-chopping of the impulse wave shapes, i.e. before the maximum point U_{max} is reached. Higher values of τ_1 may give rise to a similar effect. The time-domain properties of the PRIS can thus be controlled by varying f_{clk}, n, τ_1 and τ_2.

3.2.2.2 Bipolar pseudo-random impulse sequence

The bipolar pseudo-random impulse sequence, $f^B_{PRIS}(t)$, consists of a pseudo-random sequence of alternating positive and negative time-shifted, chopped impulse waveforms of the form defined by (3.4). The signal is derived by initiating a positive impulse waveform of the form defined by (3.2) at each positive state transition of the PRBS and a negative impulse waveform at each negative state transition of the PRBS, each of which is chopped by the state transition that initiates the next impulse waveform, as illustrated in Figure 3.6.

The bipolar PRIS sequence is defined by the mathematical expression,

$$f^B_{PRIS}(t) = \sum_{i=0,2,4\ldots}^{((N+1)/2)-1} f_i(t-t_i) f_{p,t_i,t_{i+1}}(t) - \sum_{i=1,3,5\ldots}^{((N+1)/2)} f_i(t-t_i) f_{p,t_i,t_{i+1}}(t), \tag{3.13}$$

where

$$f_{p,t_i,t_{i+1}}(t) = u(t-t_i) - u(t-t_{i+1}), \tag{3.14}$$

where t_i and t_{i+1} denote the time instances of the i^{th} and $(i+1)^{th}$ state transitions of the PRBS respectively.

3.3 Simulation of the pseudo-random impulse sequences

3.3.1 Overview

The waveforms associated with the expressions defined by (3.11) and (3.13) for the unipolar and bipolar pseudo-random impulse sequences respectively can be readily simulated, using several approaches. The time instances at which the impulse waveforms are initiated and chopped, i.e. t_i and t_{i+1} respectively, are pseudo-random variables that are determined by the

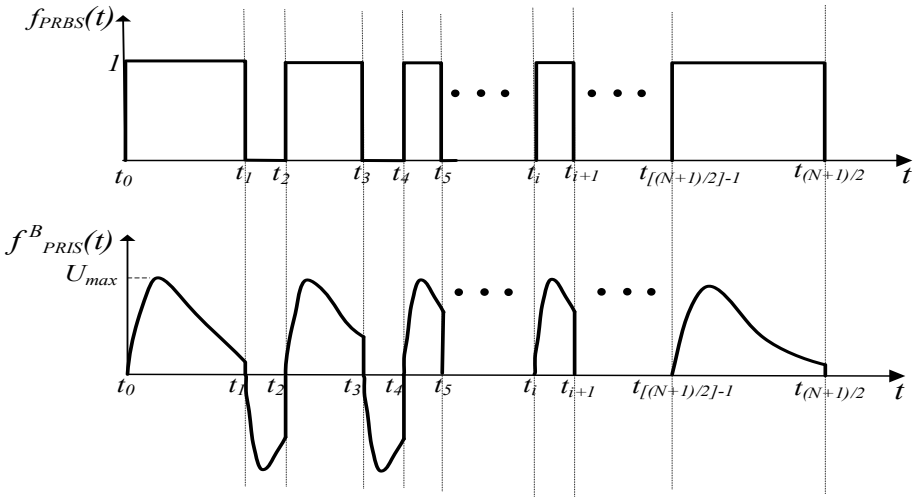

Figure 3.6: A pseudo-random binary sequence, $f_{PRBS}(t)$, and the associated bipolar pseudo-random impulse sequence, $f^B_{PRIS}(t)$.

PRBS sequence that is implemented. The values of t_i and t_{i+1} are thus derived from a feedback shift register driven by a clock signal with frequency $f_{clk}(t)$.

The Simulink platform represents a convenient tool for time-domain analysis of the ideal PRIS, that also offers extensive support for frequency-domain analysis. The PRBS shift register can be implemented using unit delays and are configured with a sample time equal to the clock period $T_{clk}(t)$. A feedback path is provided via modulo-two gates, with binary inputs that are tapped after appropriate unit delays. The overall length of the PRBS is determined by the number of unit delays used. The PRBS waveform is thus dependent on the clock period $T_{clk} = \frac{1}{f_{clk}}$ and the number of unit delays n. Figure 3.7 illustrates the implementation of a PRBS shift register in Simulink, where n= 4, with a period length of $N = 15$ bits.

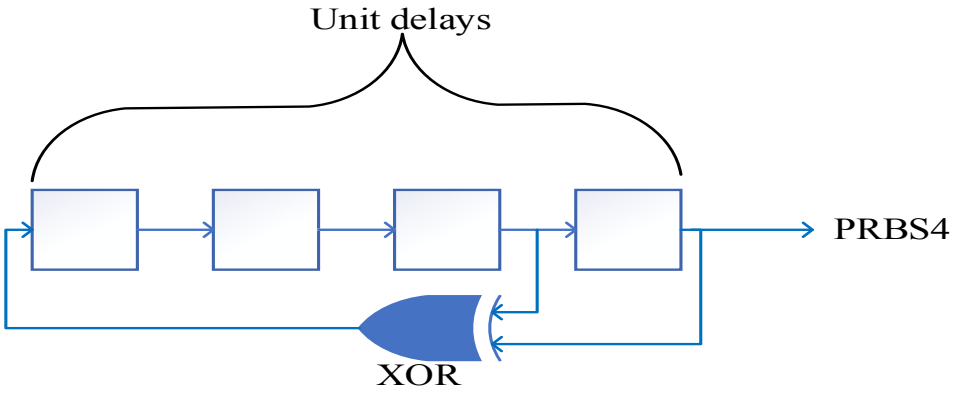

Figure 3.7: Implementation of a feedback shift register with n= 4 in Simulink.

3.3.2 Simulation of the pseudo-random impulse sequences in Simulink

Figure 3.8 and Figure 3.9 show block diagrams for simulating the unipolar and bipolar PRIS waveforms defined by (3.11) and (3.13) respectively in Simulink, using a feedback shift register n= 4, zero-crossing detection, transfer function blocks to implement the exponential functions, and a switch to select the alternative positive and negative time-shifted exponential functions. The two *HitCrossing* blocks detect the rising and falling edges respectively of the PRBS, thereby generating pseudo-random pulses. These pulses act as inputs to exponential transfer functions with time constants τ_1 and τ_2, which are summed to generate an impulse signal as defined by (3.1). A switch block with three inputs is used to generate a bipolar PRIS. The switch is configured to pass a signal into the top input port when the input into the middle port satisfies a selected criterion, otherwise the signal into the bottom input port is passed. In the case of the PRIS, the signal into the top input consists of a sequence of unchopped positive impulses occuring on every rising edge of the PRBS waveform. The signal into the bottom input port consists of a sequence of unchopped negative impulse waveforms. The signal into the middle port is a PRBS which controls the switching operation. Whenever there is a rising edge on the PRBS, a positive impulse waveform is passed, which is chopped when the PRBS logic changes. A negative impulse is passed at the falling edge of the PRBS, which is then chopped when the PRBS logic changes.

Figure 3.10 shows PRBS and PRIS waveforms simulated in Simulink using a model similar to the one shown in Figure 3.9, for f_{clk}= 10 kHz, $\tau_1 = 0.05T_{clk}$ and $\tau_2 = 0.4T_{clk}$.

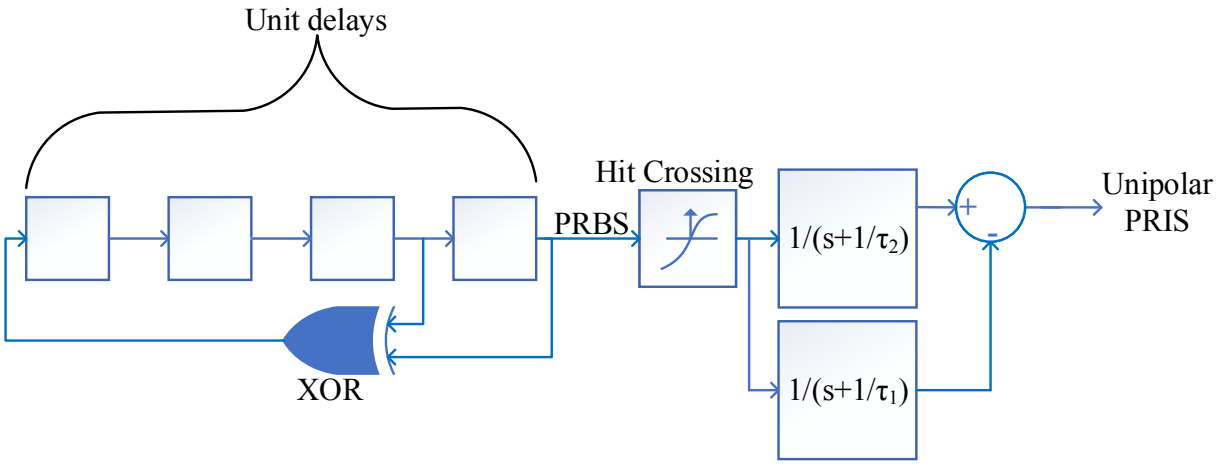

Figure 3.8: Simulink model for simulating a unipolar PRIS with n= 4.

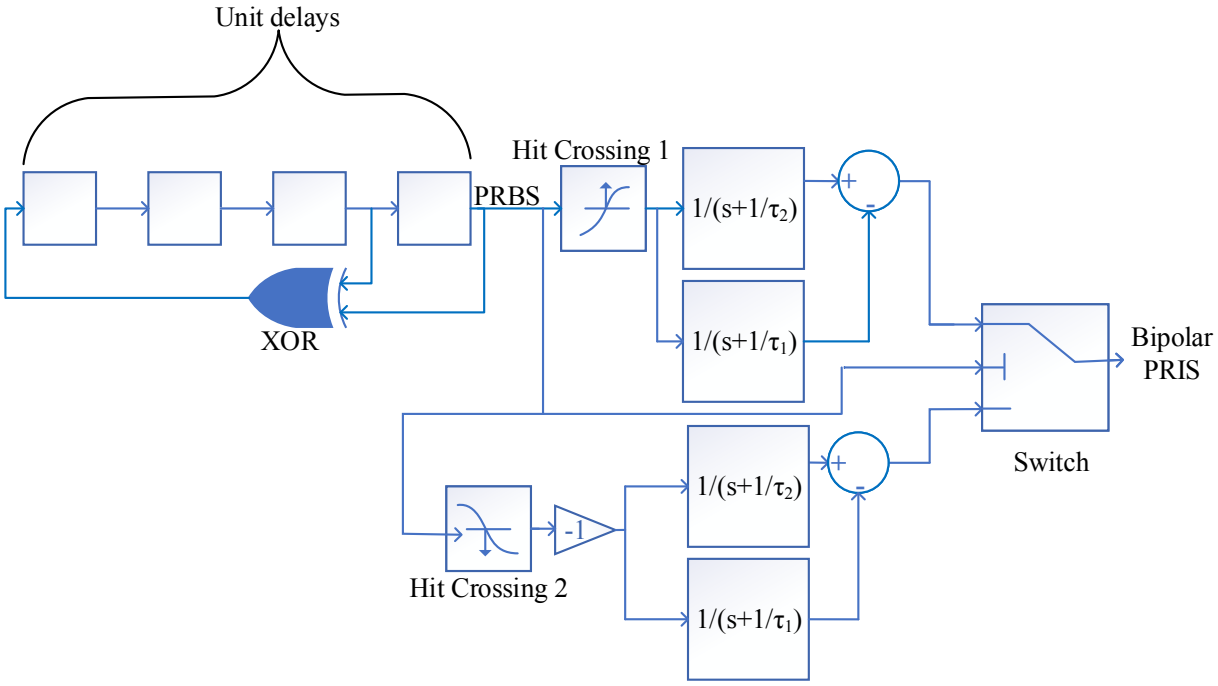

Figure 3.9: Simulink model for simulating a bipolar PRIS with n= 4.

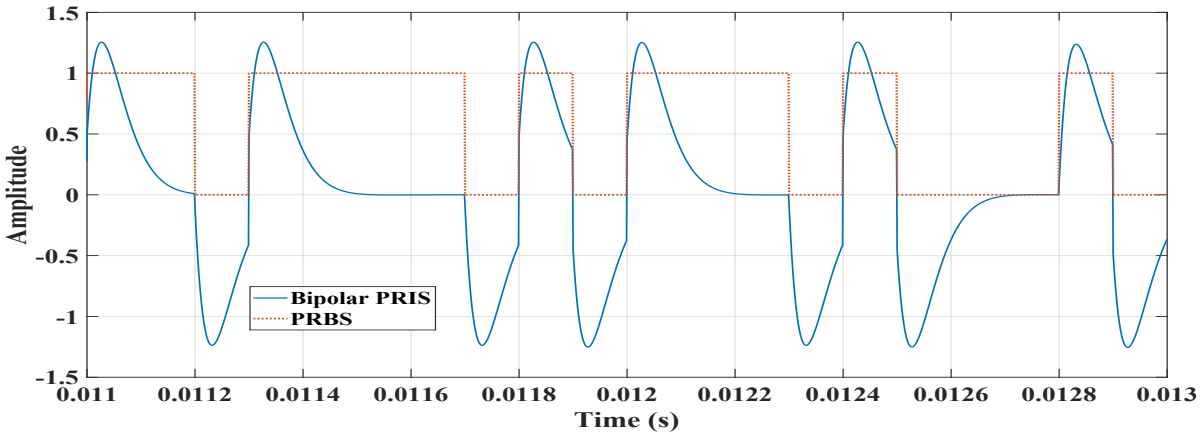

Figure 3.10: Simulated PRBS and bipolar PRIS waveforms using the Simulink model shown in Figure 3.9.

3.4 Conclusion

A novel concept of a PRIS as a perturbation signal is introduced. The signal is derived from the classical impulse waveform and the PRBS. By initiation the impulse waveform at each state transition of the PRBS and chopping it at the next PRBS state transition, a PRIS signal is developed. The PRIS waveform consists of a sequence of randomly occurring, randomly chopped impulses. The two variations of the PRIS, the unipolar and bipolar PRIS signals are introduced and the time-domain analysis presented. It is shown that the time-domain characteristics of the PRIS can be controlled by varying the clock frequency and the length of the PRBS as well as the

two time constants associated with the classical impulse waveform. An approach of simulating the proposed PRIS waveform using the Simulink platform is also presented.

CHAPTER 4

Frequency-Domain Modelling of the Pseudo-Random Impulse Sequence

4.1 Introduction

System identification and parameter estimation applications require the implementation of a perturbation signal with suitable frequency-domain properties. In this chapter, the proposed PRIS signal is modelled and analyzed in the frequency-domain. The results are discussed in the context of the suitability of the PRIS for system identification and parameter estimation applications in the field of power engineering.

4.2 Mathematical modelling of the pseudo-random impulse sequence in the frequency-domain

4.2.1 Time-shifted impulse waveform

The Fourier transform of the time-shifted impulse waveform $f_i(t-t_i)$ defined by (3.2) can be obtained by applying the Fourier integral as follows

$$F_{i,t_i}(\omega) = U\int_{t_i}^{\infty}\left[e^{-\frac{(t-t_i)}{\tau_2}} - e^{-\frac{(t-t_i)}{\tau_1}}\right]e^{-j\omega t}dt \tag{4.1}$$

Equation(4.1) can be expressed as

$$F_{i,t_i}(\omega) = U\int_{t_i}^{\infty} e^{-\frac{(t-t_i)}{\tau_2}}e^{-j\omega t}dt - U\int_{t_i}^{\infty} e^{-\frac{(t-t_i)}{\tau_1}}e^{-j\omega t}dt \tag{4.2}$$

The integrals in (4.2) can be solved to yield

$$F_{i,t_i}(\omega) = \frac{-Ue^{\frac{t_i}{\tau_2}}}{\frac{1}{\tau_2}+j\omega}\left[e^{-t(\frac{1}{\tau_2}+j\omega)}\right]_{t_i}^{\infty} + \frac{Ue^{\frac{t_i}{\tau_1}}}{\frac{1}{\tau_1}+j\omega}\left[e^{-t(\frac{1}{\tau_1}+j\omega)}\right]_{t_i}^{\infty} \tag{4.3}$$

Equation 4.3 can be further formulated to obtain

$$F_{i,t_i}(\omega) = U\left[\frac{e^{-j\omega t_i}}{\frac{1}{\tau_2}+j\omega} - \frac{e^{-j\omega t_i}}{\frac{1}{\tau_1}+j\omega}\right] \tag{4.4}$$

The righthand side of (4.4) can be simplified to yield the expression

$$F_{i,t_i}(\omega) = Ue^{-j\omega t_i}\left[\frac{\tau_2-\tau_1}{(1+j\omega\tau_1)(1+j\omega\tau_2)}\right]. \tag{4.5}$$

4.2.2 Time-shifted pulse waveform

The Fourier transform of the time-shifted pulse waveform $f_{p,t_i,t_{i+1}}(t)$ defined by (3.3) is given by the expression

$$f_{p,t_i,t_{i+1}}(t) = u(t-t_i) - u(t-t_{i+1}) \Leftrightarrow \left[e^{-j\omega t_i}(\pi\delta(\omega) - \frac{j}{\omega})\right] - \left[e^{-j\omega t_{i+1}}(\pi\delta(\omega) - \frac{j}{\omega})\right]. \quad (4.6)$$

The righthand side of (4.6) can be rearranged to yield

$$F_{p,t_i,t_{i+1}}(\omega) = (\pi\delta(\omega) - \frac{j}{\omega})(e^{-j\omega t_i} - e^{-j\omega t_{i+1}}). \quad (4.7)$$

4.2.3 Time-shifted chopped impulse waveform

The Fourier transform of the chopped time-shifted impulse waveform $f_{ic}(t-t_i)$ defined by (3.4) is obtained by convolution of the Fourier transforms $F_{i,t_i}(\omega)$ and $F_{p,t_i,t_{i+1}}(\omega)$ defined by (4.5) and (4.7) respectively. This yields

$$f_{ic}(t-t_i) \Leftrightarrow F_{ic,t_i,t_{i+1}}(\omega) = Ue^{-j\omega t_i}\left[\frac{\tau_2-\tau_1}{(1+j\omega\tau_2)(1+j\omega\tau_1)}\right] * \left[(\pi\delta(\omega) - \frac{j}{\omega})(e^{-j\omega t_i} - e^{-j\omega t_{i+1}})\right]. \quad (4.8)$$

Alternatively, the frequency domain expression of the chopped time-shifted impulse waveform can be obtained by applying the Fourier integral to the time-shifted impulse waveform $f_i(t-t_i)$ defined by (3.2) on a closed interval t_i to t_{i+1} as follows

$$F_{ic,t_i,t_{i+1}}(\omega) = U\int_{t_i}^{t_{(i+1)}} \left[e^{-\frac{(t-t_i)}{\tau_2}} - e^{-\frac{(t-t_i)}{\tau_1}}\right]e^{-j\omega t}dt \quad (4.9)$$

Equation (4.9) can be solved to yield

$$F_{ic,t_i,t_{i+1}}(\omega) = \frac{-Ue^{\frac{t_i}{\tau_2}}}{\frac{1}{\tau_2}+j\omega}\left[e^{-t(\frac{1}{\tau_2}+j\omega)}\right]_{t_i}^{t_{i+1}} + \frac{Ue^{\frac{t_i}{\tau_1}}}{\frac{1}{\tau_1}+j\omega}\left[e^{-t(\frac{1}{\tau_1}+j\omega)}\right]_{t_i}^{t_{i+1}} \quad (4.10)$$

Equation (4.10) can be solved to yield

$$F_{ic,t_i,t_{i+1}}(\omega) = \frac{-Ue^{\frac{t_i}{\tau_2}}}{\frac{1}{\tau_2}+j\omega}\left[e^{-t_{i+1}(\frac{1}{\tau_2}+j\omega)} - e^{-t_i(\frac{1}{\tau_2}+j\omega)}\right] + \frac{Ue^{\frac{t_i}{\tau_1}}}{\frac{1}{\tau_1}+j\omega}\left[e^{-t_{i+1}(\frac{1}{\tau_1}+j\omega)} - e^{-t_i(\frac{1}{\tau_1}+j\omega)}\right] \quad (4.11)$$

By simplifying (4.11), the following expression can be obtained

$$F_{ic,t_i,t_{i+1}}(\omega) = \frac{U\left[e^{-j\omega t_i} - e^{\frac{t_i}{\tau_2}-t_{i+1}(\frac{1}{\tau_2}+j\omega)}\right]}{\frac{1}{\tau_2}+j\omega} - \frac{U\left[e^{-j\omega t_i} - e^{\frac{t_i}{\tau_1}-t_{i+1}(\frac{1}{\tau_1}+j\omega)}\right]}{\frac{1}{\tau_1}+j\omega} \quad (4.12)$$

By simplifying (4.12) further, the frequency-domain expression of the chopped time-shifted impulse waveform can be obtained as

$$F_{ic,t_i,t_{i+1}}(\omega) = \frac{A\tau_1\tau_2(\frac{1}{\tau_1}+j\omega) - B\tau_1\tau_2(\frac{1}{\tau_2}+j\omega)}{(1+j\omega\tau_1)(1+j\omega\tau_2)}. \quad (4.13)$$

where

$$A = U\left[e^{-j\omega t_i} - e^{\frac{t_i}{\tau_2} - t_{i+1}(\frac{1}{\tau_2}+j\omega)}\right]. \tag{4.14}$$

and

$$B = U\left[e^{-j\omega t_i} - e^{\frac{t_i}{\tau_1} - t_{i+1}(\frac{1}{\tau_1}+j\omega)}\right]. \tag{4.15}$$

4.2.4 Unipolar pseudo-random impulse sequence

The unipolar PRIS, $f^U_{PRIS}(t)$, consists of a pseudo-random sequence of time-shifted impulses, as defined by (3.11). By using the superposition property of the Fourier transform, the Fourier transform, $F^U_{PRIS}(\omega)$, of $f^U_{PRIS}(t)$ can be expressed as

$$F^U_{PRIS}(\omega) = \sum_{i=0,1,2\ldots}^{((N+1)/2)} Ue^{-j\omega t_i}\left[\frac{\tau_2 - \tau_1}{(1+j\omega\tau_2)(1+j\omega\tau_1)}\right] * \left[(\pi\delta(\omega) - \frac{j}{\omega})(e^{-j\omega t_i} - e^{-j\omega t_{i+1}})\right]. \tag{4.16}$$

Using (4.13), the frequency domain expression for the unipolar PRIS can also be expressed as

$$F^U_{PRIS}(\omega) = \sum_{i=0,1,2\ldots}^{((N+1)/2)} \frac{A\tau_1\tau_2(\frac{1}{\tau_1}+j\omega) - B\tau_1\tau_2(\frac{1}{\tau_2}+j\omega)}{(1+j\omega\tau_1)(1+j\omega\tau_2)}. \tag{4.17}$$

Equations (4.16) and (4.17) show that the spectral characteristics of the unipolar PRIS are dependent on the amplitude U and time constants τ_1 and τ_2 of the exponential functions that constitute the impulse, and the pseudo-random time variables t_i and t_{i+1}, which are functions of the clock frequency f_{clk}.

4.2.5 Bipolar pseudo-random impulse sequence

The bipolar PRIS, $f^B_{PRIS}(t)$, consists of a pseudo-random sequence of alternating positive and negative time-shifted, chopped impulse waveforms, as defined by (3.13). The Fourier transform of the sequence of positive time-shifted chopped impulses can be expressed as

$$F^P_i(\omega) = \sum_{i=0,2,4\ldots}^{((N+1)/2)-1} Ue^{-j\omega t_i}\left[\frac{\tau_2 - \tau_1}{(1+j\omega\tau_2)(1+j\omega\tau_1)}\right] * \left[(\pi\delta(\omega) - \frac{j}{\omega})(e^{-j\omega t_i} - e^{-j\omega t_{i+1}})\right]. \tag{4.18}$$

or by using (4.13) the Fourier transform of the sequence of positive chopped time-shifted impulses can also be expressed as

$$F^P_i(\omega) = \sum_{i=0,2,4\ldots}^{((N+1)/2)-1} \frac{A\tau_1\tau_2(\frac{1}{\tau_1}+j\omega) - B\tau_1\tau_2(\frac{1}{\tau_2}+j\omega)}{(1+j\omega\tau_1)(1+j\omega\tau_2)}. \tag{4.19}$$

The Fourier transform of the sequence of negative time-shifted chopped impulses can be expressed as

$$F_i^N(\omega) = -\sum_{i=1,3,5...}^{((N+1)/2)} Ue^{-j\omega t_i}\left[\frac{\tau_2-\tau_1}{(1+j\omega\tau_2)(1+j\omega\tau_1)}\right] * \left[(\pi\delta(\omega)-\frac{j}{\omega})(e^{-j\omega t_i}-e^{-j\omega t_{i+1}})\right]. \quad (4.20)$$

Equation(4.20) can also be expressed as

$$F_i^N(\omega) = -\sum_{i=1,3,5...}^{((N+1)/2)} \frac{A\tau_1\tau_2(\frac{1}{\tau_1}+j\omega)-B\tau_1\tau_2(\frac{1}{\tau_2}+j\omega)}{(1+j\omega\tau_1)(1+j\omega\tau_2)}. \quad (4.21)$$

The frequency spectrum of the bipolar PRIS is thus obtained by summing the Fourier transforms of the sequences of positive and negative time-shifted chopped impulses. This yields

$$\begin{aligned} F_{PRIS}^B(\omega) = &\sum_{i=0,2,4...}^{((N+1)/2)-1} Ue^{-j\omega t_i}\left[\frac{\tau_2-\tau_1}{(1+j\omega\tau_2)(1+j\omega\tau_1)}\right] \\ &* \left[(\pi\delta(\omega)-\frac{j}{\omega})(e^{-j\omega t_i}-e^{-j\omega(t_{i+1})})\right] \\ &-\sum_{i=1,3,5...}^{((N+1)/2)} Ue^{-j\omega t_i}\left[\frac{\tau_2-\tau_1}{(1+j\omega\tau_2)(1+j\omega\tau_1)}\right] \\ &* \left[(\pi\delta(\omega)-\frac{j}{\omega})(e^{-j\omega t_i}-e^{-j\omega t_{i+1}})\right]. \end{aligned} \quad (4.22)$$

Equation(4.22) can also be expressed as

$$F_{PRIS}^B(\omega) = \sum_{i=0,2,4...}^{((N+1)/2)-1} \frac{A\tau_1\tau_2(\frac{1}{\tau_1}+j\omega)-B\tau_1\tau_2(\frac{1}{\tau_2}+j\omega)}{(1+j\omega\tau_1)(1+j\omega\tau_2)} - \sum_{i=1,3,5...}^{((N+1)/2)} \frac{A\tau_1\tau_2(\frac{1}{\tau_1}+j\omega)-B\tau_1\tau_2(\frac{1}{\tau_2}+j\omega)}{(1+j\omega\tau_1)(1+j\omega\tau_2)}. \quad (4.23)$$

Equation (4.23) shows that the spectral characteristics of the bipolar PRIS are dependent on the amplitude U and time constants τ_1 and τ_2 of the exponential functions that constitute the impulse, and the random time variables t_i and t_{i+1}, which are functions of the clock frequency f_{clk}.

4.3 Spectral properties of the pseudo-random impulse sequence

4.3.1 Introduction

The mathematical expressions derived for the Fourier transform of the unipolar and bipolar pseudo-random sequences, i.e. (4.17) and (4.23) respectively, are complex. The parameters denoted by t_i and t_{i+1} are, furthermore, pseudo-random variables that have to be expressed with reference to the properties of the PRBS that generates the sequences. This represents a major complication in deriving closed-form mathematical expressions for the frequency spectrums associated with these signals. A simulation approach is therefore adopted to investigate

the spectral properties of the PRIS. This approach involves simulation of time-domain representations of the PRIS, using Simulink models as proposed in section 3.3, followed by spectral analysis. A parametric approach is adopted, whereby parameters such as the PRBS clock frequency f_{clk} and the impulse time constants τ_1 and τ_2 are varied with the view to investigate the effects of these parameters on the spectral properties of interest. This approach, furthermore, supports the design processes associated with implementing a practical PRIS source for a given application well.

The objective of spectral estimation is to determine how the total power from a finite length of a stationary data sequence is distributed over frequency. There are two broad classes of spectral estimators, namely nonparametric or classical methods, and parametric methods. Parametric methods assume a model for the data, which then provides a way of parameterising the spectrum by estimating the parameters for the assumed model. Parametric methods may offer more accurate estimates compared to the nonparametric methods for cases where the data satisfy the assumed model. Parametric methods are, however, sensitive to incorrectly specified models. It is also more likely that the data does not satisfy the chosen model, making nonparametric methods outperform the parametric ones [50].

The behaviour of a random signal, such as the proposed PRIS can be described in terms of its statistical information. This makes it possible to characterise the signal in terms of a Power Spectral Density (PSD), using the autocorrelation function, $R_{xx}(\tau)$, of the signal. The PSD, $P_{xx}(f)$, of a signal $x(t)$ is defined by the relationships [36], [51]

$$P_{xx}(f) = \int_{-\infty}^{\infty} R_{xx}(\tau) e^{-j2\pi f\tau} d\tau, \tag{4.24}$$

and

$$R_{xx}(\tau) = \lim_{T\to\infty} \frac{1}{T} \int_{-\infty}^{\infty} x(t)x(t+\tau)d\tau, \tag{4.25}$$

where $R_{xx}(\tau)$ denotes the autocorrelation function of the signal.

Equation (4.24) shows that Power Spectral Density (PSD) represents the Fourier transform of the autocorrelation function of a signal. In practice, the PSD has to be estimated using a finite temporal frame size of the sampled data. Truncation and sampling, however, introduce leakage and aliasing problems [50]. Measured data are, furthermore, often contaminated by noise, and some form of averaging may be required to obtain consistent results by eliminating stochastic noise components. PSD is typically estimated using a classical spectral estimator in combination with an appropriate window function. Windowing reduces leakage and measurement noise. The magnitude of the PSD at frequencies far from the signal frequency, i.e. the leakage or sidelobe magnitude, at the expense of an increased bandwidth of the main lobe. The

variance and bias of the estimator represent two of the most important considerations when choosing an estimator. Others considerations include the mean and computational complexity. The bias is defined as the difference between the expected value obtained with estimator and the true value of the estimated parameter. Variance is defined as the mean square value minus the square of the mean of the estimated parameter. Choosing a suitable estimator requires a compromise between bias and variance errors. Reducing the bias, thereby improving resolution and dynamic range, increases the variance, thereby increasing the noise, and vice versa [52], [50].

Some of the popular non-parametric power spectral estimators are summarised below:

- **Periodogram** : The periodogram is relatively simple to implement, but it represents an inconsistent estimator in the sense that, although the mean value of the estimated parameter converges to the true PSD value as the data frame becomes large, the variance is constant and does not decrease with the length of the data record [52]. The variance of the periodogram estimate is, furthermore, not a function of the window used to suppress leakage.
- **Blackman-Tukey**: The performance of the periodogram can be improved by weighting the autocorrelation estimates with a real sequence, known as a lag window. This reduces the variance of the spectral estimator at the expense of increasing the bias. The lag windows commonly used in this method include the rectangular window, Bartlett window, Hann window, Hamming window and Blackman window. The chosen window should reduce leakage effects sufficiently, and the window length is chosen to achieve a compromise between spectral resolution and variance [52], [50].
- **Bartlett**: The Bartlett method reduces fluctuations in the periodogram by dividing the available data sample into subsamples, determining the periodogram of each subsample, and then averaging the periodograms obtained from the subsamples. The Bartlett method has a lower spectral resolution compared to the periodogram due to splitting of the data into segments. A reduction in variance is thus expected [53].
- **Welch**: The Welch method refines the Bartlett method in the sense that the data segments are allowed to overlap and that each data segment is windowed before computing the periodogram. There are thus two parameters affecting the quality of the Welch estimation, namely the amount of overlap and length of each segment. Overlapping the data segments decreases the variance while windowing the data segments provides control over the bias, or resolution, of the estimated PSD. The optimum overlap occurs when the variance is at a minimum and depends on the shape of the windowing function used [52], [53].

The Welch method is used in this investigation, as it presents the most parameters for optimising the accuracy of the estimation. The commonly used Hann window, which offers good frequency resolution and reduced spectral leakage is selected. The Hann window has lower sidelobes compared to many of the other window types, which offers a better dynamic range. An overlap percentage of 62.5% is used, as it represents the optimum overlap percentage for the Hann window, as shown by Najafi *et al* [50].

In order to verify the performance of the simulation approach proposed above, the spectrum derived by estimation from a PRIS waveform simulated using the time-domain model shown in Figure 3.9 is compared to the spectrum obtained from (4.23). To obtain the analytical frequency curve from (4.23), the random variable t_i is simulated using random numbers for the chosen PRBS. Figure 4.1 compares the results obtained with the two approaches, for a PRIS with f_{clk}=15kHz, $\tau_1 = 1.5T_{clk}$, $\tau_2 = 5T_{clk}$ and n=4. The results obtained with the two approaches show a good correlation. There are however differences in damping at zero nodes with the simulated waveform indicating more damping as a result of spectral estimation.

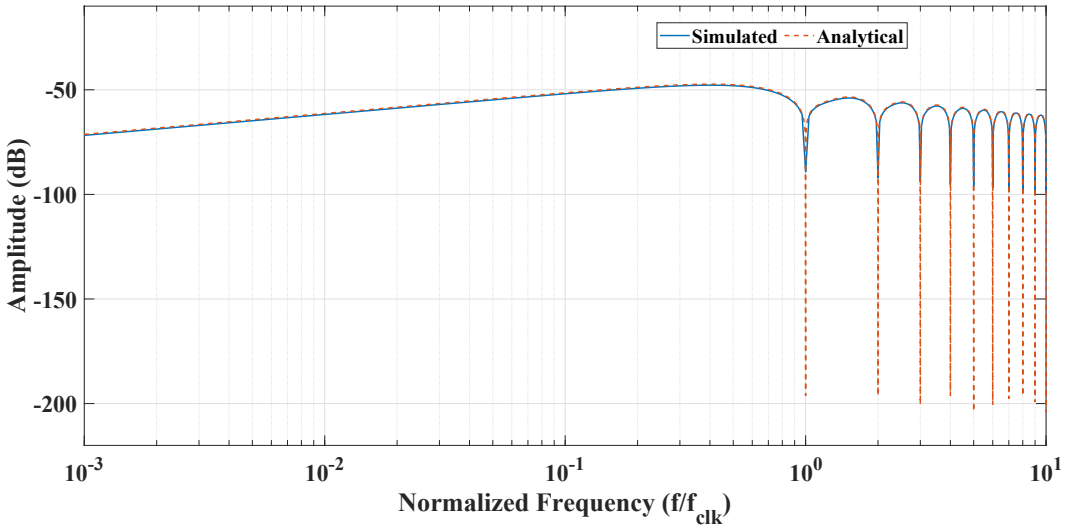

Figure 4.1: Comparison of simulated frequency spectra obtained from a time-domain PRIS waveform and analytical expression from (4.23), for f_{clk}=15kHz, $\tau_1 = 1.5T_{clk}$ and $\tau_2 = 5T_{clk}$.

4.3.2 Spectral properties of the impulse waveform.

The frequency-domain properties of the classical impulse waveform are of interest in the context of this investigation, as it has a significant influence on the frequency spectrum of the associated PRIS. In this section, the properties of the impulse waveform are demonstrated through parametric simulations of the time-domain waveform defined by (3.1) and the associated frequency response for the impulse waveform which can be expressed as

$$F_i(\omega) = U\Big[\frac{\tau_2 - \tau_1}{(1 + j\omega\tau_1)(1 + j\omega\tau_2)}\Big]. \tag{4.26}$$

Figures 4.2(a) and 4.2(b) show the simulated time-domain waveform and the associated frequency response curves for the impulse waveform plotted for varying values of τ_1 with τ_2 fixed at 100μs. These results show that as the ratio $\frac{\tau_2}{\tau_1}$ increases, which indicates a decreasing value of τ_1, the amplitude of the time-domain impulse waveform increases. This, consequently, results in higher spectral energy levels as τ_1 decreases. Figures 4.3(a) and 4.3(b), on the other hand, show the simulated time-domain waveform and the associated frequency response curves for the impulse waveform plotted at varying values of τ_2 with τ_1 fixed at 1μs. In this case, it can be seen that high values of τ_2 relative to τ_1 result in higher spectral energy levels. As $\frac{\tau_1}{\tau_2}$ decreases, the amplitude of both the time-and frequency-domain responses drops. These effects of the time constants on amplitude of the impulse waveform agree with (3.9) which presents the relationship between the impulse peak magnitude value and the time constants.

The frequency spectrum of the impulse waveform, however, decays rapidly with frequency as shown in Figures 4.2(b) and 4.3(b). This results in low spectral energy, and therefore low SNR, at higher frequencies. As a result, in the context of parameter estimation, a high impulse amplitude may be required to improve the SNR. This increases the crest factor, which may cause interference with the normal operation of the system under test.

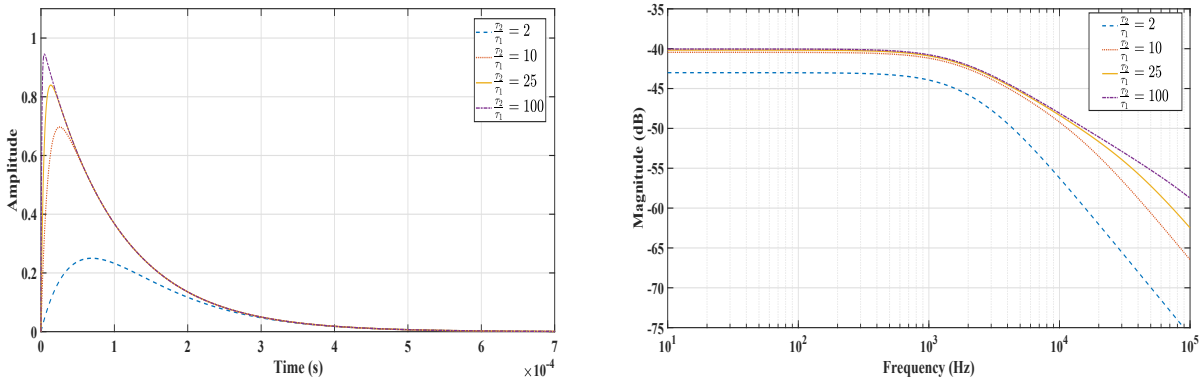

(a) Time-domain impulse waveform

(b) Spectrum of the Impulse waveform

Figure 4.2: Simulated time- and frequency responses of the impulse waveform for varying values of τ_1 with τ_2 fixed at 100μs

4.3.3 Comparison of the spectral properties of the PRBS and the bipolar PRIS

Figure 4.4 compares the estimated frequency spectrums of a unipolar PRBS and bipolar PRIS for $\tau_1 = 1.5T_{clk}$, $\tau_2 = 5T_{clk}$ and f_{clk}=15 kHz. Whereas the PRBS presents a flat spectrum in

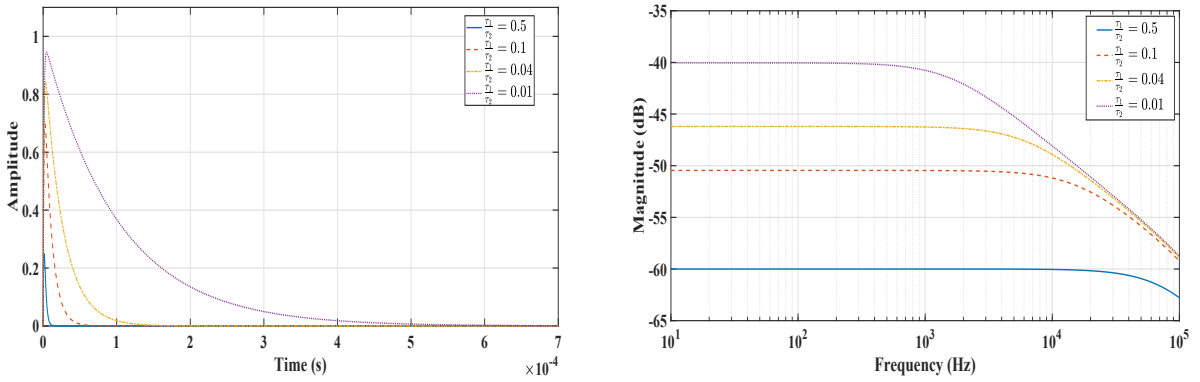

(a) Time-domain impulse waveform

(b) Spectrum of the Impulse waveform

Figure 4.3: Simulated time- and frequency responses of the impulse waveform for varying values of τ_2 with τ_1 fixed at 1μs

the frequency range below f_{clk}, the bipolar PRIS exhibits a bandpass frequency characteristic where the energy is focused in a band centred around $f = \frac{f_{clk}}{3}$. The upper side lobes of both the PRBS and bipolar PRIS have a width of f_{clk}, with minima located at integer multiples of f_{clk}. As will be shown in the following sections, the shape of the PRIS spectrum is a function of τ_1, τ_2 and f_{clk}. These parameters can, therefore, be used to focus the spectral energy of the bipolar PRIS into a specific band. Compared to PRBS, the amplitude of the bipolar PRIS spectrum drops towards the lower frequencies. The bipolar PRIS, therefore, offers an advantage for applications where a low dc component is desirable, e.g. electromagnetic systems such as transformer and electrical machine windings,

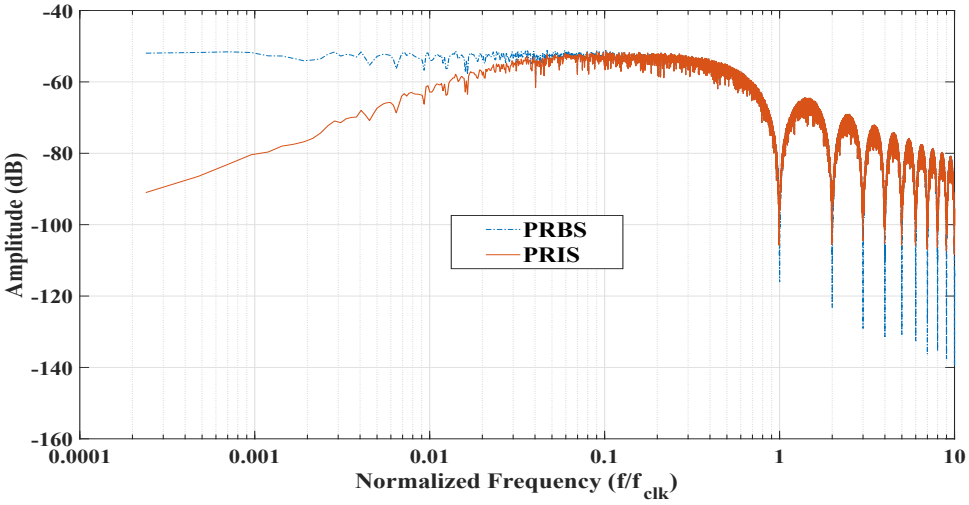

Figure 4.4: Simulated power spectral densities of the PRBS and bipolar PRIS for $\tau_1 = 1.5T_{clk}$, $\tau_2 = 5T_{clk}$ and f_{clk}=15 kHz.

4.3.4 Effects of the clock frequency on the spectral properties of the bipolar PRIS

The effects of the clock frequency, f_{clk}, on the spectral properties of the bipolar PRIS are investigated by observing PSDs obtained from PRIS signals generated with different values of f_{clk} and fixed values of τ_1 and τ_2. Figure 4.5 shows simulated PSDs of the bipolar PRIS for f_{clk} values of 10 kHz, 15 kHz and 30 kHz, with $\tau_1 = 1\mu$s and $\tau_2 = 100\mu$s. As expected, the results show that the bandwidth of the main lobe increases as f_{clk} increases. This is accompanied by a moderate upwards shift in the magnitude around the region where the spectral energy is focused. In the low-frequency range, lower values of f_{clk} exhibit higher levels of spectral energy compared to higher values of f_{clk}. The results suggest that the clock frequency can be used to shape the spectrum of the PRIS such that the spectral energy is focussed around the frequency band of interest. This is useful for system identification applications, such as control design, where it is desirable to obtain an accurate model around the crossover frequency.

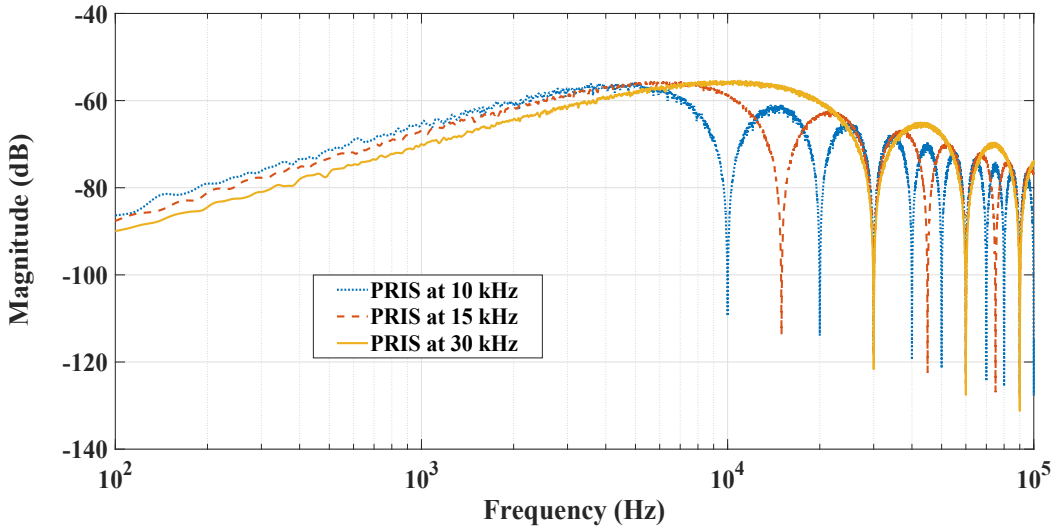

Figure 4.5: Effects of the clock frequency, f_{clk}, on the frequency spectrum of the bipolar PRIS, for $\tau_1 = 1\mu$s and $\tau_2 = 100\mu$s.

4.3.5 Effects of the impulse rise-time constant on the spectral properties of the bipolar PRIS

The effects of the PRIS rise-time constant, τ_1, on the spectral properties of the bipolar PRIS are investigated by observing PSDs obtained from PRIS signals generated with different values of τ_1 and fixed values of f_{clk} and τ_2. Figure 4.6 shows simulated PSDs of the bipolar PRIS for $\tau_1 = 0.1T_{clk}$, $\tau_1 = T_{clk}$, $\tau_1 = 10T_{clk}$ and $\tau_1 = 100T_{clk}$, with $f_{clk} = 15$kHz and $\tau_2 = 0.1T_{clk}$. The results show that a lower impulse rise-time constant increases the average level of spectral

energy substantially. The is attributed to the fact that a lower ratio of $\frac{\tau_1}{\tau_2}$ increases the maximum values reached by the impulse waveforms associated with the PRIS waveform, before being chopped by the PRBS state transitions, thereby increasing the total spectral energy. The relationship between U_{max} and the two time constants is indicated in (3.9). The effects of τ_1 on the PRIS spectrum can also be interpreted with reference to the relationships expressed in (3.9) and (4.23). Low values of τ_1 result in high magnitudes of the frequency components in the spectrum of the PRIS.

The results presented in Figure 4.6, furthermore, suggest that the impulse rise-time constant does not have a major effect on the shape of the frequency spectrum of the PRIS.

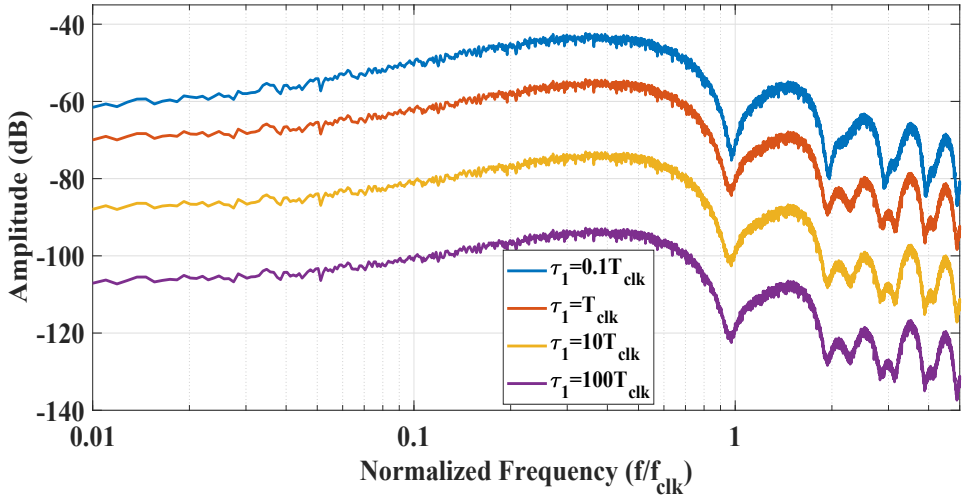

Figure 4.6: Effects of the impulse rise-time constant, τ_1, on the frequency spectrum of the bipolar PRIS, for $f_{clk} = 15$kHz and $\tau_2 = 0.1T_{clk}$.

4.3.6 Effects of the impulse fall-time time constant on the spectral properties of the bipolar PRIS

The effects of the PRIS fall-time constant, τ_2, on the spectral properties of the bipolar PRIS are investigated by observing PSDs obtained from PRIS signals generated with different values of of τ_2 and fixed values of f_{clk} and τ_1. Figure 4.7 shows simulated PSDs of the bipolar PRIS for $\tau_2 = 0.1T_{clk}$, $\tau_2 = T_{clk}$, $\tau_2 = 10T_{clk}$ and $\tau_2 = 100T_{clk}$, with $f_{clk} = 15$kHz and $\tau_1 = 0.1T_{clk}$. The results show that a lower impulse fall-time constant decreases the spectral energy in the low frequency band. Overall, this results in a more defined focus of the spectral energy in a specific frequency band.

The impulse fall-time constant does not, however, have a major effect on the spectral energy around the frequency of maximum energy for $\tau_2 > T_{clk}$. This is expected because as τ_2 increases, the PRIS starts to resemble the PRBS.

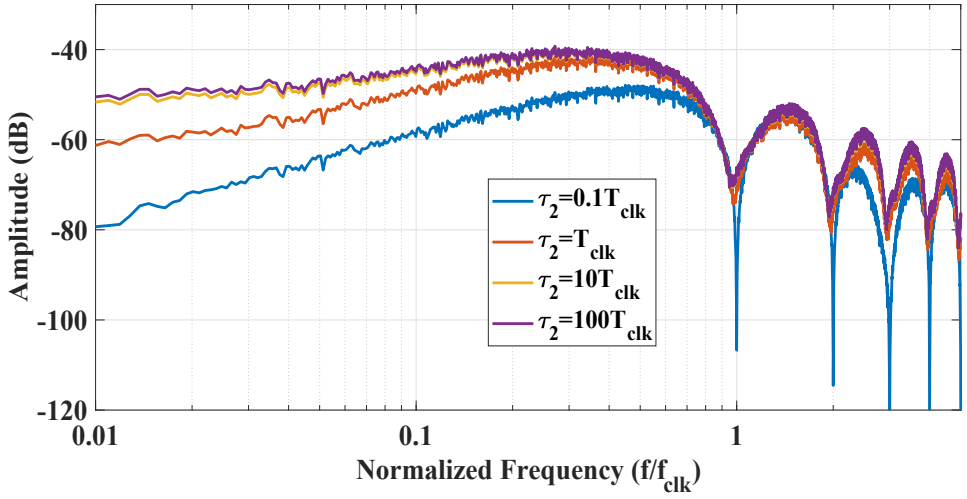

Figure 4.7: Effects of the impulse fall-time constant, τ_2, on the frequency spectrum of the bipolar PRIS, for $f_{clk} = 15$kHz and $\tau_1 = 0.1T_{clk}$.

4.4 Conclusion

This chapter begins by deriving the frequency-domain mathematical expression of the proposed PRIS waveform. The derived expression shows that the frequency spectrum of the PRIS is dependent on the amplitude and the two time constants that make up the impulse, and the PRBS clock frequency.

Spectral estimation presents a problem of determining the spectral content of a random process from a finite set of recorded data from that process. The power spectral density function, that describes the distribution of power with the frequency of a random process, is introduced and popular classical estimators discussed. It is noted that it is necessary to strike a balance between bias and variance of the estimator.

The spectral properties of the classical impulse waveform, the PRBS and the proposed PRIS waveforms are presented and discussed. It is clear from the presented results that the wideband frequency response characteristics of the PRIS are strong functions of the chosen PRBS clock frequency and impulse time constants. These parameters can be adjusted to control the spectral characteristics of the PRIS, thus providing a fair degree of signal controllability in comparison to popular perturbation signals such as swine sweep, impulse and the PRBS. The PRBS,

for example, has a flat frequency spectrum below the -3dB point, i.e. white noise. Adjusting the bandwidth of the PRBS does not change this and, thus, does not allow any further focussing of the perturbation energy. The PRIS signal, on the other hand, has f_{clk}, τ_1 and τ_2 that impact on the shape of the frequency spectrum. This is an important aspect of the PRIS which can ensure persistent excitation for a wide range of identification applications.

CHAPTER 5

System Topology, Analysis and Design of Bipolar PRIS Perturbation Source for *In Situ* applications

5.1 Introduction

The bipolar PRIS perturbation signal proposed in this investigation can be generated in practice by the system topology shown in Figure 2.4, by replacing the series impedance Z with an overdamped series RLC circuit. This gives rise to the system topology shown in Figure 5.1, where Z is represented by the series combination of resistor R, capacitor C and inductor L. This topology offers a number of advantages for *in situ* high power, high voltage applications, including the following:

- The circuit can be optimised such that the power losses associated with the series resistance, R, are minimised.
- The AC current component induced in $i_p(t)$ by the AC source can be reduced through filtering, thereby reducing the current ratings of the PRBS voltage source components and the overall power losses.
- The topology offers good control over time constants τ_1 and τ_2, through optimisation of the series reactive circuit elements, i.e. C and L. This facilitates control over the frequency-domain properties of the perturbation signal, as explained in sections 4.3.5 and 4.3.6.

Figure 5.2 shows simulated results for the PRBS voltage signal $v_{prbs}(t)$, perturbation current $i_p(t)$ and target voltage $v_T(t)$ for the system topology shown in Figure 5.1, for $V_{prbs} = 50V$, $R = 50\Omega$, $C = 1\mu$F and $L = 47\mu$H, and a 50 Hz single phase supply network with $V_{Th} = 220V_{rms}$ and $Z_{Th} = 0.4 + j0.25\Omega$. The target is represented by a purely resistive load of $Z_T = 100\Omega$. The results show that the perturbation current, $i_{prbs}(t)$, represents a bipolar PRIS waveform as depicted in Figure 3.6. The current waveform, furthermore, confirm that the 50 Hz sinusoidal component in $i_p(t)$ is reduced significantly compared to the waveform shown in Figure 2.7 for the case of a PRBS voltage source connected through a purely resistive element. The amplitude

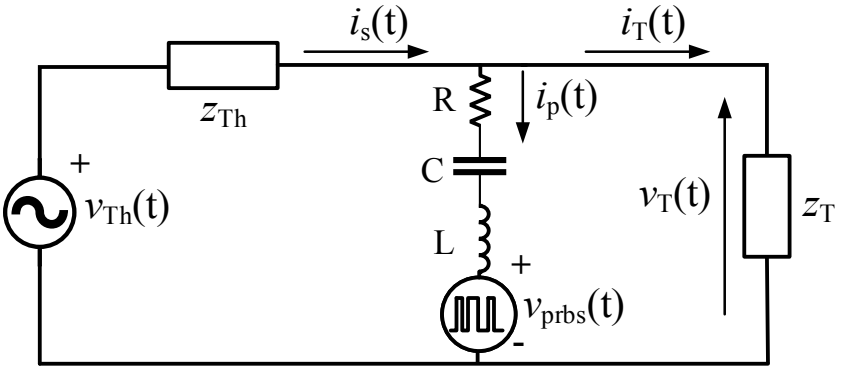

Figure 5.1: System topology of the proposed PRIS source.

of the PRIS current perturbation signal can be controlled by adjusting the PRBS source voltage V_{prbs}, while the spectral energy can be focussed by controlling the PRBS clock frequency and the time constants series RLC network. The mean value of the perturbation current is close to zero.

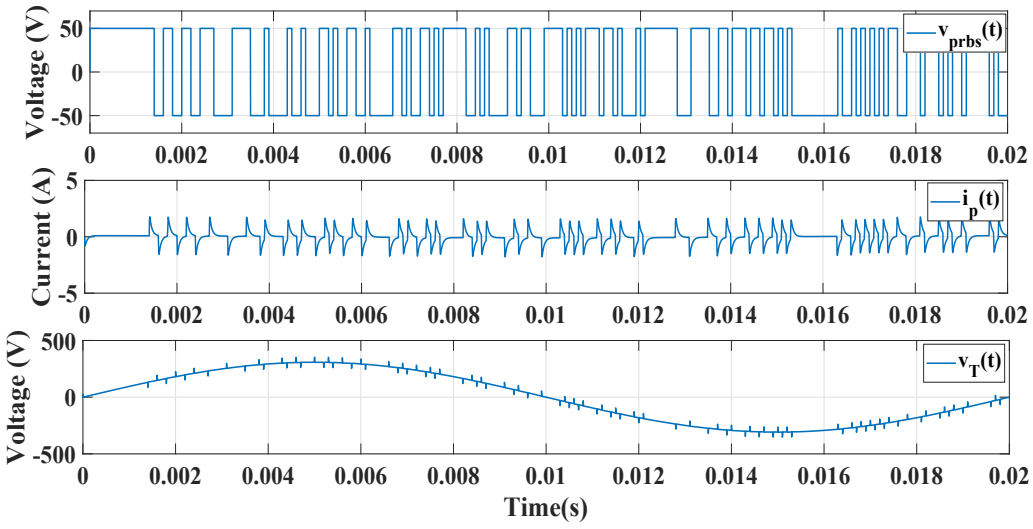

Figure 5.2: Simulated PRBS voltage signal $v_{prbs}(t)$, perturbation current $i_p(t)$ and source voltage $v_T(t)$ for the system topology shown in Figure 5.1, for $n = 14$, $f_{clk} = 15kHz$, $V_{prbs} = 50V$, $R = 50\Omega$, $C = 1\mu$F, and $L = 47\mu$H, $V_{Th} = 220V_{rms}$, $Z_{Th} = 0.4 + j0.25\Omega$ and $Z_T = 100\Omega$.

Figure 5.3 compares the spectral characteristics of the perturbation current signals shown in Figure 2.7 and Figure 5.2. The results show that in comparison with the topology where Z is represented by a resistor, the low frequency components, including the 50Hz component induced by the Thevenin equivalent AC source, are reduced substantially in the case of the PRIS topology. The frequency spectrum of the perturbation current produced by the PRIS source, furthermore, reflects the bandpass characteristic shown in Figure 4.4. Overall, the results con-

firm that the system topology shown in Figure 5.1 has the potential to generate a perturbation current with the time- and frequency-domain properties attributed to the PRIS signal.

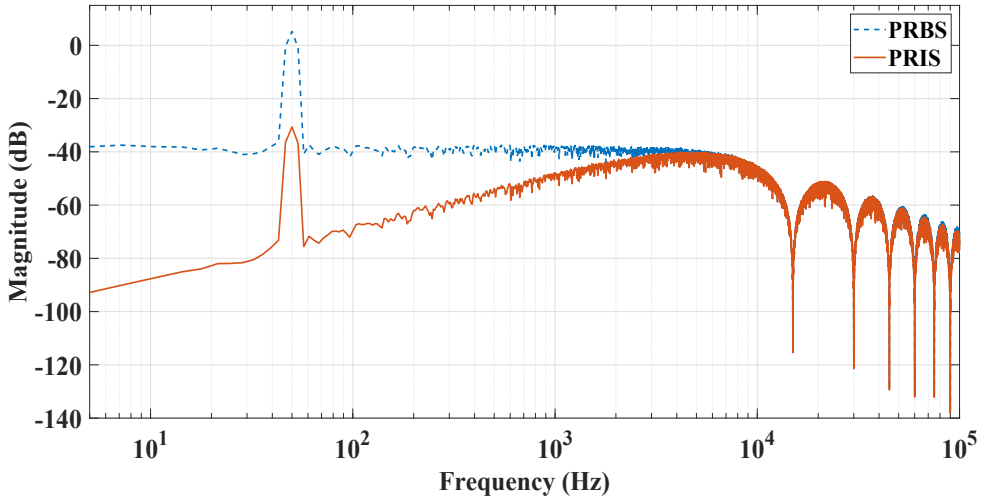

Figure 5.3: Estimated power spectrums of the simulated current perturbation signals obtained with the system topologies shown in Figure 5.1 and Figure 2.6.

5.2 Analysis of the PRIS system topology for *in situ* applications

5.2.1 Introduction

The PRIS source topology proposed in Figure 5.1 essentially applies a DC voltage source, V_{dc}, to the target system through a series RLC arrangement at the state transitions of the PRBS drive signal. The current induced by the PRBS voltage source can be derived by applying the principle of superposition, i.e. by short-circuiting the AC source in the analysis. This gives rise to the circuit topology shown in Figure 5.4, where V_{dc} represents the DC voltage of the PRIS source and Z_L represents the equivalent load impedance reflected by the parallel combination of the Thevenin equivalent source impedance, Z_{Th}, and the target impedance, Z_T. The switch in Figure 5.1 is controlled by a PRBS drive signal.

The circuit topology presented in Figure 5.4 shows that the perturbation current waveform, $i_p(t)$, is not only dependent on the PRBS voltage source and the impedance represented by the series RLC network, but also on the equivalent load impedance, Z_L. The properties of Z_L are, however, typically unknown in practice, and also vary from application to application. The dynamic behaviour of the circuit is therefore analysed for short-circuit conditions, i.e. $Z_L = 0$. While this scenario represents an approximation to the real-world application, it provides valuable insight into the time- and frequency-domain behaviour of the proposed PRIS source

topology. The short-circuit analysis is also useful from a design perspective, as it represents a worst-case scenario with reference to the magnitude of the perturbation current.

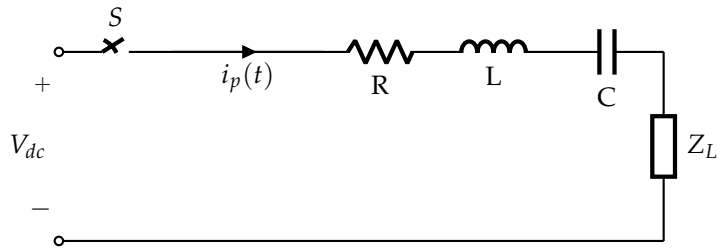

Figure 5.4: Simplified circuit topology for dynamic analysis of the PRIS perturbation system.

5.2.2 Short-circuit analysis of the PRIS source

5.2.2.1 Current waveforms

Under short-circuit conditions, i.e. for $Z_L = 0$, the circuit shown in Figure 5.4 can be represented by the circuit shown in Figure 5.5. Figure 5.6 presents the Laplace domain representation of the circuit shown in Figure 5.5.

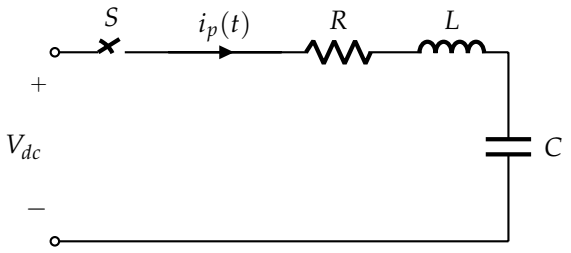

Figure 5.5: Short-circuited circuit topology for dynamic analysis of the PRIS perturbation system.

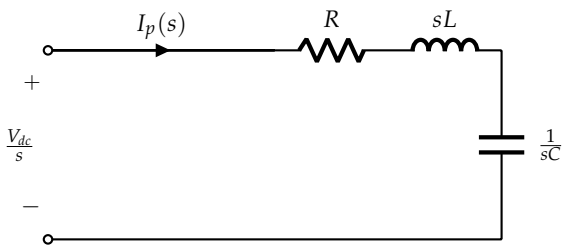

Figure 5.6: Laplace domain representation of the circuit shown in 5.5.

Figure 5.6 gives rise to the following equation in the Laplace domain:

$$\frac{V_{dc}(s)}{s} = I_p(s)R + sLI_p(s) - LI_0 + \frac{I_p(s)}{sC} + \frac{V_0}{s}, \tag{5.1}$$

where I_0 denotes the initial current through the inductor and V_0 denotes the initial voltage across the capacitor. These initial values are determined in practice by the final state of the previous switching interval. Rearranging (5.1) yields the relationship

$$I_p(s) = \frac{\frac{V_{dc}(s)-V_0}{L} + sI_0}{s^2 + \frac{R}{L}s + \frac{1}{LC}}. \tag{5.2}$$

Equation (5.2) represents a single positive impulse waveform of the form shown in Figure 3.1. The denominator in (5.2) represents the characteristic equation of a series RLC circuit. The roots of this equation are given by

$$\frac{1}{\tau_{1,2}} = s_{1,2} = -\alpha \pm \sqrt{\alpha^2 - \omega_0^2}, \tag{5.3}$$

where $\alpha = \frac{R}{2L}$ and $\omega_0 = \frac{1}{\sqrt{LC}}$.

The circuit elements comprising the RLC coupling circuit, i.e. R, L and C, determine the time constants $\tau_{1,2}$ in (5.3). These circuit elements, therefore, impact significantly on the time constants τ_1 and τ_2 associated with the exponential functions comprising the impulse waveforms contained in the PRIS perturbation current, $i_p(t)$. Depending on whether $\omega_0^2 < \alpha^2$, $\omega_0^2 > \alpha^2$, or $\omega_0^2 = \alpha^2$, the circuit shown in Figure 5.4 exhibits the following overdamped, underdamped or critically damped solutions for $i_p(t)$:

$$i_p(t) = K_1 e^{s_1 t} + K_2 e^{s_2 t} \text{ (Overdamped)}, \tag{5.4}$$

$$i_p(t) = K_3 e^{-\alpha t} \cos \omega_0 t + K_4 e^{-\alpha t} \sin \omega_0 t \text{ (underdamped)} \tag{5.5}$$

and

$$i_p(t) = K_5 t e^{-\alpha t} + K_6 e^{-\alpha t} \text{ (critically damped)}, \tag{5.6}$$

where K_1 to K_6 denote constants defined in terms of the circuit parameters.

Figure 5.7 shows simulated examples of overdamped, critically damped and underdamped waveforms for $i_p(t)$. In the case of an underdamped waveform, the PRIS impulses oscillate and pass below zero, which causes undershoots of opposite polarity. Increased damping by increasing the value of R reduces these oscillations but also decreases the peak values of the impulses. The PRIS proposed in this research has the characteristics of an overdamped waveshape. Excessive damping reduces the maximum amplitude of the current impulse signal, which in turn reduces the associated voltage perturbation. The circuit should, ideally, be designed such that impulse current waveform $i_p(t)$ is close to critically damped. This yields optimised values for

the passive elements, especially in the sense that R is sized such that the power the loss associated with the circuit is minimised. By appropriately sizing the three series-connected passive elements in the circuit, an impulse signal with appropriate values of τ_1 and τ_2 can be generated.

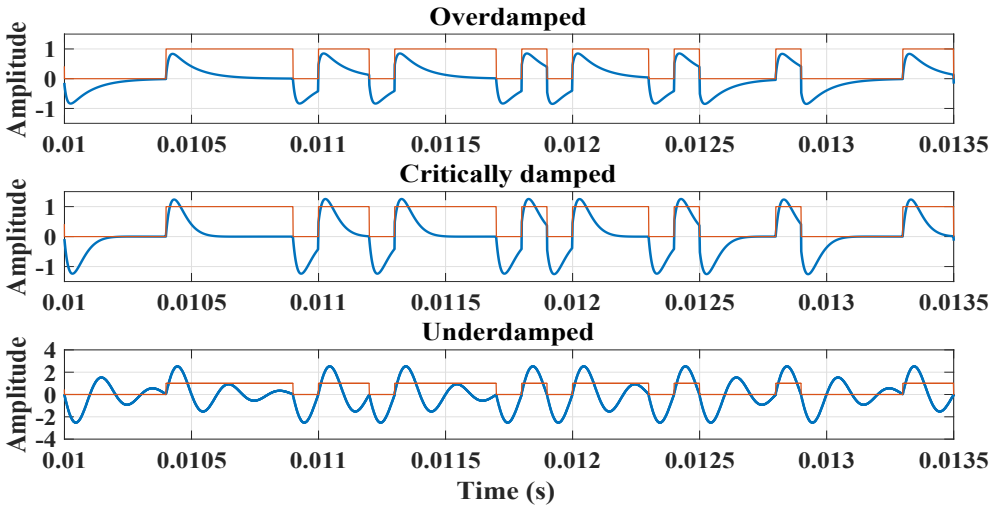

Figure 5.7: Simulated overdamped, critically damped and underdamped current waveforms for the the circuit topology shown in Figure 5.2.

Depending on the damping scenario that applies, the time-domain expression associated with $i_p(t)$ can be derived from the expressions given by (5.4) to (5.6). For the overdamped case, $i_p(t)$ is derived as follows:

In terms of the roots of the denominator defined by (5.3), (5.2) can be expressed as

$$I_p(s) = \frac{\frac{V_{dc}-V_0}{L}}{(s+\frac{1}{\tau_1})(s+\frac{1}{\tau_2})} + \frac{sI_0}{(s+\frac{1}{\tau_1})(s+\frac{1}{\tau_2})}. \tag{5.7}$$

The inverse laplace transform of (5.7) is be obtained as

$$i_p(t) = \frac{(V_{dc}-V_0)(e^{-t/\tau_2}-e^{-t/\tau_1})}{L(\frac{1}{\tau_1}-\frac{1}{\tau_2})} + \frac{\frac{I_0 e^{-t/\tau_1}}{\tau_1}}{(\frac{1}{\tau_1}-\frac{1}{\tau_2})} - \frac{\frac{I_0 e^{-t/\tau_2}}{\tau_2}}{(\frac{1}{\tau_1}-\frac{1}{\tau_2})}. \tag{5.8}$$

Equation (5.8) can be rearranged to yield

$$i_p(t) = \frac{\left[e^{-t/\tau_1}(V_0 - V_{dc} + \frac{I_0 L}{\tau_1}) - e^{-t/\tau_2}(V_0 - V_{dc} + \frac{I_0 L}{\tau_2})\right]\tau_1\tau_2}{L(\tau_2-\tau_1)}. \tag{5.9}$$

Similarly, the time domain expression of a negative impulse waveform can be expressed as,

$$i_p(t) = -\frac{\left[e^{-t/\tau_1}(V_0 - V_{dc} + \frac{I_0 L}{\tau_1}) - e^{-t/\tau_2}(V_0 - V_{dc} + \frac{I_0 L}{\tau_2})\right]\tau_1\tau_2}{L(\tau_2-\tau_1)}. \tag{5.10}$$

A bipolar PRIS is generated through repetition of several PRBS switching intervals. In this case, a series of chopped positive and negative impulse are created. A bipolar PRIS over one PRBS period can thus be expressed as

$$i^{B}_{pris}(t) = \sum_{i=0,2,4\ldots}^{((N+1)/2)-1} \frac{\left[e^{-t/\tau_1}(V_0 - V_{dc} + \frac{I_0 L}{\tau_1}) - e^{-t/\tau_2}(V_0 - V_{dc} + \frac{I_0 L}{\tau_2})\right]\tau_1\tau_2}{L(\tau_2 - \tau_1)} \times \Big[u(t - t_i) - u(t - t_{i+1})\Big]$$

$$- \sum_{i=1,3,5\ldots}^{((N+1)/2)} \frac{\left[e^{-t/\tau_1}(V_0 - V_{dc} + \frac{I_0 L}{\tau_1}) - e^{-t/\tau_2}(V_0 - V_{dc} + \frac{I_0 L}{\tau_2})\right]\tau_1\tau_2}{L(\tau_2 - \tau_1)} \times \Big[u(t - t_i) - u(t - t_{i+1})\Big]. \tag{5.11}$$

where $u(t - t_i) - u(t - t_{i+1})$ represents the random PRBS switching intervals of the switches.

The equation shown in 5.9 represents a positive overdamped impulse waveform, such as the one illustrated in Figure 3.1. This equation shows that in practice, the impulse waveform will be influenced by the initial state of the capacitor and inductor after every switching cycle. For instance, V_0, like the DC voltage V_{dc}, influences the maximum amplitude level of the impulse waveform. I_0, on the other hand, has an influence on the starting point of the impulse waveform. Since the switching is performed pseudo-randomly using the PRBS , the values of V_0 and I_0 will subsequently be pseudo-random. Therefore, although the shape of the practical PRIS waveform is similar to that of the ideal case presented in Figures 3.5 and 3.6, the consecutive chopped impulses in a practical PRIS waveform will have subtle differences in amplitude level and the point where each impulse starts.

The time constants for an overdamped condition, which is the case proposed for parameter estimation in this work, can be expressed in terms of the series RLC elements. This yields the relationships

$$\tau_1 = \frac{1}{s_1} = \frac{1}{|\, -\frac{R}{2L} - \sqrt{(\frac{R}{2L})^2 - \frac{1}{\sqrt{LC}}}\,|} \tag{5.12}$$

and

$$\tau_2 = \frac{1}{s_2} = \frac{1}{|\, -\frac{R}{2L} + \sqrt{(\frac{R}{2L})^2 - \frac{1}{\sqrt{LC}}}\,|}. \tag{5.13}$$

5.2.2.2 Impedance of the series RLC circuit

The impedance of the series RLC circuit is given by the relationship

$$Z(\omega) = R + j\omega L + \frac{1}{j\omega C}. \tag{5.14}$$

Equation (5.14) can be rearranged to yield

$$Z(\omega) = \frac{j\omega RC - \omega^2 LC + 1}{j\omega C}. \tag{5.15}$$

The magnitude of the series RLC impedance, $|Z|$, is given by the expression

$$|Z(\omega)| = \frac{\sqrt{[(1-\omega^2 LC)^2 + (\omega RC)^2]}}{\omega C}. \tag{5.16}$$

Equation (5.16) can be used to optimise the values of the reactive elements of the series RLC circuit to achieve the desired attenuation factor in a given frequency band. This is illustrated in Figure 5.8 where, using (5.16), the frequency responses of $|Z(\omega)|$ for various ratios of L/C are compared. The results are presented for the same value of R, i.e. $R = 50\Omega$, for all cases and L fixed at 50μH. The straight line represents the response of the topology shown in Figure 2.6, where a purely resistive coupling circuit applies. In this case, in order to increase the attenuation of the AC component induced by the Thevenin equivalent AC supply source, the series resistance must be increased, which will result in increased power losses in the circuit.

The magnitude response of the impedance of the series RLC circuit exhibits a bandpass characteristic, with high impedance in the lower and upper frequency ranges. By varying the ratio of the reactive components, the resonant frequency and magnitude response of the series impedance can be controlled. The resonant frequency can be derived using the expression

$$f_r = \frac{1}{2\pi\sqrt{LC}} \tag{5.17}$$

The resonant frequency of the RLC network shifts to the right as the $\frac{L}{C}$ is increased. This affects the spectral shape of the PRIS perturbation current $i_p(t)$ in the low-frequency region and influences the attenuation of the AC component in the perturbation current. Overall, these observations support the conclusions derived in the spectral analysis of the PRIS signal discussed in section 4.3.3, especially in the sense that the spectral content of the signal can be focussed by reducing excitation in the lower and upper frequency regions.

The results presented in Figure 5.9 illustrate the relationship between the magnitude of the impedance of the series RLC circuit at 50 Hz, i.e. $|Z(50Hz)|$, and the PRIS time constants for the case where $\frac{L}{C} = 10$. These curves illustrate that the impedance increases with decreasing values of τ_1 and decreasing values of τ_2. This is associated with increased attenuation of the sinusoidal component induced by the AC voltage source in the PRIS current signal $i_p(t)$. Curves such as shown in Figure 5.8 and 5.9 can be used in the design of the PRIS source, especially with reference to the following:

- Derive optimal values for time constants τ_1 and τ_2, such that adequate excitation energy is achieved in the desired frequency band.

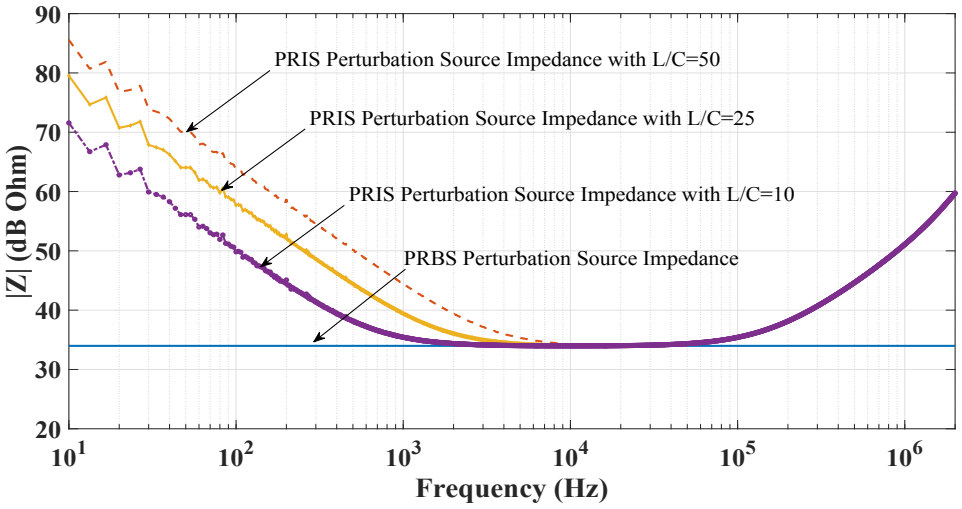

Figure 5.8: Frequency responses of the magnitude of the impedance of the series circuit, $|Z(\omega)|$, as a function of the ratio $\frac{L}{C}$, for R=50Ω and L=50μH.

- Ensure sufficient attenuation of the AC component in the perturbation current, such that the power ratings of the PRBS source components are optimised and the power losses are minimised.

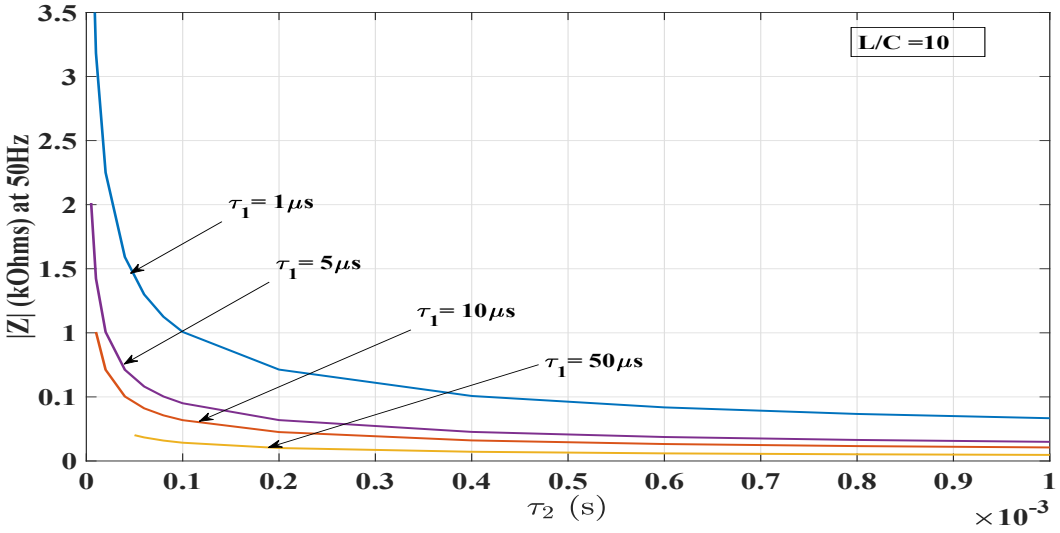

Figure 5.9: Relationships between the magnitude of the impedance of the series RLC circuit at 50Hz, $|Z(50Hz)|$, and time constants τ_1 and τ_2.

5.2.3 Effects of the target system on the PRIS perturbation signal

5.2.3.1 Overview

It can be expected in practice that the systems targeted in wideband system identification and parameter estimation experiments exhibit complex frequency-dependent input impedance characteristics. The input impedance of the system under test can have considerable influence on the time- and frequency-domain characteristics of the resultant perturbation current. Different scenarios are therefore investigated with the view to gain insight into these influences.

5.2.3.2 PRIS perturbation current characteristics for a capacitive target system impedance

Figure 5.10 shows an equivalent circuit representation for the case where the input impedance of the target system is capacitive. Circuit elements R_s, L_s and C_s represent the series RLC components of the PRIS source, while C_T denotes the input capacitance of the target system. The effects of a capacitive target system on the PRIS perturbation current are investigated by simulations performed for different ratios of the target capacitance C_T to the PRIS source capacitance C_s. The equivalent capacitance, C_{eq}, of the circuit shown in Figure 5.10 is given by the relationship

$$C_{eq} = \frac{C_s}{\frac{C_s}{C_T} + 1}. \tag{5.18}$$

Equation (5.18) shows that $C_{eq} \rightarrow C_s$ as $C_T \rightarrow \infty$, while $C_{eq} \rightarrow 0$ as $C_T \rightarrow 0$. In general, for very low values of C_T, the equivalent capacitance C_{eq} is also low, which gives rise to a high capacitive reactance for the combination.

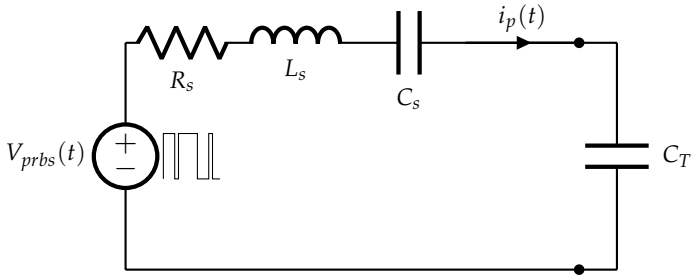

Figure 5.10: Circuit topology of the PRIS source with a capacitive target system input impedance.

Figure 5.11 and Figure 5.12 show simulated time-and frequency-domain responses respectively for varying values of the ratio of the capacitance of the target system, C_T, to the capacitance of the PRIS source, C_s. The responses for a pure resistive target is also shown for comparison. The results show that, as C_T decreases relative to C_s, the magnitude of the perturbation

current decreases, while the time-domain waveform assumes an underdamped response. The spectral energy in the main lobe also decreases. As the value of C_T increases, the value of C_{eq} increases to assume the value of C_s. The results presented in Figure 5.11 and Figure 5.12 show, furthermore, that the time-and frequency-domain responses do not change significantly for $\frac{C_T}{C_s} \geq 1 \times 10^2$.

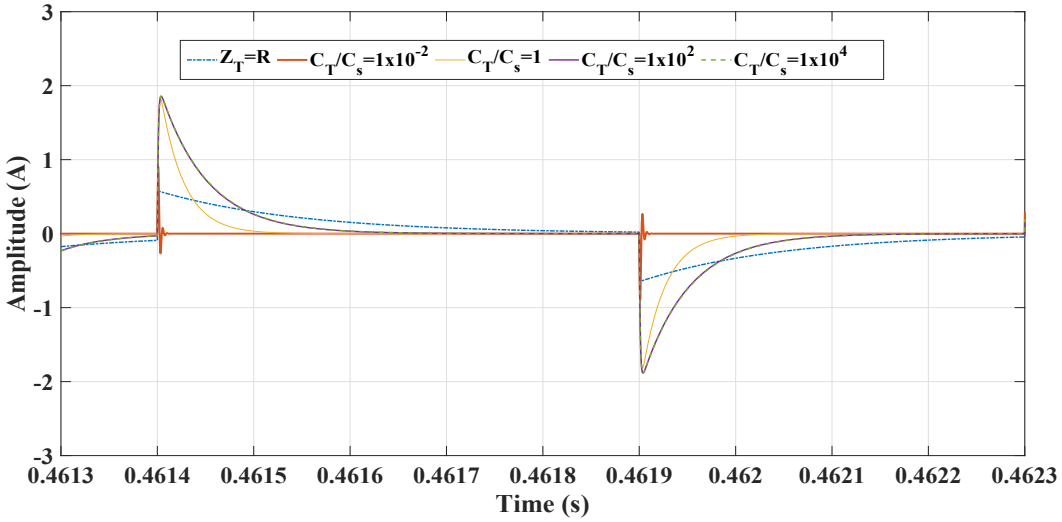

Figure 5.11: Time-domain responses of the PRIS perturbation current as a function of ratio of the target system capacitance C_T to the PRIS source capacitance C_s.

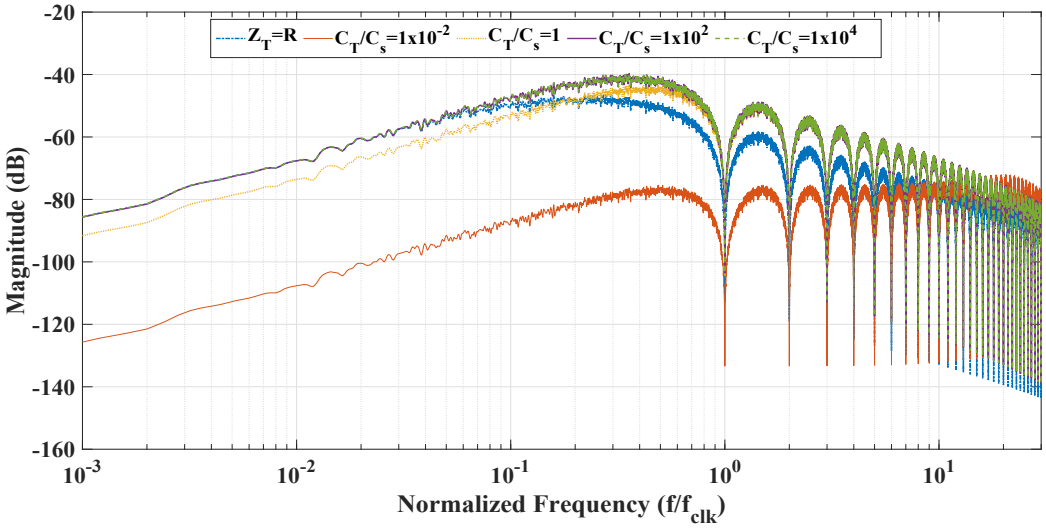

Figure 5.12: Frequency-domain responses of the PRIS perturbation current as a function of ratio of the target system capacitance C_T to the PRIS source capacitance C_s.

5.2.3.3 PRIS perturbation current characteristics for an inductive target system impedance

Figure 5.13 shows an equivalent circuit representation for the case where the input impedance of the target system is inductive. Circuit elements R_s, L_s and C_s represent the series RLC components of the PRIS source, while L_T denotes the input inductance of the target system. The effects of an inductive target system on the PRIS perturbation current are investigated by simulations performed for different ratios of the target inductance L_T to the PRIS source inductance L_s. The equivalent inductance, L_{eq}, of the circuit shown in Figure 5.13 is given by the relationship

$$L_{eq} = L_T + L_s. \tag{5.19}$$

Equation (5.19) shows that $L_{eq} \to L_T$ as $L_T \to \infty$, while $L_{eq} \to L_s$ as $L_T \to 0$. In general, for very high values of L_T, the equivalent inductance L_{eq} is also high, which gives rise to a high inductive reactance for the combination.

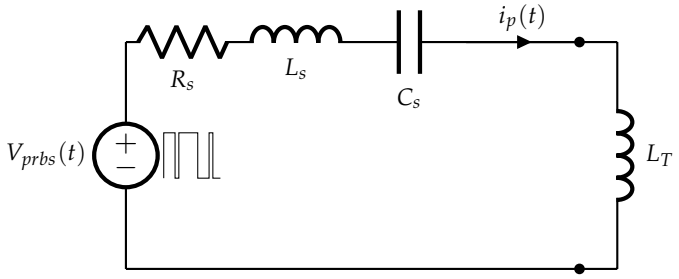

Figure 5.13: Circuit topology of the PRIS source with an inductive target system input impedance.

Figure 5.14 and Figure 5.15 show simulated time-and frequency-domain responses respectively for varying values of the ratio of the inductance of the target system, L_T, to the inductance of the PRIS source, L_s. The responses for a pure resistive target is also shown for comparison. The results show that, as L_T increases relative to L_s, the magnitude of the perturbation current decreases, while the time-domain waveform assumes an underdamped response. The spectral energy in the main lobe also decreases. As the value of L_T decreases, the value of L_{eq} decreases to assume the value of L_s. The results presented in Figure 5.11 and Figure 5.12 show, furthermore, that the time-and frequency-domain responses do not change significantly for $\frac{L_T}{L_s} \leq 1 \times 10^2$.

Unlike in the case of a capacitive target system, the inductive system has a significant effect on the location and damping of the series resonant point introduced in (5.17). A high value of L_T shifts this resonant frequency towards the lower frequency region and decreases the

damping ratio. While this phenomenon may be detrimental in some applications, it can be an advantage in other applications.

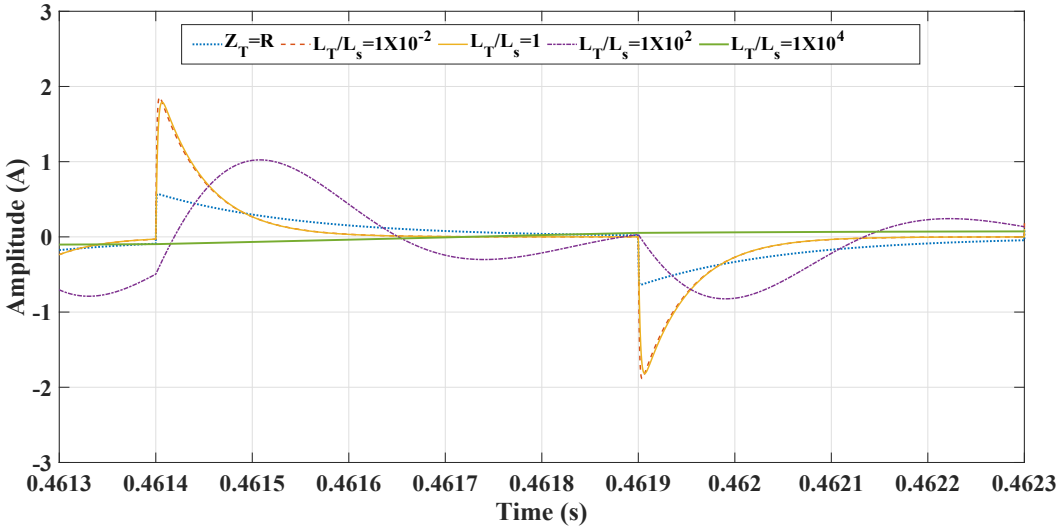

Figure 5.14: Time-domain responses of the PRIS perturbation current as a function of ratio of the target system inductance L_T to the PRIS source inductance L_s.

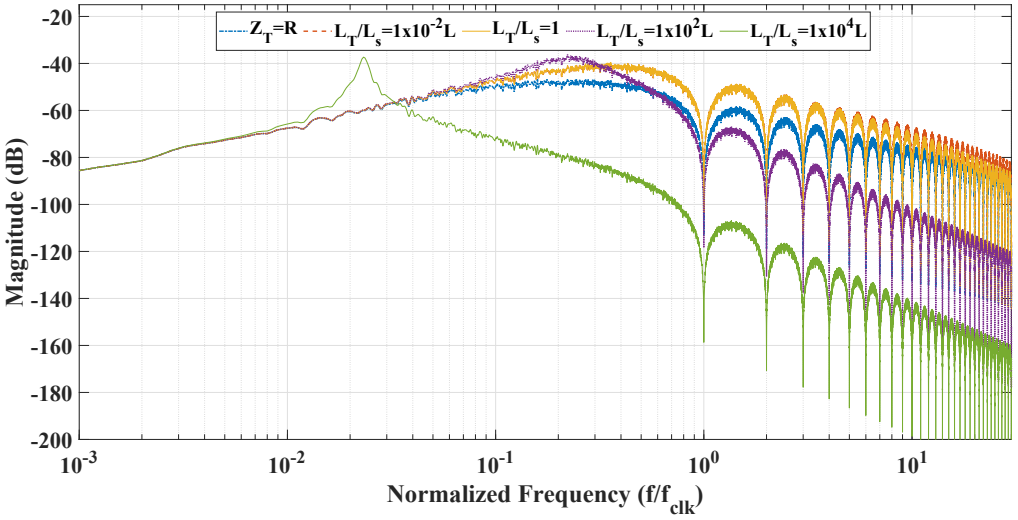

Figure 5.15: Frequency-domain responses of the PRIS perturbation current as a function of ratio of the target system inductance L_T to the PRIS source inductance L_s.

5.2.3.4 PRIS perturbation current characteristics for a complex target system impedance

Practical target systems, such as an AC network or transformer targeted under *in situ* operating conditions, typically exhibit complex input impedance frequency responses, that vary with frequency through resistive, inductive and capacitive domains. Complex target systems

may reflect successive combinations of these scenarios across the frequency range of interest. The behaviour of the PRIS topology in these regions can be interpreted with reference to the scenarios presented in 5.2.3.2 and 5.2.3.3.

5.2.4 Comparison of power loss between the PRBS voltage source and a PRIS source in an *in situ* application

In the context of high power, high voltage *in situ* applications, it is of interest to compare the power losses associated with a PRBS voltage source connected through a series resistive element versus a series RLC circuit. Figure 5.16 compares the instantaneous power losses in the series resistor for the PRBS voltage source topology shown in Figure 2.6 and the PRIS source topology shown in Figure 5.1, for the same RLC values used for the simulation results presented in Figure 2.7 and 5.2. The instantaneous power waveforms reflect one cycle of the sinusoidal source supply voltage. The results show, that for equal values of V_{prbs} and R, the source topology with resistive coupling presents significantly higher losses compared to the PRIS perturbation source topology. The ratio of the average power loss in resistor R in the PRIS source to that in the PRBS voltage source, calculated over one PRBS period for this simulation, is approximately1:35. This suggests that the PRIS can be generated using a compact and efficient design with highly reduced average power losses, compared to conventional sources such as the PRBS current source and a PRBS voltage source connected through a series resistor.

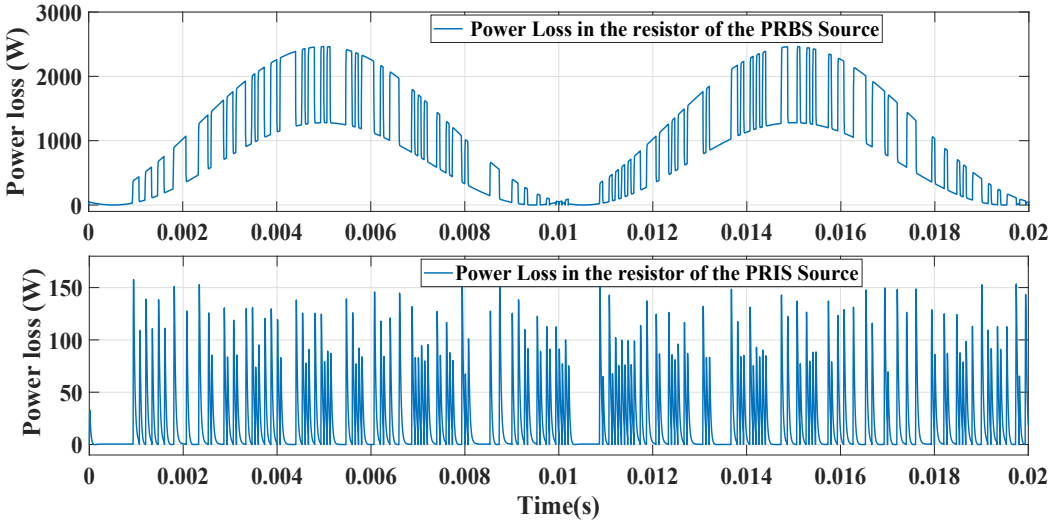

Figure 5.16: Instantaneous power loss in resistor R for (a) the PRBS perturbation source topology shown in Figure 2.6, and (b) the PRIS perturbation source topology shown in Figure 5.1.

5.3 Design considerations for a practical PRIS source

5.3.1 Introduction

The PRIS source topology shown in Figure 5.1 consists of a bipolar PRBS voltage source and a series RLC circuit. The PRBS voltage source implements a classical active H-bridge to switch the polarity of a DC source, where the gate signals are controlled by a unipolar PRBS waveform, as shown in Figure 5.18. The H-bridge features four semiconductor switches, i.e S_1 to S_4, and the two switches in each leg of the bridge switch complementarily to each other, such that when one is in the "on" state, the other one is in the "off" state. The operation of this PRIS source exhibits two switching intervals. In the first interval, switches S_1 and S_4 conduct, while S_3 and S_2 are open. In the second interval, switches S_3 and S_2 conduct, while switches S_1 and S_4 are open. Switches S_1 and S_4 are activated on the positive transitions of the PRBS signal, while switches S_2 and S_3 are activated on the negative transitions. Inverting logic gates are implemented on switches S_2 and S_3 to invert the unipolar PRBS signal applied to these switches. The waveforms shown in Figure 5.18 illustrates the operation of the switching sequence.

The switches operate in off/on mode, which reduces losses and thereby enhances the scope of application for high power/high voltage applications. The lengths of each of the switching intervals are pseudo-random, as it is determined by the PRBS run. The shortest switching interval will be equal to the PRBS clock period, T_{clk}, while the longest interval will be equal to nT_{clk}, where n is the number of shift registers used in PRBS generation.

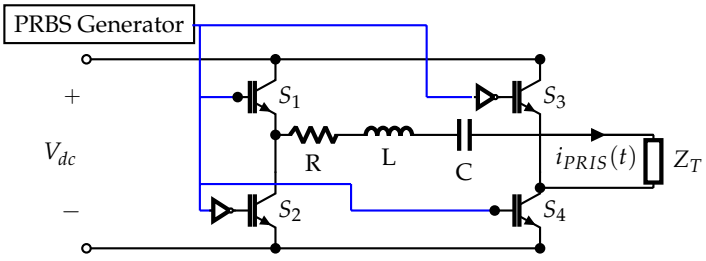

Figure 5.17: Configuration of the active H-bridge for generating the bipolar PRBS voltage signal.

5.3.2 Design of a programmable PRBS generator

Figure 5.19 shows a block diagram of the n-stage LFSR topology that is commonly used to generate a PRBS . The feedback paths are implemented through a modulo-two gate [13], and the order of the PRBS states depends on the feedback configuration. The number of shift registers, n, determines the length, N, of the PRBS , such that $N = 2^n - 1$. The stages of the LFSR are cross-connected and are simultaneously triggered by a clock pulse of length T_{clk}. When the

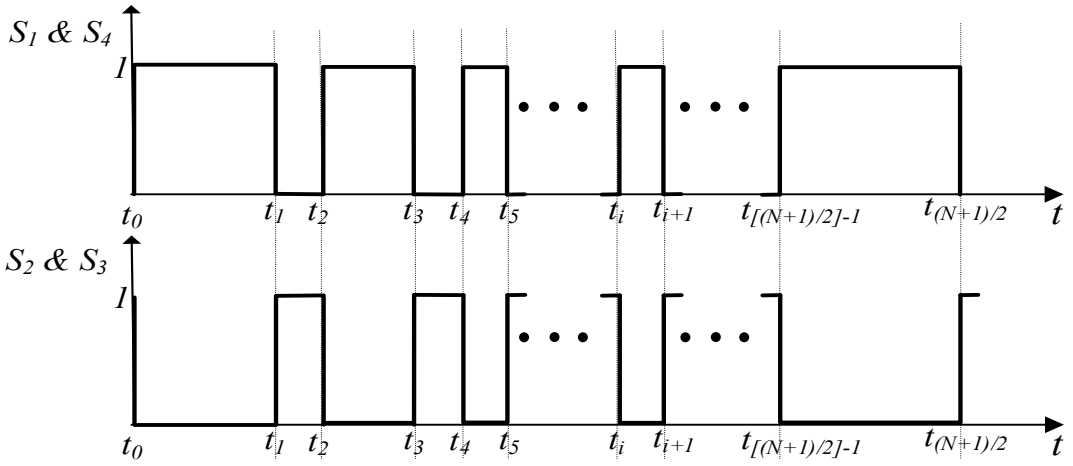

Figure 5.18: Switching sequence of the bipolar PRBS voltage source.

clock pulse is applied, the logic content of each LFSR stage are transferred to the next, and a new logic state is introduced to the input of the first stage through the feedback circuit. The contents of the LFSR, therefore, move in a cyclic manner and the output, which is normally taken from the final stage, forms a serial sequence of logic states. A scenario in which all the stages in the LFSR contain a logic 0 should be avoided. This is because the output of the exclusive OR (XOR) yields a logic 0 state, and the shift register would remain in this state, thereby generating an infinite zero sequence.

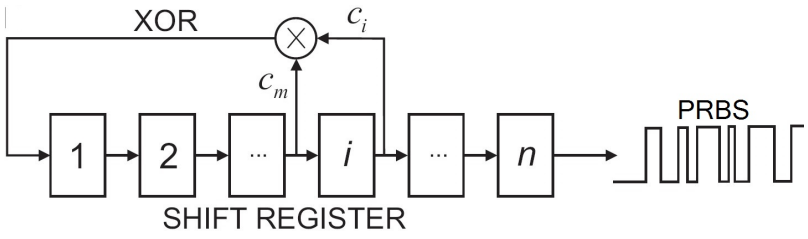

Figure 5.19: Generation of a PRBS using a linear feedback shift register topology.

An LFSR can mathematically be described in terms of a polynomial equation, from which the points of feedback connections can be determined. Table 5.1 summarises the polynomials and PRBS lengths for 4-stage PRBS (PRBS 4) to a 9-stage (PRBS 9) LFSR configurations [13], [54]. The input of the XOR gate for a 4-stage LSFR, for example, is the third and fourth stage of the LFSR, as illustrated in Figure 5.20.

A PRBS generator can be implemented in practice either through a hardware implementation or through a software implementation. Hardware implementations include the use of shift registers and flip-flops or a Field Programmable Gate Array (FPGA). Software implementations typically use a microcontroller or a development environment such as LabVIEW, by realising a

Table 5.1: LFSR polynomials for different PRBS lengths [13]

n	**Polynomial**	$N = 2^n - 1$	n	**Polynomial**	$N = 2^n - 1$
4	$X^4 + X^3 + 1$	15	5	$X^5 + X^3 + 1$	31
6	$X^6 + X^5 + 1$	63	7	$X^7 + X^6 + 1$	127
8	$X^8 + X^6 + X^5 + X^4 + 1$	255	9	$X^9 + X^5 + 1$	511

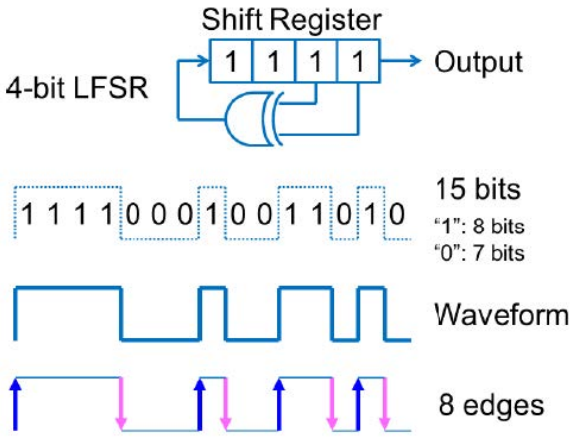

Figure 5.20: PRBS waveform generation with 4-stage LFSR [55].

Figure 5.21: Block diagram illustration of a PRBS source

virtual instrumentation design. Microcontrollers with high clock speeds are readily available, which allows for a PRBS generator with a high bandwidth to be realised. In order to ensure a PRIS source with a high degree of controllability, it is necessary to implement a programmable PRBS signal generator, where parameters such as the length of the PRBS shift register, n, and clock frequency, f_{clk}, can be defined by the user to suit a particular application.

In order to ensure the desired degree of controllability, a software implementation using a microcontroller is selected for the PRBS generator designed in this investigation. The system uses an ATmega328 microcontroller, with a clock speed of 16 MHz, which is sufficient for the frequency band considered in this work. Figure 5.21 shows an overview of the PRBS generator. A Graphical User Interface (GUI) is implemented on the host computer using the Python pro-

gramming language, where the control parameters of the LSFR are selected. These parameters include the number of shift registers n, clock frequency f_{clk} and length of the desired PRBS sequence.

The host computer communicates with the microcontroller via a Universal Serial Bus (USB). The LFSR is implemented on the microcontroller, using the C programming language. The binary polynomials are initialised as variables and XOR gates are implemented using the bitwise operators. A bitshifter() function is implemented to shift the PRBS bits to the right, thereby generating the PRBS sequence. The microcontroller generates two complementary PRBS signals, i.e. $PRBS$ and $\overline{PRBS}$, that are available at the digital output pins of the controller. These signals, with logic level one of 5 V, serve as the input signals to the gate driver circuits that control the switching of the H-bridge switches. The PRBS generator implemented using the above approach can generate PRBS signals from PRBS with n= 4 to 14, with a maximum clock frequency in excess of 500 kHz.

Figure 5.22 shows measured waveforms for the clock signal, $PRBS$ signal and $\overline{PRBS}$ signal for the system, where f_{clk} =10 kHz and n=4. The waveforms shown in Figure 5.22 represent two periods of a PRBS 4 waveform, where the total sequence length is given by $2 \times (\frac{2^n-1}{f_{clk}})$= 3 ms.

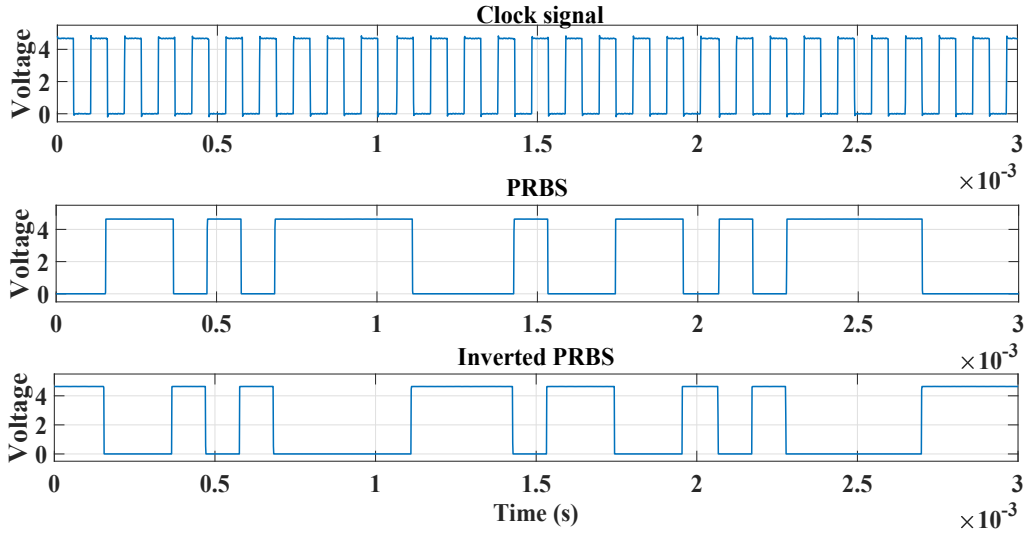

Figure 5.22: Measured clock signal, $PRBS$ signal and $\overline{PRBS}$ signal for f_{clk} =10 kHz and n=4 bits.

5.3.3 Design of the H-bridge

The voltage level of the DC input to the PRIS generator determines the dynamic range of the PRIS current impulses produced by the system. The DC voltage level used in an *in situ* system

identification experiment should be high enough to ensure a good SNR, but low enough to ensure that the target system is not disturbed too far from the normal operating condition. It is therefore desirable that the DC voltage can be adjusted to suit various applications. In the source topology implemented for this investigation, the DC input voltage, V_{dc}, is derived from a variable transformer, using a rectifier and smoothing filter, or from a variable DC power supply.

The H-bridge designed for the purposes of this investigation has a voltage rating of 1 kV, with a peak current rating of 20 A. Figure 5.23 shows the circuit implementation of the complete H-bridge circuit. The semiconductor switches are implemented using Insulated Gate Bipolar Transistors (IGBTs), due to their high voltage and current ratings. IGBTs, furthermore, have the advantage of a low on-state voltage, $V_{CE(sat)}$, even for devices with large voltage ratings. This reduces on-state power losses, especially in high voltage, high current applications. The switching elements are controlled by the complementary digital PRBS control signals, i.e. $PRBS$ and $\overline{PRBS}$. These signals are interfaced to the IGBT gate circuits via gate drivers, that translates the digital control signals to voltage and current levels that are suitable to drive the IGBT switches, and also provide galvanic isolation between the microcontroller and the power electronic circuit.

The chopped impulse waveform associated with the PRIS perturbation current shows that the switches interrupt the inductive perturbation current for short PRBS periods. This necessitates the implementation of appropriate snubber circuitry to prevent high voltage pulses during switching. Anti-parallel diodes are therefore implemented to protect the IGBTs from high reverse voltages. An RC snubber circuit is included in the circuit to suppress the overvoltages that may arise due to the parasitic inductance, L_p, associated with the connection between the DC voltage source and the H-bridge. The parameters of the RC snubber circuit are determined from an estimated value of the parasitic inductance. The instantaneous energy stored in this inductor depends on the instantaneous magnitude of the impulse current, which varies randomly from switching interval to switching interval. This energy should be transferred to the snubber circuit during the switching transitions. The snubber capacitor can be approximated by equating the energy stored in the parasitic inductor to that stored in the snubber capacitor, which yields the expression, $C_s = \frac{L_p I_s^2}{V_{dc}^2}$, where I_s denotes the peak value of the switching current. The snubber resistor is chosen such that $R_s = \frac{V_{dc}}{I_s}$. The snubber resistor can be fine-tuned further to reduce ringing if the value of R is found to be insufficient.

The Silicon Labs SI8233 isolated driver is selected due to its low propagation delay at a maximum of 60ns and compact nature [56]. The power switches used are the IXGH24N170 IGBTs which are rated to block voltages up to 1700V and conduct a continuous current of

up to 50A [57]. The freewheeling diodes are implemented using the 30 A, 1200 V hyperfast RHRP30120 diodes [58].

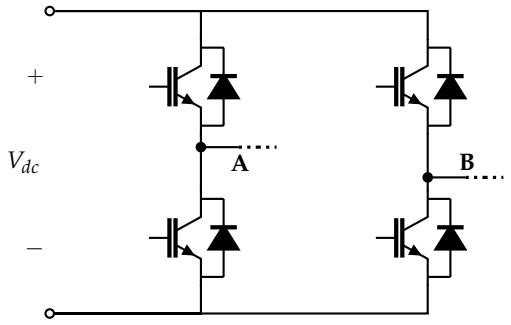

Figure 5.23: Circuit diagram of the H-bridge implementation.

Figure 5.24 shows the measured voltage waveform produced by the practical H-bridge configuration for a DC input voltage of 48 V, and using a PRBS 4 signal with a clock frequency of 10 kHz.

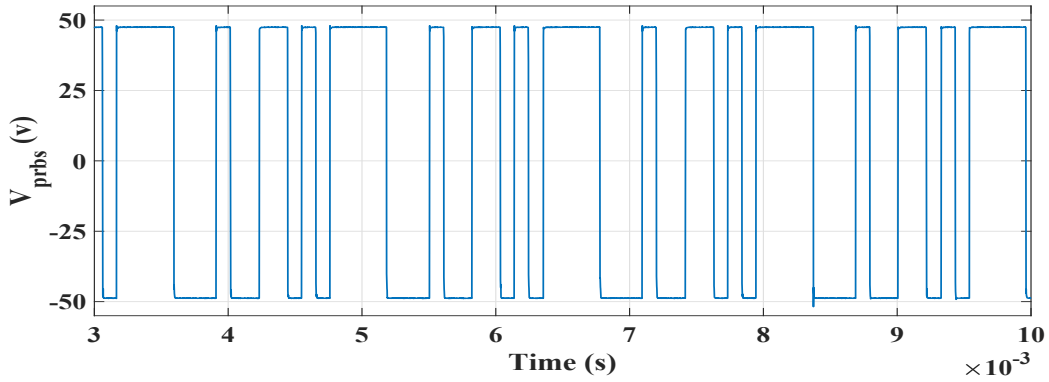

Figure 5.24: Measured voltage waveform produced by the practical H-bridge configuration for a DC input voltage of 48 V, and using a PRBS 4 signal at a clock frequency of 10 kHz.

5.3.4 Optimization of the RLC circuit

The design of an optimum PRIS source for a system identification experiment is highly dependent on the characteristics of the system targeted in the experiment. In this context, the design of the series RLC circuit should take cognisance of the following considerations:

- The analysis presented in chapters 3 and 4 show that time constants τ_1 and τ_2 must be selected such that an optimal distribution of spectral energy for the system targeted in the investigation is realised. The results presented in section 5.2.2 detail the relationships

between these time constants and the time- and frequency-domain properties of the resultant PRIS perturbation waveform for the short-circuited PRIS source. In practice, the considerations highlighted in section 5.2.3 with reference to the effects of the target system, must also be considered.

- In high power, high voltage *in situ* applications, the AC current component induced by the Thevenin AC supply source in the perturbation current must be sufficiently attenuated in order to reduce the current and power ratings of the switching elements. This can be achieved by considering the insights presented in section 5.2.2.2.

Equations (5.12), and (5.13) can be used iteratively to determine appropriate values for R, L and C, by assigning a value to one of the elements and then invoking appropriate practical constraints, including the following:

- To avoid front chopping of the PRIS impulses, which would result in low dynamic range, the design should ensure that τ_1 is small compared to T_{clk}.
- τ_2 should be large compared to the longest PRBS run, nT_{clk}, such that the PRIS impulses are not allowed to decay rapidly on the falling edge.
- From equation (5.16), the impedance value at the fundamental frequency should be high enough to provide sufficient attenuation of the sinusoidal component in the perturbation current by an *in situ* target system.

The choice of these two time constants will influence the PRIS spectrum, as is illustrated in Figures 4.6 and 4.7. To ensure suitable damping of the PRIS waveform, the RLC circuit can further be optimised, such that the damping ratio $\zeta \leq \frac{R}{2}\sqrt{\frac{C}{L}}$.

5.4 Conclusion

A system topology that can be used for *in situ* system identification using the proposed PRIS signal is described and analyzed. The design considerations for a practical PRIS source are discussed. The design of the PRIS source involves designing a programmable PRBS generator, H-bridge circuit design and sizing of the RLC network. The PRBS generator should be designed such that the PRBS clock frequency and length can be controlled as this has an influence on the frequency characteristics of the PRIS current. The series RLC network, which influences the value of the PRIS time constants and hence the shape of the waveform, should be optimised to ensure that perturbation energy is sufficient across the desired frequency band.

The advantages of the PRIS source circuit topology for high power, high voltage *in situ* perturbation applications, from a practical circuit perspective, include:

- The power electronic switches in the PRIS source operate in an on/off mode, thereby reducing power losses.
- The PRIS source can make use of the reactive elements, particularly the series capacitor, to attenuate the fundamental frequency current component induced by the AC system under test. This translates into reduced power losses and lower power ratings of the power electronic switches used in the circuit.
- The PRIS time constants are functions of the reactive elements in the PRIS source circuit. The time constants can be used to control the spectral properties of the PRIS signal. It is, therefore, possible to practically control the frequency properties of the PRIS by varying the values of the reactive elements to achieve more perturbation energy at the frequency band of interest.

The interaction of the PRIS source with the target system is investigated. It is shown that the system under test can have considerable influence on the time-and frequency-domain characteristics of the perturbation current. The design of the PRIS source should, therefore, be guided by the nature of the characteristics of the target system.

CHAPTER 6

Application of the Pseudo-Random Binary Impulse Sequence to *In Situ* Identification of Grid Impedance

6.1 Introduction

The PRIS perturbation signal developed in this research has good potential for *in situ* system identification and parameter estimation applications. To verify the proposed signal and the associated source topology for a practical case study, the PRIS signal is applied to determine the grid impedance characteristics of a 50 Hz supply network for the frequency range up to the 50th harmonic. A novel experimental procedure is proposed to perform *in situ* frequency response measurements of the grid impedance in the presence of the stochastic variations of the system voltage and frequency. The measured frequency responses are used to estimate parameters for an approximate lumped parameter circuit model of the grid topology.

6.2 Overview of system identification and parameter estimation principles

System identification encompasses the field of mathematical modelling of systems using measured input and output signals [1]. System identification, parameter estimation and digital signal processing techniques have been applied extensively in the field of energy systems, including the modelling and identification of power system impedance and equipment such as motors, transformers, generators, excitation systems and power converters [11]-[12], [20]-[45], [48]. These models are used in a range of power system studies, including stability studies, machine control, spectral analysis, fault detection, pattern recognition and linear prediction. The success of these studies is, however, dependent on accuracies the associated model structures and parameters.

The identification process typically consists of the following series of steps [34], [59]:

1. **Getting information about the target system**

To build a model for a target system it is necessary to obtain information about the system. This information can be obtained from the normal operation of the system, through experimental measurements, or a combination of both. Experimental measurements typically use a dedicated perturbation source to excite the target system. An optimal excitation is selected by considering cost, measurement time and power consumption, as well as the accuracy, repeatability and reliability of the results. The signals to be measured and the associated measurement procedures also require careful consideration. These choices are made within the constraints of the experimental design to obtain informative data.

2. **Choosing the model structure to represent the target system** A system model can be broadly defined as an assumed relationship between observed signals [59]. The models that are of interest for the dynamic systems can be classified into mental models, graphical models, software models and mathematical models [1]. A mathematical modelling approach is adopted for the case study considered in this investigation. Mathematical models also referred to as analytical models, describe the relationships between system variables in terms of mathematical expressions, such as difference or differential equations.

   An analytical approach is adopted and the system is described using the laws of physics. These models are well suited to the analysis, prediction, and design of dynamic systems. Mathematical models are typically developed by defining a model structure, i.e. the grey-box modelling approach, or by system identification, i.e. the black-box modelling approach, or a combination of both. In the grey-box modelling approach, the system is broken into subsystems, of which the properties are known from previous experience or earlier empirical work. These subsystems are then joined mathematically to obtain the complete system model. The black box approach, however, implements an experimental approach where input and output signals are recorded. A model is then fitted to the recorded data by assigning suitable parameter values [1].

3. **Estimating unknown model parameters**

   Unknown model parameters, such as the coefficients in the differential equation or circuit parameters, are estimated. Figure 6.1 shows a block diagram that illustrates the parameter estimation process. A parametric model is initialised with values derived from datasheets and *a priori* knowledge of the system. The measured output of the system, y, and the simulated output of the model, $\bar{y}$, are compared and a cost function, ϵ is derived as a measure of the difference between the measured and simulated responses. The model

parameters, θ, are then optimised by minimising the cost function, using an appropriate parameter estimation algorithm [1].

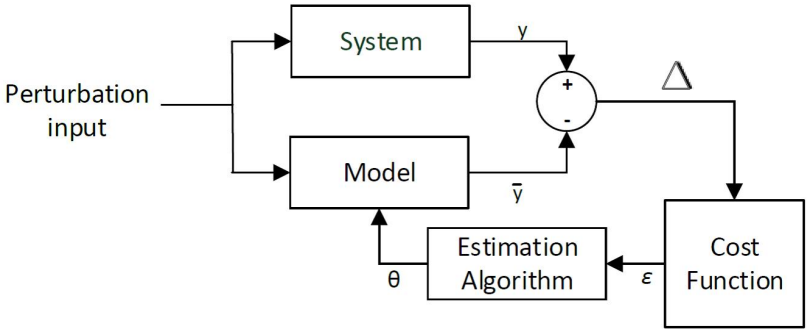

Figure 6.1: Parameter Estimation block diagram.[1]

4. **Validating the model**

   Model validation aims to assess how well the estimated model reproduces measured data. The process is iterative in the sense that inadequate models are rejected and the identification process is repeated until an acceptable solution is achieved. A model may be inadequate due to the following [59]:

   - An insufficient model structure choice.
   - Uninformative data. The system may not have been perturbed persistently for estimation purposes.
   - Insufficient identification criterion, i.e. optimization algorithm, chosen for fitting.

6.3 Grid impedance identification

6.3.1 Overview

There are numerous applications where the wideband modelling of grid impedance is of interest for the modern power system, including the following [3], [21], [22], [36], [60]:

- Harmonic filter design
- Harmonic penetration studies
- Transient analysis

- Design of protection systems
- Verification of grid compliance, especially with reference to harmonic distortion limits
- Prediction of power system resonance

The hierarchy depicted in Figure 6.2 shows that the system identification methods that are typically applied for characterising grid impedance can be broadly categorised into passive and active methods, based on the influence that they have on the system under test. Passive methods [20], [25], [61] are non-invasive and rely on existing network components to generate the perturbation signal. Wideband perturbation is, for instance, induced during switching operations. Passive methods are cost-effective and easy to implement, as no external perturbation sources are necessary. The grid impedance can, however, only be determined for the frequencies that are present in the waveform of the system voltage. Passive methods, therefore, have a limited frequency resolution and range. The perturbation is not controllable, and the occurrence and amplitude of the perturbation signal cannot be guaranteed. This may result in a low SNR [11]. Active methods, however, are invasive in the sense that an external source is used to inject a perturbation signal [3], [11], [21], [24], [26]. Although they are more costly compared to passive methods, active methods are becoming more popular. This is because active perturbation signals have some degree of controllability. The amplitude, for example, can be adjusted to improve the SNR, thereby improving the accuracy of the system identification experiment.

Active methods can be categorised further into transient and steady-state methods, depending on the nature of the perturbation signal. Transient methods, such as proposed by Cespendes *et al.* [23], involve the application of an impulse perturbation, while Girgis and McManis [36] proposed the use of a transient excitation is introduced by switching a capacitor. Sumner *et al.* [21] measured grid impedance using a transient perturbation by injecting a short current spike at the POC. Transient perturbation methods require the use of a high-speed data acquisition system. In steady-state methods, a periodic perturbation such as sine wave is applied and the measurements are repeated at different frequencies. Steady-state methods based on wideband perturbations, such as random sequences, have also been reported [12]. Both the transient and steady-state methods employ Fourier analysis to obtain the frequency components in the injected signal, which is usually a current signal, and the resulting voltage response.

The bipolar PRIS perturbation signal proposed in this research falls in the category of an active, steady-state grid impedance identification methodology.

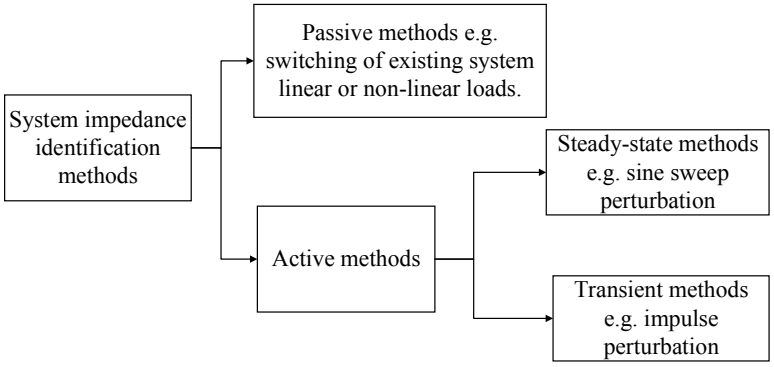

Figure 6.2: Hierarchy of grid impedance identification methods.

6.3.2 *In situ* grid impedance frequency response measurements

6.3.2.1 Measurement arrangement

Figure 6.3 shows the circuit topology of the test arrangement implemented for *in situ* identification of the frequency response of the Thevenin equivalent impedance, Z_{Th}, of a single-phase network. The PRIS perturbation source is connected at the PCC.

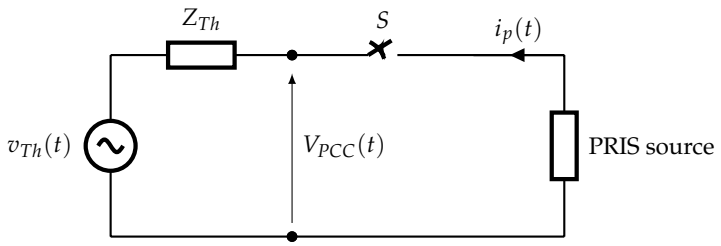

Figure 6.3: Impedance measurement of grid impedance using PRIS perturbation.

The impedance measurement method proposed in this research is conducted in two stages, which are controlled by the switch, S, that allows for the perturbation signal to be connected to the network. The measurement is initiated with S in an open position. In this state, the pre-excitation open circuit voltage waveform associated with $v_{Th}(t)$ is recorded at the PCC. After several cycles, S is closed to apply the PRIS perturbation source. During this state, the perturbation current, $i_p(t)$, induces a perturbation signal on the voltage waveform at the PCC, $v_{PCC}(t)$, due to the voltage drop induced across Z_{Th}. The post-excitation data, i.e. the perturbed voltage $v_p(t)$ and perturbation current $i_p(t)$, are recorded. This results in two sets of recorded data i.e. the pre-excitation and post-excitation data. The voltage drop $\Delta v(t)$ across the Thevenin equivalent grid impedance, Z_{Th}, is defined by the relationship

$$\Delta v(t) = v_{Th}(t) - v_p(t). \tag{6.1}$$

In practice, the Thevenin equivalent voltage source, $v_{Th}(t)$, is typically represented by a sinusoidal AC grid supply voltage waveform, with some degree of harmonic distortion caused by the interaction of harmonic currents drawn by the nonlinear loads with the supply impedance. This gives rise to the following mathematical formulation for $v_{Th}(t)$:

$$v_{Th}(t) = \sum_{n=1,2,3...}^{\infty} V_n \sin(2\pi n f_o t) + \phi_n, \tag{6.2}$$

where V_n and ϕ_n denote the RMS value and phase angle respectively of the n_{th} harmonic component.

The frequency response of Z_{Th} is estimated from the Thevenin equivalent voltage waveform $v_{Th}(t)$, the perturbed supply voltage waveform at the PCC $v_p(t)$, and the perturbation current $i_p(t)$. Two frequency-domain methods can be used to model Z_{Th} [36], [60]. In the first approach the impedance is obtained by dividing the Fast Fourier Transform (FFT) of $\Delta v(t)$ by the FFT of $i_p(t)$, as given by

$$Z_{Th}(w) = \frac{\mathcal{F}\{\Delta v(t)\}}{\mathcal{F}\{i_p(t)\}}. \tag{6.3}$$

The FFT approach is, however, affected by system nonlinearities and noise in practice [36], [60]. The second approach of estimating the frequency response of Z_{Th} involves the use of correlation methods, using the PSD as discussed in Section 4.3. With this method, it is possible to improve the SNR by averaging out the uncorrelated noise in the measurements. The absolute errors in the estimated frequency spectrum at frequencies where the measured voltage and current signals are low can thereby be reduced significantly.

6.3.3 Challenges associated with grid impedance measurements

The Thevenin equivalent grid impedance Z_{Th} and source voltage V_{Th} are both stochastic in nature. The grid impedance changes with changes in the network topology and with varying load. The source voltage variation is a result of variations in the fundamental frequency, harmonic components and non-characteristic sub-harmonic components. This non-stationary nature of the power system has been identified as a problem for characterising grid impedance [3], [21], [22], [23], [60]. The supply voltage fundamental frequency and harmonic components, for example, can appear in the estimated frequency spectrum of the impedance [3]. This distorts the frequency response curve of the estimated system impedance, especially in the har-

monic frequency band. The practical problems encountered in grid impedance measurements can be summarised as follows:

- *Synchronization of pre-and post-Excitation voltages* $v_{Th}(t)$ *and* $v_p(t)$: If it is assumed that $v_{Th}(t)$ is stationary and repetitive, $\Delta v(t)$ can be calculated as formulated in (6.1). This can be done by recording an equal number of cycles of pre-excitation voltage $v_{Th}(t)$ and post-excitation voltage $v_p(t)$ and applying (6.1). In a real power system, however, time varying nonlinear loads induce dynamic voltage harmonics. The voltages $v_{Th}(t)$ and $v_p(t)$ phasors are, furthermore, not likely to be measured on the same reference angle, which gives rise to errors in the calculated impedance response [3], [21], [22], [23], [60] .

- *Frequency variation of the supply voltage* : The fundamental frequency of a power system rarely remains stationary. A change in the fundamental frequency during a measurement period results in a phase shift between the pre-and post-excitation waveforms [21], [22]. This translates into significant phase shifts at harmonic frequencies. Due to the presence of the phase errors, the recorded pre- and post-excitation data are not synchronised sufficiently to provide maximum cancellation of harmonics.

- *Variation of the voltage harmonic components*: The time-varying nonlinear loads connected to the supply network result in voltage harmonics and subharmonics that are stochastic in nature. The amplitudes of these components can thus change during the measurement period. This results in inaccuracies in the estimated frequency response of the system.

The following solutions have been reported in the literature to the problems mentioned above :

- *Short observation windows*: This solution involves the use of impulse or transient perturbations to excite the network under test and using short sections of recorded data to compute the impedance. The assumption in this case, however, is that the system under test is stationary within the selected data window. Staroszczyk [3] proposed the use of an impulse perturbation signal and a 40 ms observation window to compute the impedance. Sumner *et al* [21] used a triangular current pulse as excitation signal, with an 80 ms observation window. Xu *et al* [22] proposed the use of transient excitation obtained by switching a capacitor, and recorded the pre- and post-excitation waveforms in one continuous record. Windows of the pre-excitation and post-excitation data, which are one fundamental frequency period in length and start from a reference time such as the first zero-crossing point, are then selected for analysis.

Although this method has been shown to improve the results, the assumption that short data windows will be insensitive to the non-stationary nature of the power system is not always correct. Due to the short measurement periods, the frequency resolution of the results is, furthermore, poor. Since the transients used in the excitation are rapid, the methods require high-speed data acquisition instrumentation. Céspedes *et al* [23] noted that, with online impulse excitation, the grid impedance could not be approximated well beyond 2 kHz due to insufficient resolution in the recorded perturbation impulse.

- *Discarding the impedance estimated at the fundamental and harmonic frequencies*: The errors in the impedance frequency response due to synchronisation and grid variations typically appear at the fundamental and harmonic frequencies. Sumner *et al* [21] proposed discarding the impedance values around the fundamental and harmonic frequencies and extrapolating the linear part of the impedance from the inter-harmonic frequencies.

- *Detecting and correcting errors caused by changes in supply frequency*: Methods such as those reported by Sumner *et al* [21] and Xu *et al* [22] can be used to detect and correct errors caused by changes in supply frequency. The phase difference between the first and the last steady-state cycles of the pre-excitation or the post-excitation fundamental voltage waveforms are calculated and used to correct the recorded data section that is used for impedance calculation.

6.3.4 Measuring instrumentation

Due to the requirements imposed by wideband excitation and data acquisition at relatively high voltages, grid impedance measurements require dedicated instrumentation. The measurement equipment should have high bandwidth, high accuracy and high dynamic range, and the data acquisition instrumentation should have a high sample rate and resolution. The measurements conducted for this investigation made use of the following commercial products:

(a) *Voltage and current measurements*: The voltage signals were measured using GwInSTEK GDP-025 differential probes. This probe has a bandwidth of ranging from dc to 25 MHZ, with an accuracy of $\pm 2\%$ over this frequency range, and can be used for voltage measurements up to 1400 V_{p-p}. The current signals were measured using Tektronix A622 current probes. This probe has a bandwidth ranging from dc to 100 kHz and can measure currents from 50 mA to 100 A peak.

(b) *Data acquisition system*: The CompactDAQ data acquisition platform manufactured by National Instruments is used in the investigation. The CompactDAQ chassis can accommod-

ate several input modules, that provide direct sensor connectivity, and controls the timing, synchronisation and data transfer between these modules and an external host computer. The CompactDAQ chassis features USB, Ethernet or WiFi connectivity. Table 6.1 summarises the specifications of the NI 9223 input module used in the investigation. The module implements simultaneous analogue-to-digital converters (ADCs) and the current and voltage probes are connected to the module via a Bayonet Neill Concelman (BNC) connector interface.

Table 6.1: Specifications of the NI 9223 input module.

Number of channels	4 analog input channels	**ADC Resolution**	16 bits
Maximum sampling rate	1 MS/s/channel	**Input signal level**	$\pm$10V

(c) *Software*: The CompactDAQ platform can be used with LabVIEW or Matlab software installed on a host computer. This allows for data acquisition, analysis, visualisation and management to be customised. A dedicated Matlab application was developed to acquire the sampled data from the DAQ system for this investigation. The Matlab application implements various functions to configure and run a data acquisition session. Parameters such as the number of input channels, sampling rate and duration of acquired data can be set in the Matlab code.

Figure 6.4 shows a block diagram of the data acquisition arrangement used for the experimental procedures.

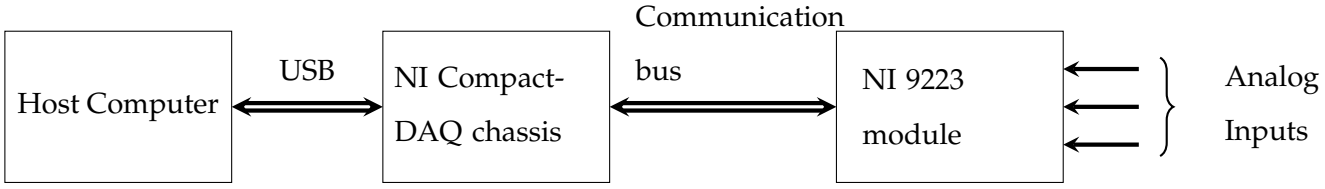

Figure 6.4: Block diagram of the data acquisition system.

6.3.5 Proposed grid impedance measurement and data preprocessing methodology

A novel data acquisition methodology is proposed to synchronise the pre-excitation and post-excitation voltage waveforms with the view to address the challenges described in section 6.3.3. The variations in the background harmonics can be described as random noise that can be

reduced using the statistical technique of signal averaging, thereby enhancing the quality of the grid impedance measurements. Averaging is a useful technique for noise signals with an expected value of zero [62]. The assumption made in applying the averaging technique is, that although both the impedance Z_{Th} and the source voltage V_{Th} are stochastic, the variations in V_{Th} are random and much faster compared those of Z_{Th}, and can thus be described as white noise. The true grid impedance should, therefore, be consistent when repeated measurements are conducted in rapid succession.

The frequency response of the grid impedance can be represented by the relationship

$$Z_{Th}(\omega) = Z_{Th,desired}(\omega) + Z_{noise}(\omega), \tag{6.4}$$

where $Z_{Th,desired}(\omega)$ denotes the desired frequency response and $Z_{noise}(\omega)$ denotes the frequency response of the noise due to the stochastic nature of the power system.

An interleaved perturbation and data capturing scheme, with averaging of multiple estimated impedance responses, is proposed with the view to achieving improved grid impedance measurements. In the case of interleaved data capture, a long measurement at V_{PCC} is recorded, during which switch S in Figure 6.3 is alternately switched on and off at intervals of approximately 1 second. Multiple pre-excitation and post-excitation data sequences are thereby captured. The consecutive pairs of the sampled pre-excitation and post-excitation sequences of $v_{Th}(t)$, $v_p(t)$ and $i_p(t)$ are then used to calculate the $Z_{Th}(w)$. Multiple impedance responses, which can later be averaged, are thereby obtained. The pre-excitation and post-excitation sequences occur in close temporal proximity, thereby minimising adverse effects due to grid variations. The interleaved measurement methodology is illustrated in Figure 6.5, which shows how the sampled waveform of $V_{PCC}(t)$ is partitioned into multiple sections of pre-excited voltage and post-excited sections.

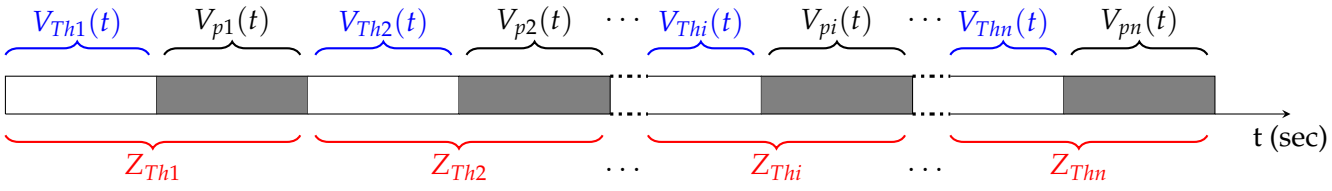

Figure 6.5: Interleaved pre-excitation and post-excitation sequences of the unperturbed voltage $V_{Th}(t)$ and perturbed voltage $V_p(t)$.

The impedance frequency responses calculated for the consecutive pairs of the sampled pre-excitation and post-excitation partitions are averaged to obtain the estimated frequency

response. Random noise adds destructively in this process. The averaging process is defined by the relationship

$$Z_{Th,desired}(\omega) = \frac{\sum_{i=1}^{n} Z_{Thi}(\omega)}{n}, \tag{6.5}$$

where $Z_{Thi}(\omega)$ denotes the impedance response calculated for the i^{th} partition.

In order to calculate $\Delta v(t)$ as formulated in 6.1, it is necessary to extract $v_{Th}(t)$ and $v_p(t)$ from the waveform recorded for $v_{PCC}(t)$. The waveforms extracted for $v_{Th}(t)$ and $v_p(t)$ must be synchronised in the time domain before $\Delta v(t)$ is calculated. This is achieved by subjecting $v_{PCC}(t)$ to a low pass filter to obtain the fundamental component. From the fundamental voltage waveform, instances of positive zero-crossings are identified. The zero-crossing points are utilised to extract sections of equal length, synchronised at the zero crossings of the fundamental frequency, from the unperturbed and perturbed sections of $v_{PCC}(t)$, as shown in Figure 6.6. Figure 6.7 presents a block diagram of process proposed for extracting the frequency response of the grid impedance.

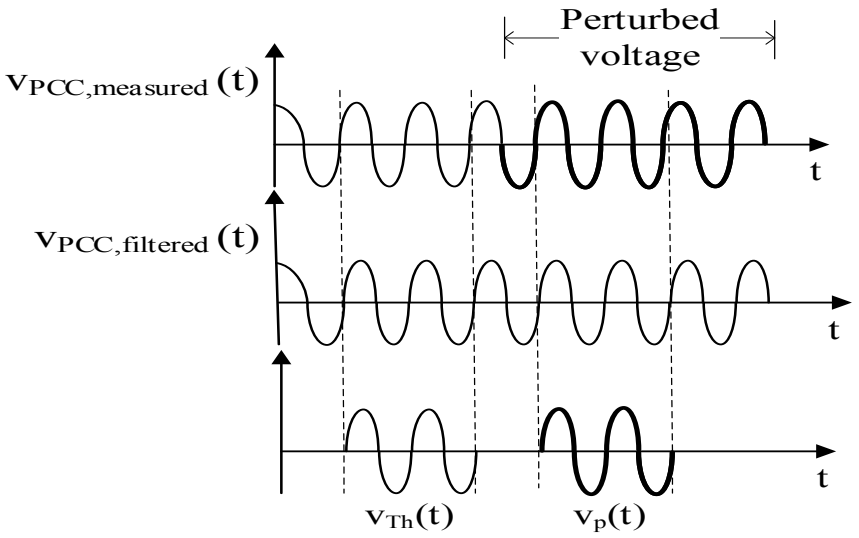

Figure 6.6: Extraction of $v_{Th}(t)$ and $v_p(t)$ waveforms from the measured $v_{PCC}(t)$ waveform.

6.4 Validation of the proposed PRIS perturbation signal and methodology for measuring grid impedance

6.4.1 Introduction

Two case studies are conducted with the view to determine the performance of the PRIS perturbation signal and the proposed methodology for determining the frequency response of a

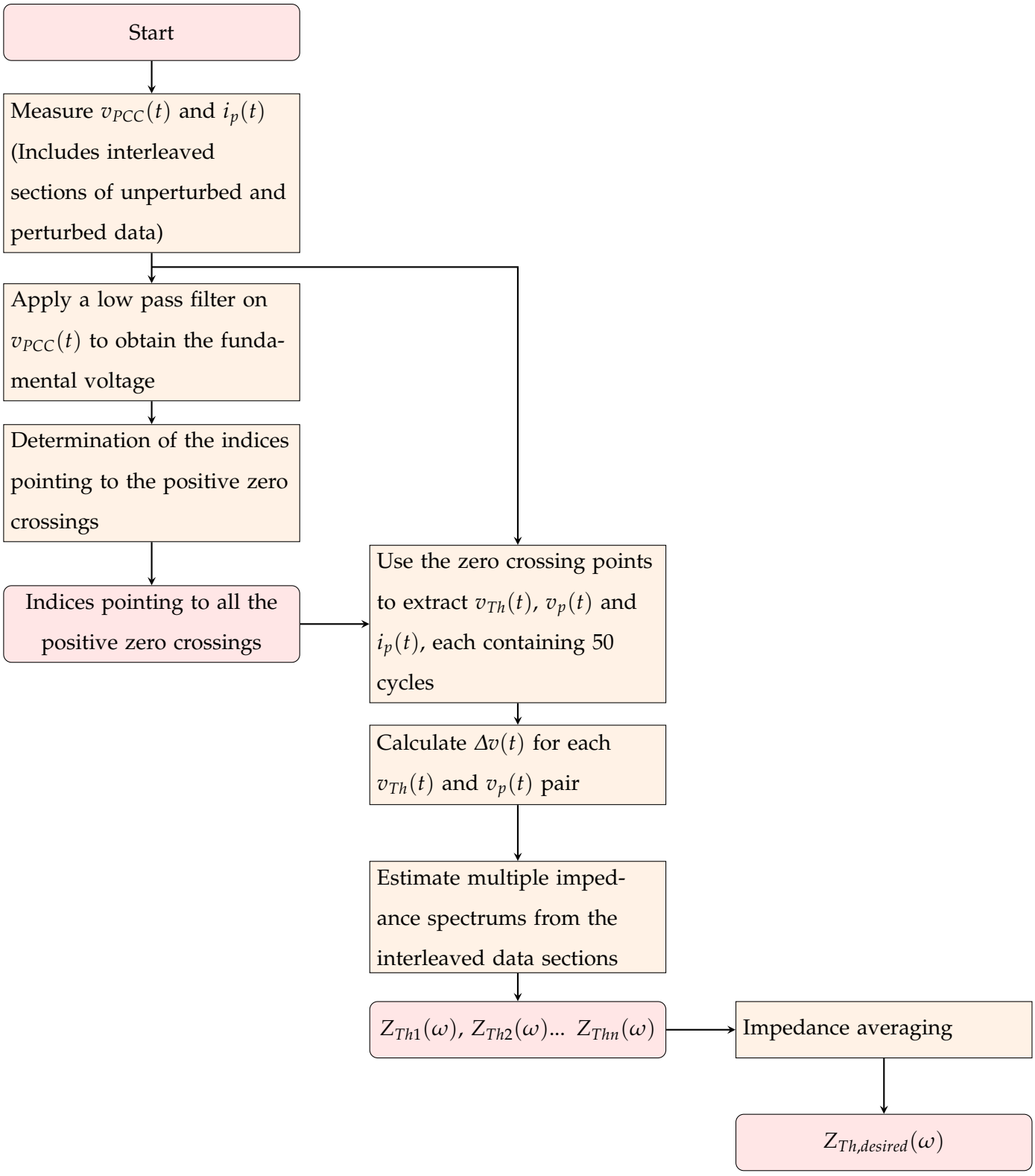

Figure 6.7: Overview of the grid impedance frequency response identification procedure used in this study

Thevenin equivalent grid impedance from *in situ* measurements. The first case study targets the impedance of an experimental network constructed under laboratory conditions, while the

second case study targets a three-phase, 50 Hz, rural supply network. The PRIS source used in the experimental work is designed using the approaches outlined in section 5.3 to achieve persistent excitation of the dynamic modes associated with the target networks. As indicated in section 4.3.3 and shown in Figure 4.4, the spectral energy of the PRIS decreases towards the lower frequency range. Parameters f_{clk}, τ_1 and τ_2 must be chosen to ensure good estimation accuracy over a wide frequency range, including the low frequency range. The relevant voltage and current waveforms are recorded using a sampling frequency of 1 MHz. The frequency responses of the target impedances are estimated from the measured voltage and current waveforms in using the Welch estimator with a Hann window, implemented in Matlab.

6.4.2 Case study I: Laboratory network

6.4.2.1 Network model

This case study targets a network constructed under laboratory conditions to emulate a single-phase LV AC supply network. The frequency response of the Thevenin equivalent impedance of the target network circuit is identified by perturbing the network with a PRIS perturbation current. The frequency spectrum obtained from the experimental approach is compared with responses obtained through a sine sweep simulation and mathematical analysis of the circuit.

The target circuit consists of an inductive Thevenin equivalent AC source and a Pi equivalent cable model. Figure 6.8 shows a lumped parameter circuit model of the arrangement. This topology is commonly found in industrial and residential reticulation systems. It has an application in determining the frequency domain characteristics of a network for applications such as modelling the performance of grid-connected inverters in reticulation systems.

The Thevenin voltage source, $v_{Th}(t)$, is represented by a relatively stiff AC supply grid with a fair degree of harmonic distortion, as is typical for an industrial supply network. The actual Thevenin equivalent impedance of the laboratory supply grid is unknown and is neglected in this application on the basis that it is relatively small compared to the impedance of the cable model. A Thevenin equivalent source impedance is, however, incorporated by including R_1 and L_1 in series with the AC voltage source. The objective of the exercise is to demonstrate the use of the PRIS perturbation system for determining the frequency response of the Thevenin equivalent impedance of a simple LV, 220Vrms, 50 Hz AC supply network topology. Table 6.2 summarises the relevant circuit parameters.

The PRIS source used in this study is realised using a 50Ω resistor, a 100μH inductor, and a 2μF capacitor for the series RLC network. The source is programmed for a PRBS clock frequency, $f_{clk}(t)$, of 10 kHz. The DC input voltage of the PRIS source can be controlled to obtain

an optimum PRIS perturbation current level, that does not exceed the maximum rating of the target elements but provide sufficient excitation. This yielded a value of 60 V for V_{dc} for this experiment.

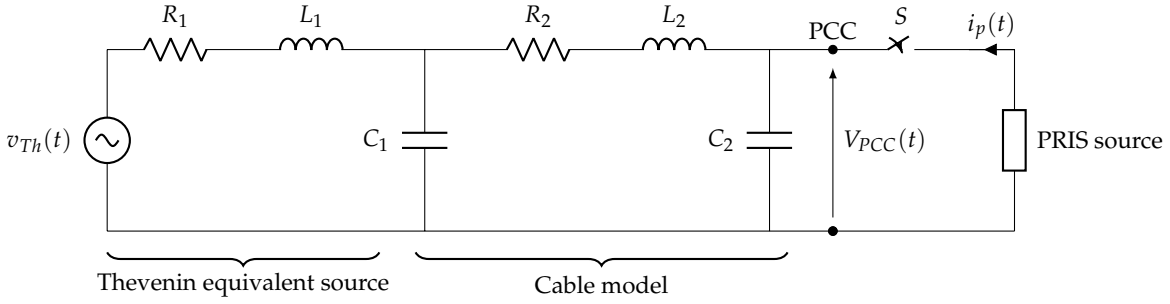

Figure 6.8: Lumped parameter equivalent circuit topology of the supply network implemented for case study 1.

Table 6.2: Parameter values implemented for the circuit topology shown in Figure 6.8.

Parameter	Value	Parameter	Value	Parameter	Value
C_1	1μF	R_1	17.3Ω	L_1	48.22mH
C_2	1μF	R_2	0.7Ω	L_2	0.981mH

6.4.2.2 Analytical solution for the Thevenin equivalent impedance

The Thevenin equivalent impedance, Z_{Th}, of the circuit topology shown in Figure 6.8, as observed from the PCC, can be derived analytically as follows:

- The series combination of R_1 and L_1 form a parallel network with C_1. This impedance is denoted as Z_1, and is represented in the Laplace domain by the relationship

$$Z_1 = \frac{R_1 + sL_1}{s^2L_1C_1 + sR_1C_1 + 1}. \tag{6.6}$$

- Impedance Z_1 appears in series with the series combination of R_2 and L_2. This impedance is denoted as Z_2, and is represented by the relationship

$$Z_2 = \frac{R_1 + sL_1}{s^2L_1C_1 + sR_1C_1 + 1} + R_2 + sL_2. \tag{6.7}$$

- Impedance Z_2 appears in parallel with C_2. This impedance is denoted as Z_{Th}, and is represented by the relationship

$$Z_{Th} = \frac{1}{sC_2} - \left[\frac{1}{s^2C_2^2(R_2 + \frac{R_1+sL_1}{s^2L_1C_1+sR_1C_1+1} + sL_2 + \frac{1}{sC_2})}\right]. \tag{6.8}$$

The frequency response of Z_{Th} can be determined by substituting s with $j\omega$ in 6.8, and inserting the relevant component values.

Figure 6.9 shows a measured section of the waveforms of the PRBS gate drive signal and the PRIS perturbation current obtained for the circuit shown in Figure 6.8. Figures 6.10(a) and 6.10(b) show measured waveforms for a section of the perturbed voltage $V_p(t)$. The results reflect that a bipolar PRIS perturbation signal is superimposed on the sinusoidal supply voltage to the target system.

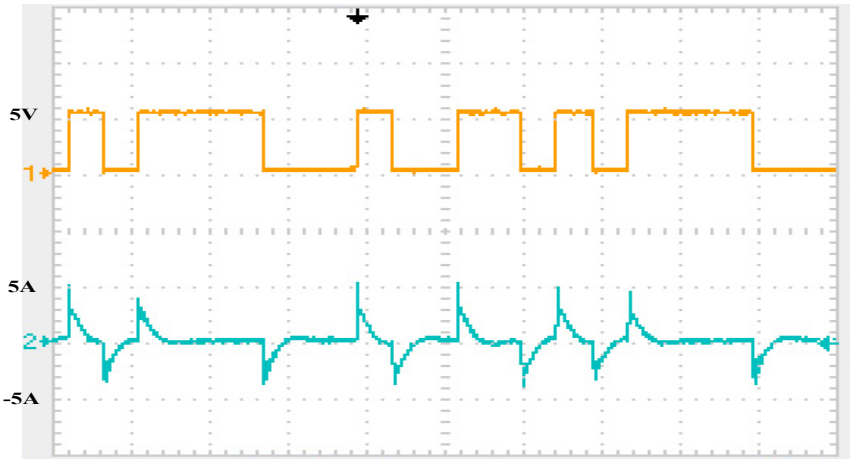

Figure 6.9: Measured waveforms for the PRBS drive signal and the bipolar PRIS perturbation current for case study 1.

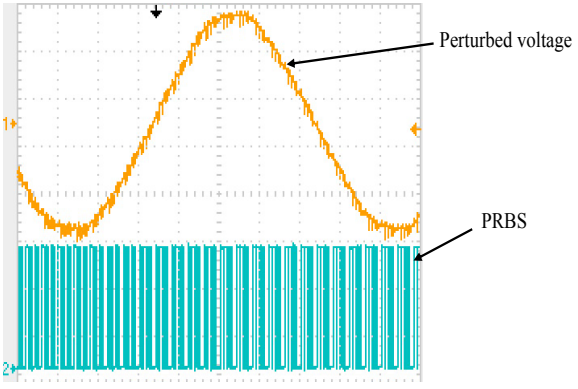

(a) PRBS drive signal and perturbed supply voltage waveform $v_p(t)$.

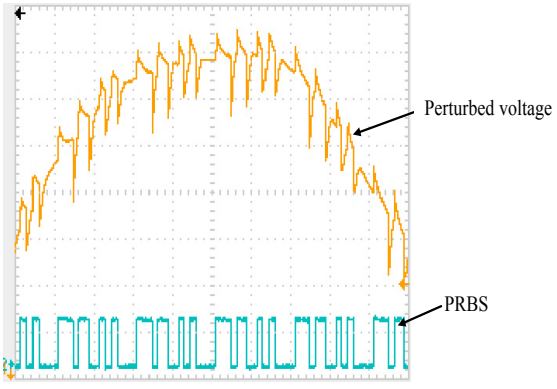

(b) Zoomed PRBS drive signal and perturbed supply voltage waveform $v_p(t)$.

Figure 6.10: Measured waveforms for the PRBS drive signal and perturbed supply voltage $v_p(t)$ for case study 1

Figure 6.11 shows the PSD responses of $v_{Th}(t)$, $v_p(t)$ and $i_p(t)$ obtained with the PRIS perturbation signal. The fundamental component at 50 Hz and harmonic components present in

the harmonic frequency range are evident in the plots. As expected, the $i_p(t)$ frequency response shows that its spectral energy is affected by the impedance characteristics of the target system.

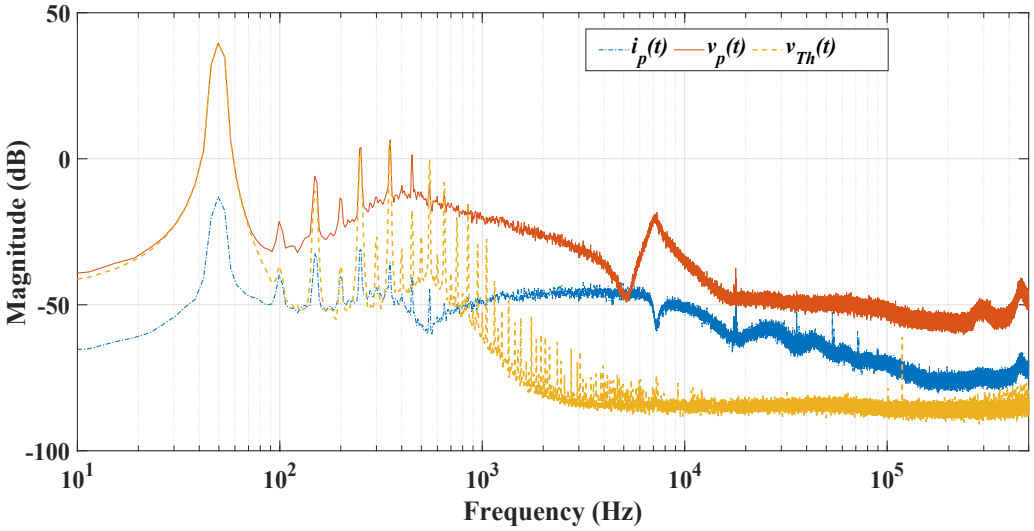

Figure 6.11: PSD responses of the measured perturbation current $i_p(t)$, pre-excitation voltage $v_{Th}(t)$ and post-excitation voltage $v_p(t)$ obtained through PRIS excitation.

The frequency response of the impedance of the circuit shown in Figure 6.8, with the parameter values given in Table 6.2, was simulated using a frequency sweep simulation conducted with DIgSILENT PowerFactory software. The frequency responses, obtained through simulation, the PRIS perturbation measurements and impedance transfer function given by (6.8) are compared in Figure 6.12 for the frequency range between 10 Hz and 60 kHz. The simulated, experimental and analytical results show excellent agreement. The frequency response of Z_{Th} exhibits three resonant frequencies. These resonant frequencies can be derived using the approximate expression

$$f_r = \frac{1}{2\pi\sqrt{LC}}, \tag{6.9}$$

where f_r denotes the resonant frequency, and L and C denote the inductance and capacitance respectively implicated in the resonant circuit.

The first resonant peak occurs at 517 Hz and is attributed to the parallel resonance of L_1 and a parallel combination of C_1 and C_2. The second resonant peak occurs at 7229 Hz and is attributed to the parallel resonance of L_2 and a series combination of C_1 and C_2. A resonant dip occurs at 5100 Hz and is attributed to the series resonance of L_2 and C_1. Beyond the resonant peak at 7229 Hz, the impedance is predominantly capacitive.

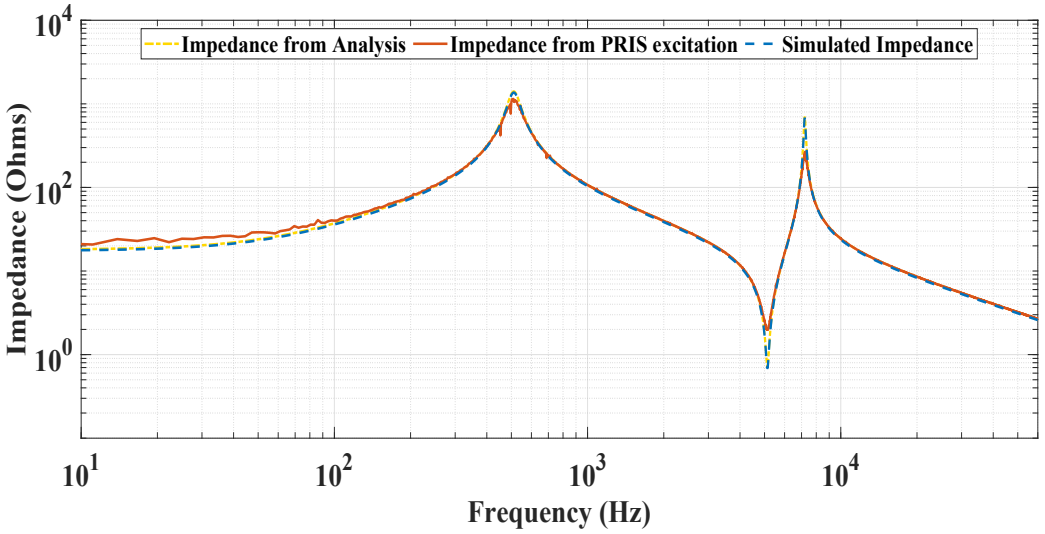

Figure 6.12: Magnitude frequency responses of the Thevenin impedance of the topology shown in Figure 6.8 obtained through a sine sweep simulation, PRIS perturbation measurements and analytical transfer function represented by (6.8).

6.4.3 Case study II: Rural network

6.4.3.1 Network model

Figure 6.13 shows a single line diagram of the three-phase, 50 Hz, rural supply network targeted in case study 2. The network represents an 11kV supply grid feeding agricultural loads denoted by L_1 and L_2, which are connected at Bus 2 and Bus 5 respectively, and an experimental wind generation facility that is connected at Bus 1. Bus 5 is supplied from the 11 kV utility supply through an 11 kV/400 V step-down transformer. Bus 2 is supplied from Bus 5 via a 400 V/3.3 kV step-up transformer, a 3.3 kV cable, and a 3.3 kV/400 V step-down transformer.

The 3.3 kV cable, denoted as cable 2, consists of three XLPE insulated $35mm^2$ aluminium conductors. Bus 1 is supplied from Bus 2 via cable 1, which consists of four XLPE insulated $70mm^2$ aluminium conductors rated at 600/1000 V. Load L_1 consists of fifteen 400 W halogen floodlights distributed across the three phases. Load L_2 consists of fifteen 400 W halogen floodlights distributed across the three phases, four 0.25 kW single-phase induction motors, a 2.2 kW single-phase induction motor, a 37 kW three-phase induction motor, and a 45 kW three-phase induction motor. The motors are operated intermittently. The objective of the study is to characterise the grid impedance observed for each phase at the PCC, which is located at Bus 1, with the wind plant disconnected.

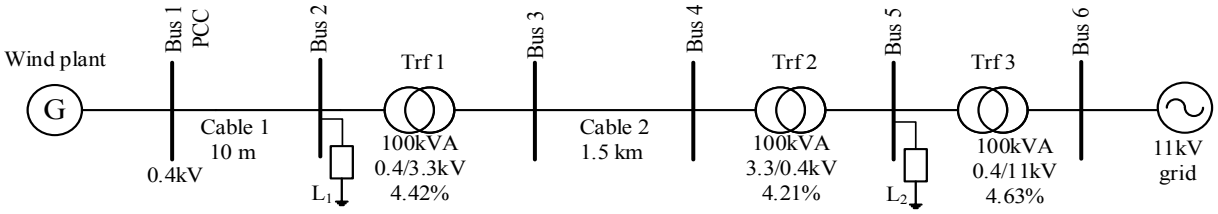

Figure 6.13: Single line diagram of the rural grid targeted in case study 2.

6.4.3.2 Characteristics of the Thevenin voltage source

To investigate the dynamic behaviour of the Thevenin voltage source associated with the target network, a 10 seconds long measurement of the Line to Neutral (L-N) phase voltages $V_{Th}(t)$ is recorded at the PCC at a sampling rate of 1 MHz. The zero-crossing points of the fundamental voltage components are obtained and used to calculate the RMS values of $V_{Th}(t)$ for every cycle.

Figure 6.14 shows a plot of the Probability Density Functions (PDFs) of the RMS voltages for the three phases, together with the expected values, μ, and the Standard Deviation (SD), σ. The PDFs exhibit the properties of Gaussian density functions of the form given by [51]

$$F_V(x) = \frac{1}{\sigma\sqrt{2\pi}} exp\big[-\frac{(x-\mu)^2}{2\sigma^2}\big], -\infty < x < \infty \tag{6.10}$$

where μ and σ denote the mean and the standard deviation respectively. The Gaussian PDF attains a maximum value of $\frac{1}{\sigma\sqrt{2\pi}}$ at $x = \mu$.

The statistical results show that the open-circuit phase voltages at the PCC have a significant random component that is normally distributed. The RMS voltage magnitudes exhibit significant dispersion for all phases, with the largest SD value of 0.412 recorded for phase C. The high variances in the RMS values of the source voltage confirm the presence of non-stationary random variations with white noise characteristics. The difference between the highest and lowest mean values observed for the RMS voltage distributions is of the order of 0.41%. This can be attributed to unbalanced load distributions across the three phases.

The variation in the fundamental frequency is investigated by calculating the frequency of each cycle for the recorded measurement of $V_{Th}(t)$. Figure 6.15 shows a plot of the PDF of the fundamental frequency for each cycle, together with the expected values and standard deviations for each phase. As expected, all of the phases reflect the same mean fundamental frequency, i.e. 49.167 Hz. The frequency PDF exhibits a slight dispersion around the mean, as indicated by the SD value of 0.0037. The results confirm that the grid frequency exhibits a small nonstationary component over the recording interval.

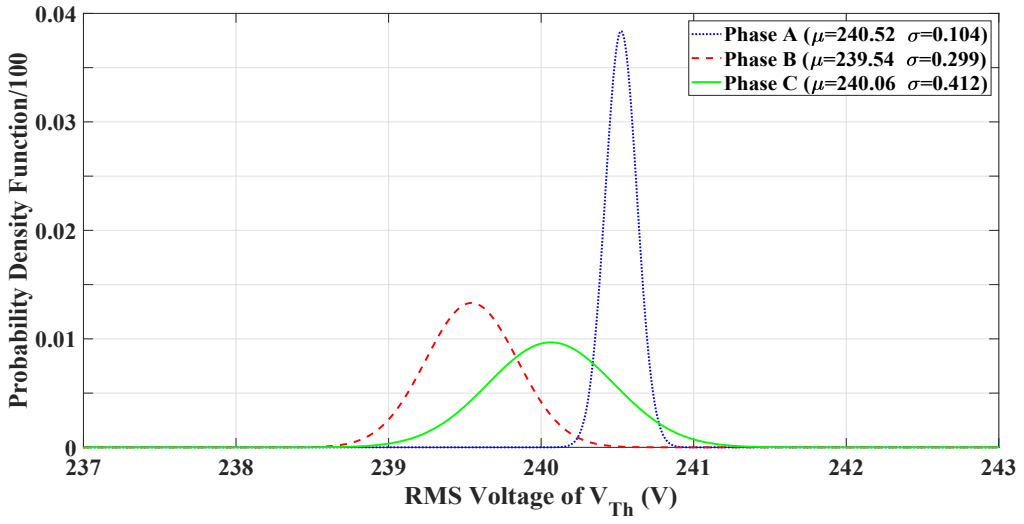

Figure 6.14: Probability density functions of the RMS phase voltages measured over a period of 10 seconds.

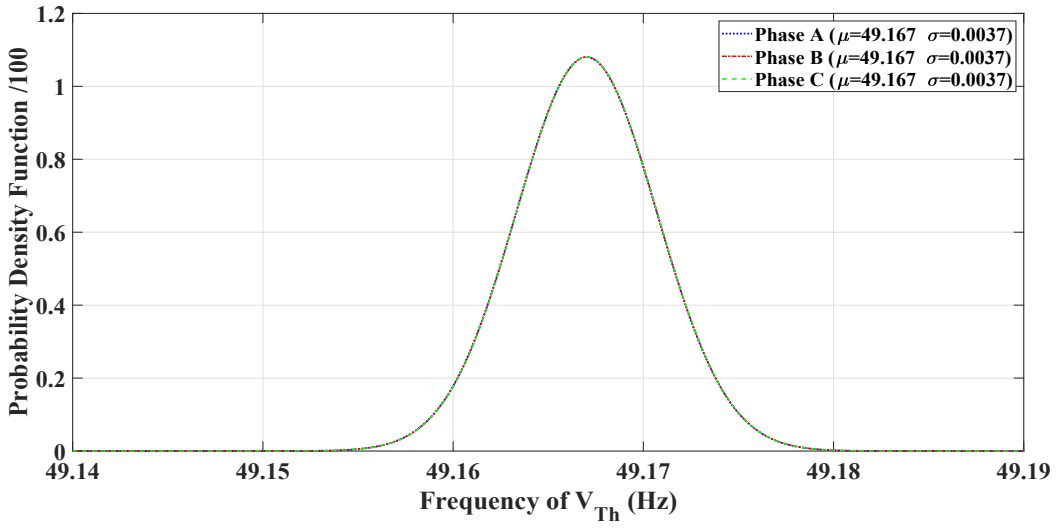

Figure 6.15: Probability density function of the grid frequency measured over a period of 10 seconds.

6.4.3.3 Lumped parameter equivalent circuit grid model

The network depicted in Figure 6.13 is represented in the simulation studies by a lumped parameter equivalent circuit grid model. The cables and transformers are modelled using the generic lumped-parameter equivalent circuit models shown in Figure 6.16(a) and 6.16(b) respectively. Table 6.3 summarises parameter definitions for the model topologies shown in Figure 6.16.

Figure 6.17 shows an approximate circuit model for the network shown in Figure 6.13, with the loads neglected. The interwinding capacitances between the primary and secondary windings of the transformers, denoted by C_{ps}^{T}, are relatively small compared to the cable

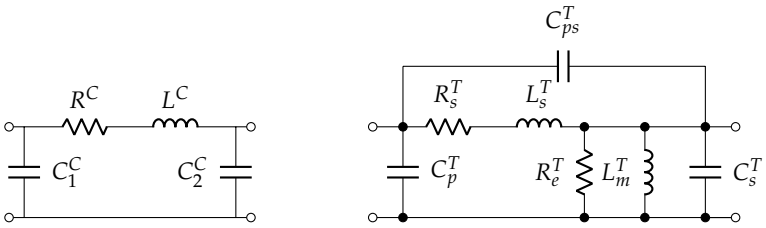

(a) Lumped parameter equivalent circuit cable model.

(b) Lumped parameter equivalent circuit transformer model.

Figure 6.16: Lumped parameter equivalent circuit models implemented for the cables and transformers.

Table 6.3: Parameter definitions for the lumped parameter equivalent circuit cable and transformer models.

Component	**Definition**
C_1^C, C_2^C	Cable capacitances
R^C, L^C	Cable series resistance and inductance
C_p^T, C_s^T, C_{ps}^T	Transformer primary winding, secondary winding and interwinding capacitances
R_s^T, L_s^T	Transformer winding resistance and leakage inductance
R_e^T, L_m^T	Transformer core losses resistor and magnetizing inductance

and transformer winding capacitances and are neglected in a first-order approximation. The transformer core losses resistances, denoted by R_e^T, are large compared to the winding resistances denoted by R_s^T, and are neglected in a first-order approximation. The adjacent parallel capacitors formed by the cables and transformer windings are combined to form equivalent capacitances denoted by C_{eq1}, C_{eq2}, C_{eq3} and C_{eq4}. The 11 kV supply voltage source is represented by a short circuit and the associated source impedance is ignored, as it is assumed to be comparatively small compared to the impedance represented by the rest of the network. These simplifications give rise to the reduced circuit model shown in Figure 6.18.

Approximate parameter values can be estimated for the circuit elements associated with the cable and transformer models shown in Figure 6.17, using manufacturer data sheets and nameplate specifications. The resultant parameter values for the reduced circuit model shown in Figure 6.18 are summarised in Table 6.4.

The frequency responses of the network impedance observed at various nodes in the model shown in Figure 6.18 are simulated over the frequency range from 10 Hz to 1 MHz with the view to gain insight into the resonant modes and the effects of the various circuit components.

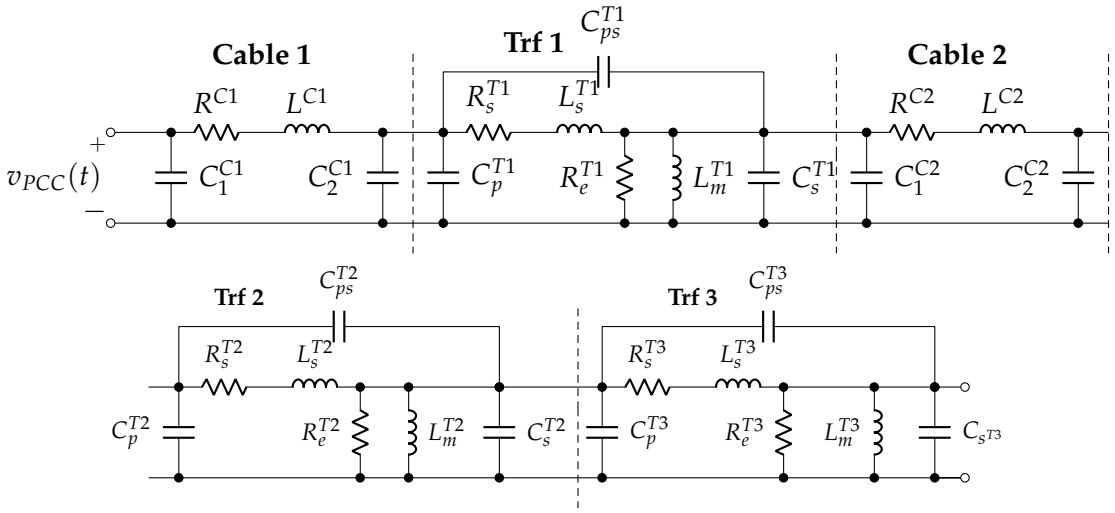

Figure 6.17: Equivalent circuit model for the network shown in Figure 6.13.

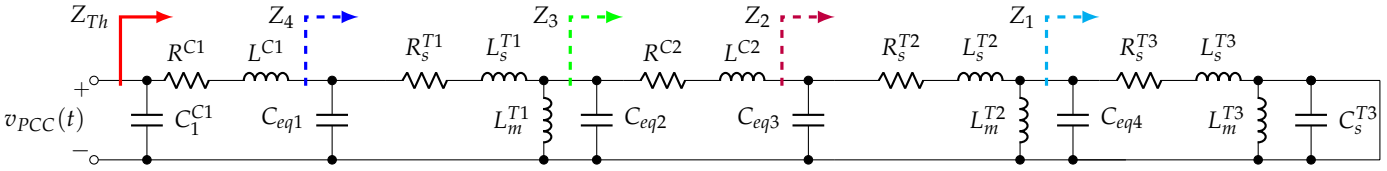

Figure 6.18: Simplified equivalent circuit model for the model shown in Figure 6.17.

Table 6.4: Approximate parameter values for the simplified equivalent circuit model shown in Figure 6.18.

Parameter	Value	Parameter	Value	Parameter	Value
C_1^{C1}	4.05nF	L_s^{T1}	0.463mH	R^{C1}	0.0027Ω
C_{eq1}	8.55nF	L^{C2}	2.08mH	R_s^{T1}	0.01344Ω
C_{eq2}	84nF	L_s^{T2}	10mH	R^{C2}	0.78825Ω
C_{eq3}	0.6μF	L_s^{T3}	0.05mH	R_s^{T2}	0.915Ω
C_{eq4}	2.47nF	L^{C1}	2.4μH	R_s^{T3}	0.0148Ω
C_s^{T3}	0.27μF	L_m^{T1}	100H	L_m^{T2}, L_m^{T3}	100H, 100H

These nodes are indicated as Z_1, Z_2, Z_3, Z_4 and Z_{Th} respectively in Figure 6.18. The impedance simulations are conducted with the parameter values given in Table 6.4, using DIgSILENT PowerFactory software. The simulated impedance responses are shown in Figure 6.19.

The simulated frequency response for Z_{Th} exhibits five resonance frequencies, labeled as R_1, R_2, R_3, R_4 and R_5 respectively. These resonance frequencies also appear partially in the frequency responses observed for Z_2, Z_3 and Z_4. The resonant subcircuits associated with the vari-

ous resonance frequencies can be identified by perturbing the parameter values of the circuit model and observing the effects on the simulated frequency responses. Table 6.5 summarises the resonance frequencies observed in the responses shown in Figure 6.19, and the resonant subcircuits associated with these frequencies.

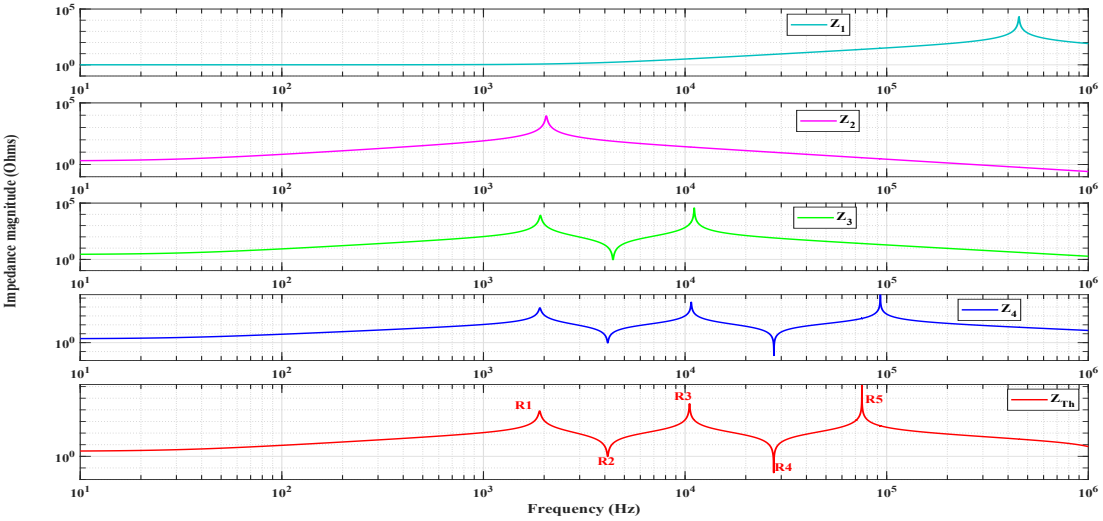

Figure 6.19: Simulated frequency responses for the network impedances observed at nodes Z_1, Z_2, Z_3, Z_4 and Z_{Th} in Figure 6.18.

Table 6.5: Resonant frequencies and the associated resonant subcircuits for the frequency responses shown in Figure 6.19.

Resonance	**Frequency (f_r)**	**Resonant subcircuits**
R_1	1.9 kHZ	Parallel resonance of $(L^{C2} + L_s^{T2} + L_s^{T3})$ and C_{eq3}
R_2	4.1 kHZ	Series resonance of $(L^{C2} + L_s^{T1})$ and C_{eq3}
R_3	12 kHZ	Parallel resonance of L^{C2} and C_{eq2}
R_4	27 kHZ	Series resonance of L_s^{T1} and C_{eq2}
R_5	79 kHZ	Parallel resonance of $(L^{C1} + L_s^{T1})$ and C_{eq1}

6.4.3.4 Impedance response results obtained with the PRIS perturbation methodology

The experimental results for *in situ* application of the PRIS perturbation to the target network shown in Figure 6.13 are obtained by applying the PRIS perturbation signal successively to the phases at the PCC, with the wind plant disconnected. In each case, the PRIS source is connected between the phase conductor and the neutral point. The procedure described in section 6.3.5

is applied to record the voltage waveform $v_{PCC}(t)$ and current waveform $i_p(t)$. Figure 6.20 shows extracts of the time-domain waveforms recorded for $v_{PCC}(t)$ and $i_p(t)$ at the PCC, using the interleaved perturbation strategy. The measured waveforms show the pre-perturbation and post-perturbation periods of length 1 s clearly. The waveforms for $v_p(t)$ and $v_{Th}(t)$ can be extracted and synchronised from the waveform recorded for $v_{PCC}(t)$, using the procedure proposed in section 6.3.5.

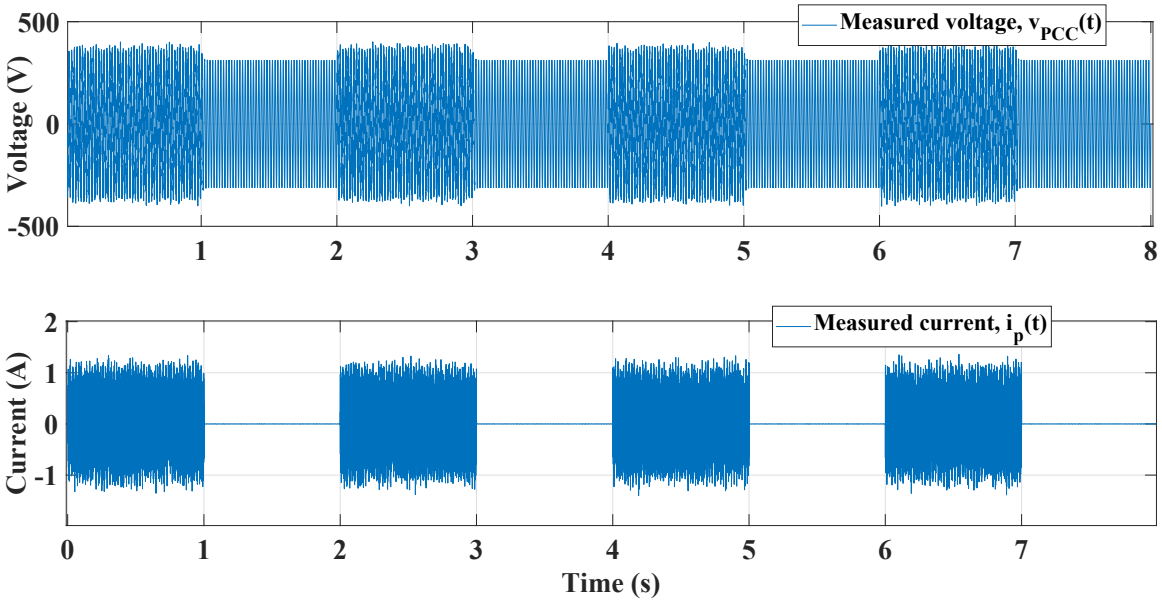

Figure 6.20: Time-domain waveforms measured at the PCC for $v_{PCC}(t)$ and $i_p(t)$ during application of the interleaved perturbation strategy.

Due to the non-stationary nature of the power grid, the length of the data window used for computing the frequency response of the grid impedance influences the results obtained. This is illustrated using measured results from one phase, where the frequency response of the grid impedance is computed using varying lengths of the measured data window. Figures 6.21(a), 6.21(b), 6.21(c), 6.21(d) and 6.21(e) show the estimated magnitude responses of the grid impedance $Z_{Th}(f)$ obtained with data window lengths 0.1 s, 0.2 s, 0.5s, 1 s and 3 s respectively. Due to the interleaved perturbation strategy, this means that the combined duration of the pre-excitation and post-excitation data capture windows are twice these lengths. The frequency responses are focussed in the frequency range from about 100 Hz to 10 kHz to provide a clear view of the harmonic frequency range. The responses obtained for the various data window lengths exhibit a similar general shape, with a coherent parallel and series resonances at approximately 2 kHz and 3.3 kHz respectively. The response obtained using a data window of 0.1 s, which represents 5 cycles for the system frequency of 50 Hz, shows a smooth response

with a frequency resolution of 10 Hz. The limited resolution associated with a relatively short data window, however, affects the accuracy of the estimated frequency response. As the length of the data window increases, the frequency resolution of the estimated responses improves, and the resonance points are more clearly defined. This, however, also results in noise degradation of the responses, especially in the harmonic frequency range. This can be partly attributed to the time-varying nature of the power system harmonics, and possibly supply frequency variations, during the measurement period. As the length of data window increases to 3 sec, the estimated responses exhibit increased noise, especially in the harmonic region.

The proposed averaging strategy is applied for three successive measurements with a data window length of 1 sec, using the interleaved procedure described in section 6.3.5. The data window length of 1 s is selected as it provides a compromise between frequency resolution and spectral noise. Figure 6.21(f) shows the average response obtained from the three individual responses. The result shows that the averaging procedure improves the estimated response in the sense that a smoother, less noisy curve is obtained. The effects of the non-stationary harmonic components are cancelled, which improves the impedance response in the lower harmonic frequency band. The averaging procedure also improves the estimated response in the high-frequency region through noise cancellation. As expected for an inductive supply grid, the estimated grid impedance response is predominantly inductive in the frequency band below 2 kHz, with a gradient of 20dB/decade.

Figures 6.22(a), 6.22(b), and 6.22(c) show the power spectral densities of the measured voltage and current waveforms for phases A, B and C respectively. The fundamental component at 50 Hz and the associated harmonic components are clearly evident in the plots. Figure 6.22(d) shows the estimated impedance magnitude responses for the three phases for the frequency range from 10 Hz to 500 kHz. The phase impedances exhibit well-defined parallel and series resonances at approximately 2 kHz and 3.3 kHz respectively. Phase B shows a second parallel-series resonant pair at 10 kHz and 25 kHz respectively. This second resonant pair is, however, completely damped in phase A and phase C. This can possibly be attributed to the effects of unbalanced loading across the phases due to the presence of single-phase loads. Phases A and C show a further parallel resonant peak at approximately 70 kHz, followed by a series resonance at approximately 130 kHz. Minor parallel and series resonances are observed in phase B at frequencies between 30 kHz and 100 kHz and in phases A and C beyond 200 kHz. The results demonstrate the complexity and variability of the impedance response characteristics of a practical supply network, especially for the frequency range above 10 kHz. This accentuates the importance of a reliable methodology for determining the wideband responses of grid impedance from *in situ* measurements conducted under dynamic conditions.

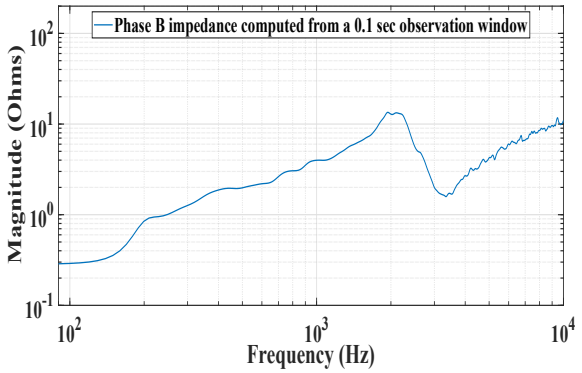

(a) Estimated impedance magnitude response for a data window of 0.1 seconds.

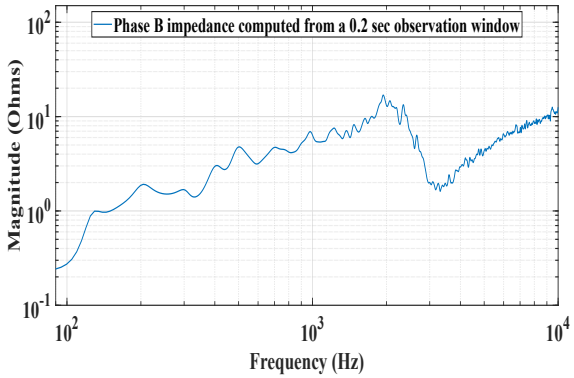

(b) Estimated impedance magnitude response for a data window of 0.2 seconds.

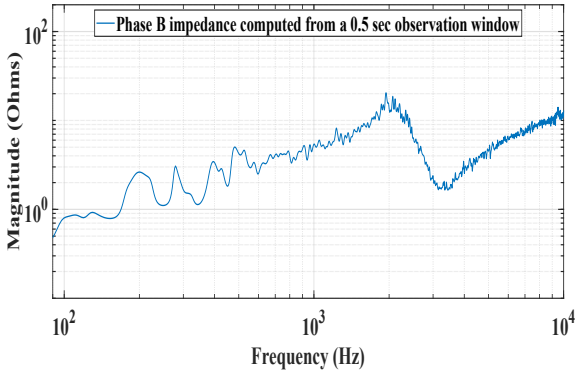

(c) Estimated impedance magnitude response for a data window of 0.5 seconds.

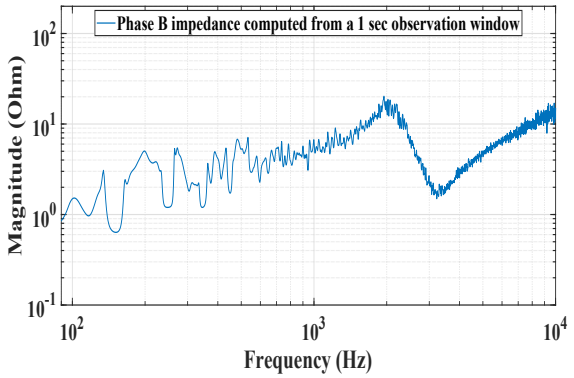

(d) Estimated impedance magnitude response for a data window of 1 second.

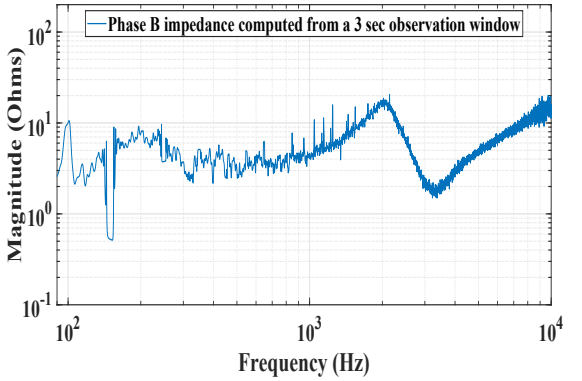

(e) Estimated impedance magnitude response for a data window of 3 seconds.

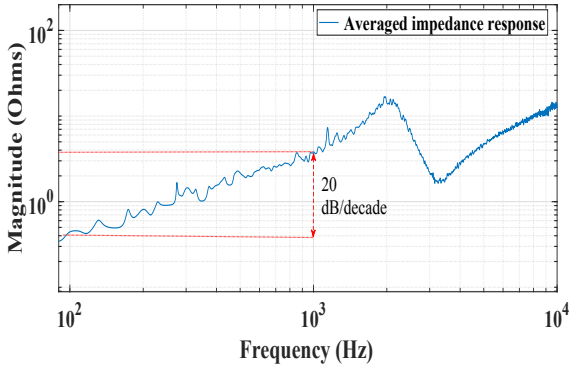

(f) Average impedance magnitude response of three responses obtained with a data window of 1 second.

Figure 6.21: Effects of data window length and averaging on the estimated magnitude response of the grid impedance.

6.4.3.5 Parameter estimation results obtained with the PRIS perturbation methodology

The results presented in Figure 6.22(d) for the impedance responses obtained with PRIS perturbations show a fair degree of similarity with the simulation results presented in Figure 6.19,

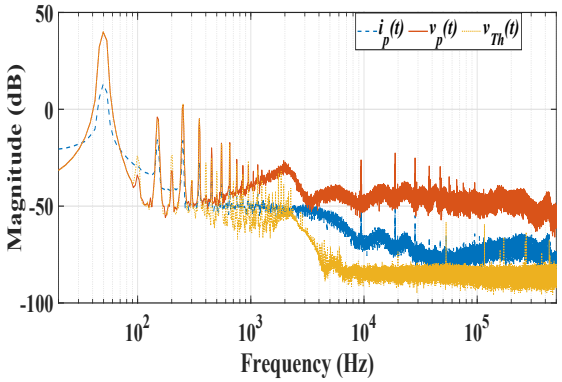

(a) PSD responses of the measured perturbation current $i_p(t)$, pre-excitation voltage $v_{Th}(t)$ and post-excitation voltage $v_p(t)$ for phase A.

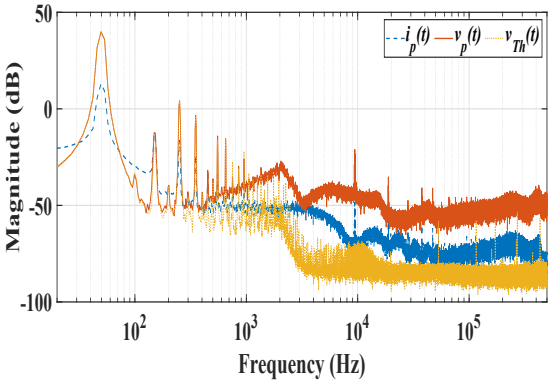

(b) PSD responses of the measured perturbation current $i_p(t)$, pre-excitation voltage $v_{Th}(t)$ and post-excitation voltage $v_p(t)$ for phase B.

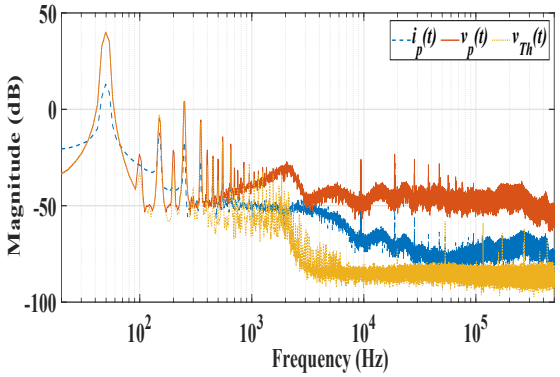

(c) PSD responses of the measured perturbation current $i_p(t)$, pre-excitation voltage $v_{Th}(t)$ and post-excitation voltage $v_p(t)$ for phase C.

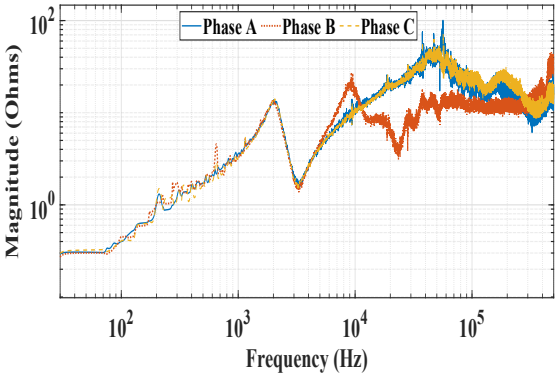

(d) Magnitude responses of the Thevenin equivalent impedance estimated for phases A-N, B-N and C-N.

Figure 6.22: Power spectral density responses of the measured perturbation current $i_p(t)$, pre-excitation voltage $v_{Th}(t)$ and post-excitation voltage $v_p(t)$, and the magnitude responses of the Thevenin equivalent impedance estimated for phases A-N, B-N and C-N.

especially for the lower frequency band. This suggests, that by using the estimated frequency responses of the grid impedance obtained from the proposed experimental procedure, together with the available *a priori* knowledge of the perturbed network, the parameters of the simplified model structure shown in Figure 6.18 can be estimated.

Figure 6.23 shows an overview of the parameter estimation procedure that is implemented for this purpose. The procedure is implemented in Matlab, using a Simulink model for the simplified network representation shown in Figure 6.18. The model is initialised with the parameter values given in Table 6.4. The model takes the measured perturbation current waveform, $i_p(t)$, as the input, and the voltage waveform at the PCC, $v_s(t)$, is simulated. The PSDs of the input current waveform $i_p(t)$ and the simulated voltage waveform at the PCC $v_s(t)$ are

estimated. The simulated frequency response of the Thevenin equivalent network impedance, $Z_s(\omega)$, is subsequently determined using the relationship defined in (6.3). A cost function, ϵ, is derived from the simulated impedance response, $Z_s(\omega)$, and the estimated response obtained by the PRIS perturbation approach, $Z_m(\omega)$, using the relationship

$$\epsilon = \sum_{i=1}^{n} \left(\frac{Z_s(\omega_i) - Z_m(\omega_i)}{Z_m(\omega_i)} \right)^2. \tag{6.11}$$

where n denotes the number of discrete frequency points in the estimated impedance responses.

The cost function returns the normalised sum of the squared errors between $Z_s(\omega)$ and $Z_m(\omega)$, that acts as the input to an optimisation algorithm. The optimisation algorithm seeks to minimise the cost function by iteratively updating the Simulink model with new parameter values.

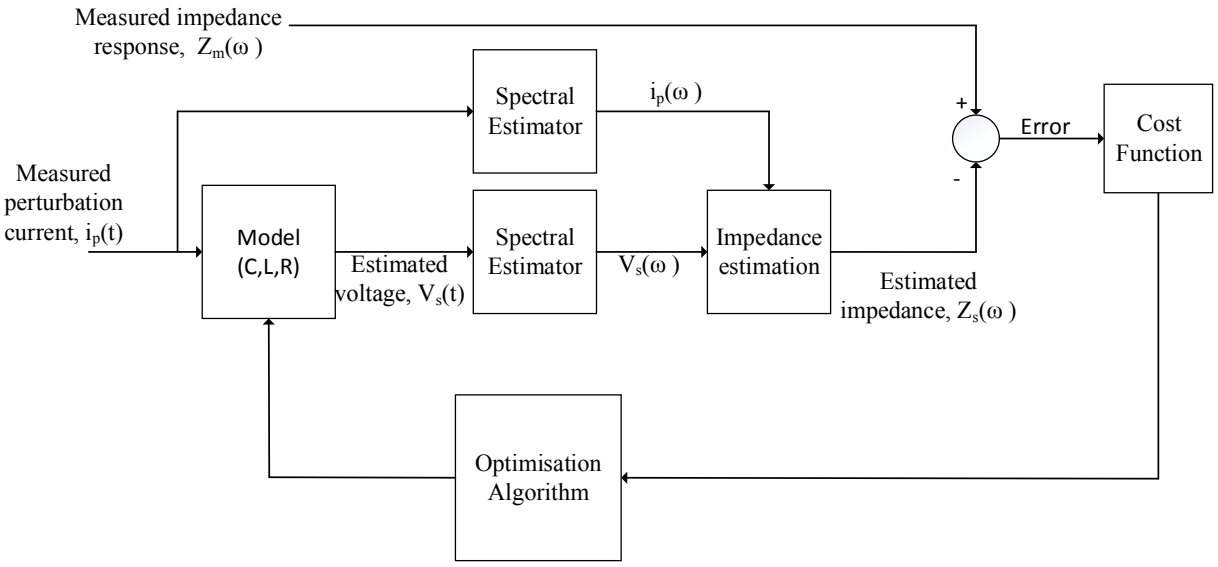

Figure 6.23: Block diagram of the parameter estimation procedure.

The parameter estimation process can be optimised by specifying constraints on the permissible parameter values, based on the *a priori* understanding of the network. For instance, the total leakage inductance, referred to the primary side, for transformer T1, denoted by L_s^{T1}, is less than the total leakage inductance referred to the primary side for transformer T2, denoted by L_s^{T2}. In such a case, an inequality constraint $L_s^{T1} < L_s^{T2}$ is implemented in the parameter estimation algorithm. Constraints are also implemented to avoid negative and zero-valued parameter values.

A variety of optimisation algorithms exist, including those that are based on the gradient method, Newton's method or quasi-Newton methods in solving the cost function [63], [64]. In choosing an appropriate algorithm, factors such as robustness, efficiency, and accuracy should

be considered. The ideal algorithm should, ideally, be able to solve a wide range of problems in its class and use the available computing power efficiently. Generally, however, a compromise has to be made since different arguments can be made in favour of one algorithm over another. It is, furthermore, important to consider whether there is a need to apply any constraints in the estimation problem while selecting an optimisation algorithm.

The *fmincon* solver implemented in Matlab is adopted in this investigation due to its capability to efficiently minimise a constrained multivariable objective function. The *fmincon* solver is a nonlinear solver that implements various algorithms, including the Sequential Quadratic Programming (SQP) algorithm, interior-point algorithm, trust-region-reflective algorithm, sqp-legacy algorithm and active-set algorithm. The SQP has faster execution time and consumes less memory compared to the rest and is hence adopted in this investigation.

The model parameters for the individual phase networks are estimated separately to capture the phase-dependent load characteristics. The estimation procedure focusses on the frequency band between 10 Hz and 10 kHz. A multi-step approach is implemented, whereby the parameters that dominate the lower frequency band are estimated first, and the estimation is extended from there to include more parameters.

A total of 15 parameters from Figure 6.18 are estimated. These include 5 capacitors, 5 inductors, and 5 resistors. The parameters for each phase are estimated separately. The damping effects at the various resonance points were used to approximate the total connected load impedance. This can be done by including loads at the appropriate points on the network model as indicated in Figure 6.8. The loads are initially adjusted manually and their effects on the frequency response of the impedance are observed. The parameter estimation procedure is then performed with the loads included, once a reasonable agreement between simulated and experimental frequency response is achieved.

Very similar results were obtained for the estimated cable and transformer parameters across the three phases. The load values for the individual phases, however, differ considerably, with phase A and phase C showing similar load characteristics. Table 6.6 summarises the parameter values estimated for phase B cable and transformer models. Table 6.6 presents the estimated load values.

The accuracy of the parameters and load values given in Tables 6.6 and 6.7 can be evaluated by comparing the measured and simulated impedance frequency responses of the grid impedance magnitude. Figure 6.24(a) and Figure 6.24(b) show the measured and simulated frequency responses of the impedance magnitude obtained for phase A using the initial and estimated parameter sets respectively. Figure 6.25(a) and Figure 6.25(b) show the measured and simulated frequency responses of the impedance magnitude obtained for phase B using

Table 6.6: Phase B parameters estimated for the simplified model given in Figure 6.18.

Parameter	Value	Parameter	Value	Parameter	Value
C_1^{C1}	4.05nF	L_s^{T1}	90μH	R^{C1}	0.0015Ω
C_{eq1}	0.603μF	L^{C2}	0.12mH	R_s^{T1}	0.0133Ω
C_{eq2}	2.11μF	L_s^{T2}	0.252mH	R^{C2}	0.092Ω
C_{eq3}	19μF	L_s^{T3}	30μH	R_s^{T2}	0.12Ω
C_{eq4}	4.59nF	L^{C1}	0.0369nH	R_s^{T3}	0.01446Ω

Table 6.7: Estimated load impedance for the network given in Figure 6.8.

Load	Phase A	Phase B	Phase C
L_1	10Ω	23Ω	10Ω
L_2	15Ω	38Ω	15Ω

the initial and estimated parameter sets respectively. The responses obtained for phase C are similar to those obtained for phase A. The results presented in Figures 6.24(b) and 6.25(b) for phase A and phase B respectively, show good agreement between the measured responses and the simulated responses obtained with the estimated parameter sets. The damping associated with the series resonance is, however, predicted less accurately. This can be, possible, attributed to the assumption of purely resistive loads in the estimation process.

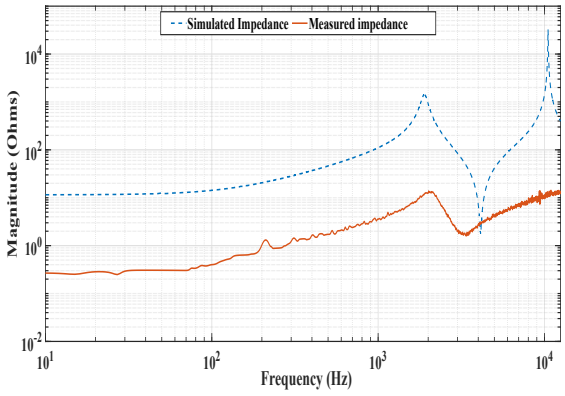

(a) Measured and simulated frequency responses of the impedance magnitude obtained for phase A using the initial parameter set.

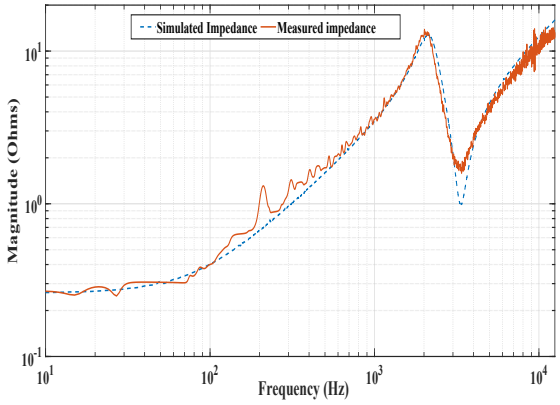

(b) Measured and simulated frequency responses of the impedance magnitude obtained for phase A using the estimated parameter set.

Figure 6.24: Measured and simulated frequency responses of the impedance magnitude obtained for phase A.

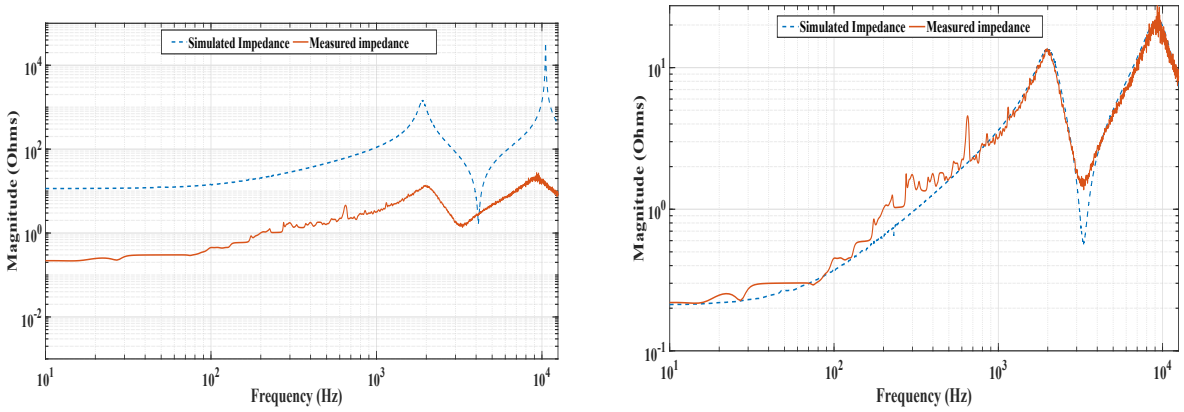

(a) Measured and simulated frequency responses of the impedance magnitude obtained for phase B using the initial parameter set.

(b) Measured and simulated frequency responses of the impedance magnitude obtained for phase B using the estimated parameter set.

Figure 6.25: Measured and simulated frequency responses of the impedance magnitude obtained for phase B.

6.5 Conclusion

The importance of grid impedance measurements is discussed and it is noted that accurate knowledge of the grid impedance characteristics is of importance for power system power quality studies, harmonic filter design and the design of protection systems. It is noted that there are challenges associated with grid impedance identification in relation to measurements conducted on a real distribution system. This is because the power system is non-stationary in the sense that the Thevenin voltage source exhibits variations in its magnitude and frequency. The grid impedance is also influenced by the connected loads. These variations are shown to have a component that is stochastic in nature.

The proposed PRIS source is used *in situ* to perturb an active network with the aim of determining the Thevenin grid impedance frequency response. The spectral energy of the PRIS perturbation current can be controlled to improve the accuracy of the measurement results by manipulating the clock frequency, sequence length and the time constants. A *in situ* measurement arrangement is presented and it is shown that the experiment is conducted in two stages, thus producing two sets of data described as pre-excitation and post-excitation data. To improve the accuracy of the impedance estimation, a novel data acquisition methodology is proposed to perturb the network and synchronise the pre-excitation and post-excitation voltage waveforms. This method aims at reducing the adverse effects of the dynamic nature of the grid on the identified impedance response. The presented results demonstrate the distortion

of the impedance response characteristics of a real supply network, especially in the harmonic frequency range due to the dynamic nature of the grid. The proposed interleaved data capture and impedance averaging procedure is shown to improve the estimated impedance responses through the cancellation of the effects of the non-stationary harmonic components.

The estimated grid impedance characteristics are, furthermore, used to estimate the values of a lumped parameter equivalent circuit of a supply network and the connected loads. The estimation procedure, which includes comparing a measured and simulated impedance response and invoking an optimisation algorithm to minimise the error, is presented. The estimated parameter values are used to obtain responses, which are shown to agree well with the measured responses for the considered frequency band between 10 Hz and 10 kHz.

CHAPTER 7

Conclusions

7.1 Introduction

This chapter summarises the achievements and conclusions of the research presented in this dissertation with reference to the original research objectives. These objectives include the following:

7.2 Research conclusion

7.2.1 Mathematical modelling and analysis of the time-domain properties of the PRIS signal

In the electrical energy field, system identification is typically used for modelling power system grid impedance and apparatus such as transformers, motors, power converters and generators. The methodology used in these system identification and parameter estimation applications involves exciting the target system using a perturbation signal with suitable time-and frequency-domain characteristics. An optimal perturbation signal should persistently excite all relevant modes of the target system. Despite the recent attention on perturbation signals, the case of a suitable signal for high power, high voltage *in situ* applications has not been studied sufficiently as motivated in Chapter 1 and 2.

The research described in this dissertation proposes a unique waveform, namely the pseudo-random impulse sequence (PRIS) as a perturbation signal that is suitable for wideband *in situ* system identification and parameter estimation applications in the power system environment. The PRIS signal seeks to combine the most advantageous characteristics of the classical PRBS signal and the classical impulse waveform used in high voltage engineering. The time-domain properties of the PRIS signal, including the mathematical formulation and wave shape properties, are discussed. The PRIS waveform is shown to consists of a sequence of pseudo-randomly occurring, pseudo-randomly chopped impulses. The two variations of the PRIS, the unipolar and bipolar PRIS signals are introduced and the time-domain analysis presented. The derived time-domain mathematical functions indicate that the PRIS time-domain properties can be controlled by manipulating the clock frequency and length associated with the PRBS as well as the two time constants associated with the impulse waveform.

An approach to simulate the PRIS is presented in Simulink, a platform that represents a convenient tool for time-domain analysis and that offers extensive support for frequency-domain analysis. The simulation of the PRIS is implemented using a linear feedback shift register, modulo-two gates, transfer function blocks, HitCrossing blocks and a switch that allows selection of positive and negative impulses based on the PRBS logic.

7.2.2 Mathematical modelling and analysis of the frequency-domain properties of the PRIS signal

System identification and parameter estimation applications require the implementation of a perturbation signal with suitable frequency-domain properties. The proposed PRIS signal is modelled and analysed in the frequency-domain and the results discussed in the context of the suitability of the PRIS for system identification and parameter estimation applications in the field of power engineering. The derived frequency-domain mathematical function is shown to agree well with simulation results. The PRIS has several advantages which make it attractive for frequency response measurement applications:

- As it is a wideband signal, the PRIS ensures that measurements can be conducted rapidly. This is an advantage especially in power system measurements where grid parameters change with operating time.

- The derived frequency-domain mathematical expressions and simulation results indicate that the PRIS has a fair degree of controllability in the sense that the frequency-domain properties can be adjusted by manipulating the associated parameters including the PRBS clock frequency, PRBS length and the two time constants, τ_1 and τ_2. The controllability of the PRIS allows it to be adjusted to improve the crest and time factors of the signal. Persistent excitation for a wide range of applications can, therefore, be achieved. The PRIS parameters can also be adjusted such that its spectral energy is focussed in the frequency band of interest, thereby improving the signal-to-noise ratio (SNR) and accuracy of the measurements. Applications, especially in systems involving electromagnetic components such as transformers, perform best where perturbation energy is focussed towards the upper frequency band and the low frequency excitation is limited. The PRIS, by controlling its parameters, can facilitate such an application.

- The PRIS, is deterministic yet random within each period. The deterministic characteristic of the PRIS facilitates repeatable experiments.

- The proposed PRIS signal is bipolar which is advantageous because the target system is not driven towards a biased offset point from the operating point prevailing at the start of the measurement.

7.2.3 Development of a perturbation source circuit topology that is optimal for *in situ* high power, high voltage applications

It is important to generate the perturbation signals for use in energy applications efficiently using circuit topologies that are compatible with the associated high power and high voltage environments. The conventional methodologies in the literature such as the sine sweep, classical PRBS current source and the PRBS voltage source connected through a resistor have inherent limitations in this environment. Such limitations include lack of suitability for *in situ* experiments and high power ratings of the associated perturbation sources. For instance, generating signals with binary states such as the PRBS for a current injection perturbation source requires the state switches to operate in linear mode, which gives rise to high power ratings for the switching components.

A novel and efficient circuit topology for generating the PRIS for high power applications is proposed and analysed. The circuit topology consists of an H-bridge and a series RLC circuit connection to the target. The merits of the proposed PRIS circuit topology for high power *in situ* perturbation applications can be summarized as follows:

- It is shown that the power electronic switches used in the H-bridge are controlled, using a PRBS logic signal, in an on/off mode, thereby reducing power losses and allowing an efficient circuit to be designed to operate in the kV range.

- The series RLC circuit attenuates the fundamental frequency current component induced by the Thevenin voltage source in case of *in situ* measurements, preventing the circulation of the AC current in the perturbation source circuit. This, furthermore, reduces power losses in the PRIS source circuit. Comparison of the PRIS current and the PRBS voltage source circuit topologies indicated at fundamental frequency component attenuation to the tune of 40 dB in the PRIS source. The average power loss across the resistor, over one PRBS period, is shown to be approximately 35 times less in the PRIS source circuit in comparison to the PRBS voltage source circuit.

- From a practical circuit perspective, the PRIS time constants τ_1 and τ_2 are controlled by adjusting the reactive elements in the PRIS source circuit. The series RLC circuit, there-

fore, offers the capability of controlling the time-and frequency-domain properties of the PRIS to suit various identification applications.

- The DC input voltage source of the PRIS source circuit allows for control of the PRIS excitation level. To improve the SNR, the dynamic range of the PRIS can be increased by increasing the DC voltage. In cases where a low perturbation level is required to avoid nonlinear distortion, the excitation level can also be reduced by decreasing the DC voltage.

The input impedance of the system under test can have considerable influence on the time- and frequency-domain characteristics of the resultant perturbation current. In practice, the system under test is expected to exhibit complex frequency-dependent input impedance characteristics. The effects of the target system on the PRIS perturbation signal are investigated. The design considerations for a practical PRIS source are presented and it is noted that the design of an optimum PRIS source for a system identification experiment is highly dependent on the characteristics of the target system.

Mathematical analysis of the proposed PRIS source reveal that in a practical PRIS source, the initial energy in the series inductor and capacitor has an influence on the shape of the chopped impulses of the PRIS waveform. The initial energy in these two elements depends on the length of each switching cycle in the PRIS source, which is pseudo-random. This will cause the maximum amplitude of the chopped impulse waveforms associated with the PRIS to differ slightly.

7.2.4 Performance evaluation of the proposed PRIS signal and perturbation source for wideband characterization of grid impedance

The performance of the PRIS perturbation system in *in situ* applications is evaluated using two case studies involving the estimation of the impedance spectrum of a complex Thevenin source in the presence of harmonic voltage distortion. The challenges associated with grid impedance measurements, due to the non-stationary nature of a real power system network, are highlighted. This research demonstrates that the grid Thevenin source voltage has amplitude and frequency variations that can be described as stochastic in nature and imitating white noise characteristics. These variations distort the measured grid spectrum in the harmonic frequency band resulting in erroneous results.

To improve the grid impedance frequency response results, this research proposes a novel procedure for grid perturbation, data recording, synchronization of pre-and post-excitation and impedance computation. An interleaved method of perturbing the network using the PRIS

at the point of common coupling (PCC) is demonstrated. This technique involves taking a long measurement that contains alternating pre-and post-excitation data. An advantage of this approach is that multiple impedance responses can be computed from pre-and post-excitation data that occur in quick succession. Averaging of these impedance responses is shown to improve the estimated response in the sense that a smoother, less noisy curve is obtained.

It is shown that the length of the data window that is used in the analysis affects the quality of computed grid impedance frequency response. The use of a short length of data, which is one of the methods that is proposed in the literature as a way of improving impedance results, is shown to present impedance results with a poor resolution which affects the accuracy of the impedance spectrum. Long data windows, on the other hand, are influenced by the harmonic changes in the power system resulting in distortion of the impedance spectrum. It is, therefore, necessary to strike a compromise between resolution and distortion while selecting the length of the data window for impedance response computation.

In the first case study, a PRIS perturbation system is used to estimate the impedance frequency response of a test circuit that is built in the laboratory to emulate a single-phase AC supply network. The presented results show that the PRIS waveform excites the various dynamic modes of this system persistently and the frequency spectrum of the impedance is extracted accurately from the perturbed voltage and current signals. The results are shown to agree well with those obtained from a mathematical transfer function representing the network impedance and frequency sweep simulation of the network using DIgSILENT PowerFactory software.

In the second case study, a PRIS perturbation system is used to estimate the phase to neutral impedance spectrum of a complex Thevenin source in a three-phase rural network. The obtained frequency responses are subsequently used to estimate the lumped parameter values of the associated network components including the transformers, cables and loads. The presented results show that the PRIS waveform and the proposed perturbation and data analysis procedure can provide reliable impedance estimation results, even on a real power system network where harmonic voltage distortion is prevalent.

The proposed method has application in renewable energy systems for characterizing grid impedance for grid compliance studies, harmonic filter design and the modelling of harmonic distortion phenomena. The proposed PRIS perturbation signal has, furthermore, excellent potential for system identification and parameter estimation in applications that target power apparatus such as transformers, electrical machines, etc. It can, however, also be applied for small-signal applications such as control systems.

7.3 Recommendation for future work

This study revealed several areas for further investigation.

- The power cost comparison between the PRIS source with that of the conventional perturbation sources such as the PRBS source is worthy of attention. In practice, this is quite complicated as the comparative performance is dependent on operating conditions such as the DC source voltages used. Furthermore, the actual losses are dependent on the magnitude of the excitation current required which is a function of the estimation application. An aspect of future work is to compare the power cost of a PRIS source with that of the conventional PRBS sources for various experimental applications and conditions.

- A good understanding of the grid impedance characteristics and its variations throughout the day is of importance for applications such as filter design. In this case, a real-time, *in situ*, wideband grid impedance measurement arrangement using the PRIS perturbation source should be designed to capture the grid impedance variations over a long period. The measurement should, furthermore, be conducted such that all the three phases are perturbed simultaneously.

7.4 Novel contribution and research publications

The original contributions associated with this research are listed below:

- *Introduction of the PRIS waveform as wideband perturbation signal for high power, high voltage applications:* The proposed PRIS signal represents a novel concept, that combines a PRBS gate signal with the classical impulse excitation waveform used extensively in high voltage engineering.

- *Time-domain model and analysis of the PRIS signal:* The time-domain properties of the PRIS signal have not been investigated in the literature. It is shown that the signal is highly suitable for *in situ* application in high power, high voltage environment.

- *Frequency-domain model and analysis of the PRIS signal:* The frequency-domain properties of the PRIS signal have not been investigated in the literature. It is shown that the power spectrum of the PRIS has a good degree of controllability in comparison with the classical PRBS and impulse signals, especially in the sense that the frequency spectrum can be manipulated by adjusting the impulse time constants and PRBS clock frequency to focus the spectral energy in the frequency band of interest.

- *Development and performance evaluation of a PRIS source circuit topology:* A novel circuit topology, using a power electronic H-bridge in combination with a series RLC network, is proposed to generate the PRIS signal. It is shown that the circuit represents an efficient and compact perturbation source that has the potential to operate at voltages in the kV range. The effects of the target system to be estimated on the PRIS perturbation current are investigated. The impedance of the target is shown to have considerable influence on the time- and frequency-domain characteristics of the perturbation current. The initial energy in the inductor and capacitor associated with a practical PRIS source are furthermore shown, through mathematical analysis of the PRIS source, to affect the shape of the chopped impulse waveforms that constitute the PRIS.

- *Application of the PRIS signal for wideband characterization of grid impedance:* The proposed PRIS signal is applied for wideband characterization of the grid impedance of a rural supply network, where the supply voltage exhibits a fair degree of harmonic voltage distortion and stochastic behaviour. A novel experimental approach is proposed to minimize the effects of voltage distortion and the time-dependent variation of the supply voltage on the estimated frequency responses and model parameters.

This research has generated the following publications:

- F. M. Mwaniki, H. J. Vermeulen, and J. P. Viljoen "Evaluation of a pseudo-random impulse sequence as an excitation signal for power system equipment," *Proc.* 26^{th} *South African Universities Power Engineering Conference,* Jan. 2018.

- F. M. Mwaniki and H. J. Vermeulen, "Characterization and Application of a Pseudo-random impulse sequence for parameter estimation applications," *IEEE Transactions on Instrumentation and Measurement*, Early Access.

- F. M. Mwaniki and H. J. Vermeulen, "Grid Impedance Frequency Response Measurements Using Pseudo-Random Impulse Sequence Perturbation," *2019 9th International Conference on Power and Energy Systems* (ICPES), Perth, Australia, 10-12 December 2019.

References

[1] T. Soderstrom and P. Stoica: *System Identification*. Cambridge:Prentice Hall International, 1989. 1.1, 1.2, 2.2.1.3, 2.2.3.3, 6.2, 2, 3, 6.1

[2] H. J. Vermeulen, J. M. Strauss and V. Shikoana: Online Estimation of Synchronous Generator Parameters Using PRBS Perturbations. *IEEE Trans. Power Syst.*, vol. 17, no. 3, pp. 694–700, Aug 2002. 1.1, 2.2.3.3

[3] Z. Staroszczyk: A Method for Real-Time, Wide-Band Identification of the Source Impedance in Power Systems. *IEEE Trans. Instrum. Meas.*, vol. 54, no. 1, pp. 377–385, Feb 2005. 1.1, 1.2, 2.2.2.2, 6.3.1, 6.3.3

[4] J. Schoukens, R. Pintelon, E. Ouderaa and J. Renneboog: Survey of excitation signals for FFT based signal analyzers. *IEEE Trans. Instrum. Meas.*, vol. 37, no. 3, pp. 342–352, Sep 1988. 1.2, 2.1, 2.1, 2.2.1.2, 2.2.1.3, 2.2.3.1, 2.2.3.2

[5] H. A. Barker and K. R. Godfrey: System identification with multi level periodic perturbation signals. *Control Engineering Practice*, vol. 7, pp. 717–726, Feb 1999. 1.2, 2.1

[6] K. R. Godfrey, H. A. Barker and A. J. Tucker: Comparison of perturbation signals for linear system identification in the frequency domain. In: *IEE Proc.-Control Theory Appl.*, pp. 535–548. 1999. 1.2, 2.1

[7] A. H. Tan, K. R. Godfrey and H. A. Barker: Design of computer optimized pseudorandom maximum length signals for linear identification in presence on nonlinear distortions. *IEEE Trans. Instrum. Meas.*, vol. 54, no. 6, pp. 2513–2519, Dec 2005. 1.2, 2.2.1.3

[8] P. Guillaume, P. Verboven, S. Vanlanduit and E. Parloo: Multisine excitations new developments and applications in modal analysis. In: *Proc. IMAC 19*. 2001. 1.2, 2.1, 2.2.1.1, 2.2.1.3, 2.2.1.3

[9] M. Vilkko and T. Roinila: Designing maximum length sequence signal for frequency response measurements of switched mode converters. In: *Nordic Workshop on Power and Industrial Electronics*. 2008. 1.2, 2.2.3.3

[10] J. Van Rooijen and H. J. Vermeulen: A perturbation source for in situ parameter estimation applications. In: *Proc. IECON'94 Conf.*, pp. 1819–1823. 1994. 1.2, 2.2.3.3, 2.3

[11] S. Neshvad, S. Chatzinotas and J. Sachau: Online Determination of Grid Impedance Spectrum through Pseudo Random Excitation of a pulse Width Modulator. In: *Int. Conf. on Renewable Energies and Power Quality*. Apr 2014. 1.2, 6.2, 6.3.1

[12] M. Jordan, H. Langkowski, T. Do. Thanh and D. Schulz: Frequency Dependent Grid Impedance Determination with Pulse Width Modulation Signals. In: *Proc.7th Int. Conf.-Workshop Compat. Power Electron.*, pp. 131–136. Jun 2011. 1.2, 6.2, 6.3.1

[13] W. D. T. Davies: *System Identification for Self-Adaptive Control*. New York: Wiley, 1970. 1.2, 2.2.3.3, 2.2.3.3, 3.2.2, 5.3.2, 5.3.2, 5.1

[14] L. Asiminoaei, R. Teodorescu, F. Blaabjerg and U. Borup: A digital controlled PV-inverter with grid impedance estimation for ENS detection. *IEEE Trans. on Power Electron.*, vol. 20, no. 6, pp. 1480–1490, Nov 2005. 1.2

[15] H. Langkowski, T. Do. Thanh, K.-D. Dettman, and D. Schulz: Grid impedance determination-relevancy for grid integration of renewable energy systems. In: *Conference of the IEEE Industrial Electronics Society (IECON'09)*. Nov 2009. 1.2, 2.2.3.3, 2.3

[16] IEC61000: Electromagnetic compatibility (EMC) Part 3 to 6: Limits, Assessment of emission limits for the connection of distorting installations to MV, HV and EHV power systems Edition 2.0. 2008. 1.2

[17] Grid Connection Code for Renewable Power Plants (RPPs) Connected to the Electricity Transmission System (TS) or the Distribution System (DS) in South Africa, Version 2.9. 2016. 1.2

[18] NERSA: Electricity Supply – Quality of Supply. Part 2: Voltage characteristics, compatibility levels, limits and assessment methods. 2007. 1.2

[19] NERSA: Electricity Supply – Quality of Supply. Part 4: Application Practices for Licensees. 2009. 1.2

[20] S. Cobreces and others: Grid Impedance Monitoring System for Distributed Power Generation Electronic Interfaces. *IEEE Trans. Instrum. Meas.*, vol. 58, no. 9, pp. 3112–3121, Sep 2009. 1.2, 6.2, 6.3.1

[21] M. Sumner, B. Palethorpe, and D. W. P. Thomas: Impedance measurement for improved power quality Part 1: The measurement technique. *IEEE Trans. Power Delivery*, vol. 19, no. 3, pp. 1442–1448, Jul 2004. 1.2, 2.2.2.2, 6.3.1, 6.3.3

[22] W. Xu, E. E. Ahmed, X. Zhang and X. Liu: Measurement of network harmonic impedances:practical implementation issues and their solutions. *IEEE Trans. Power Delivery*, vol. 17, pp. 210–216, Jan 2002. 1.2, 6.3.1, 6.3.3

[23] M. Cespedes and J. Sun: Online grid impedance identification for adaptive control of grid connected inverters. In: *Proc. IEEE Energy Convers. Congr. Expo.*, pp. 914–921. Sep 2012. 1.2, 2.2.2.2, 6.3.1, 6.3.3

[24] T. Roinila, M. Vilkko and J. Sun: Online Grid Impedance Measurement Using Discrete Interval Binary Sequency Injection. *IEEE Journal of Emerging and Selected Topics in Power Electronics*, vol. 2, no. 4, pp. 985–993, Dec 2014. 1.2, 2.2.1.1, 2.2.3.4, 6.3.1

[25] M. Liserre, F. Blaabjerg and R. Teodorescu: Grid impedance detection via excitation of LCL-filter resonance. In: *Conf. Rec. 40th IEEE IAS Annu. Meeting*. 2005. 1.2, 6.3.1

[26] T. Roinila, M. Vilkko, and J. Sun: Broadband methods for online grid impedance measurement. In: *Proc. IEEE Energy Convers. Congr. Expo.*, pp. 3003–3010. Sep 2013. 1.2, 2.2.2.2, 2.2.3.3, 2.2.3.4, 6.3.1

[27] M. Nagpal, W. Xu, J. Sawada: Harmonic impedance measurement using three phase transients. *IEEE Trans. Power Delivery*, vol. 13, pp. 272–277, Jan 1998. 1.2

[28] R. Bhaskar, M. L. Crow, E. Ludwig, K. T. Erickson and K. S. Shah: Nonlinear parameter estimation of excitation systems. *IEEE Trans. Power Syst.*, vol. 15, no. 4, pp. 1225–1231, Nov 2000. 1.2, 2.2.3.3

[29] C. C. Brozio: *wideband Modelling and Parameter Estimation of Two-Winding Transformers*. PhD Thesis, University of Stellenbosch, 1999. 1.2

[30] P. T. M. Vaessen and E. Hanique: A New Frequency Response Analysis Method for Power Transformers. *IEEE Trans. on Power Delivery*, vol. 7, no. 1, pp. 384–391, Jan 1992. 1.2, 2.2.1.2, 2.2.2.2

[31] F. Ghassemi, P. Gale, T. Cumming and C. Coutts: Harmonic Voltage Measurements Using CVTs. *IEEE Trans. Power Del.,*, vol. 20, no. 1, pp. 1743–1749, Jan 2005. 1.2

[32] E. G. -Luna and others: Current status and future trends in frequency response analysis with transformer in service. *IEEE Trans. Power Del.*, vol. 28, no. 2, pp. 1024–1031, Apr 2013. 1.2, 2.2.1.1, 2.2.1.2, 2.2.2.2

[33] P. Mraz, P. Treyer, U. Hammer and S. Gonzalez: Innovative application of frequency response analysis for partial discharge measurement. In: *19th International Symposium on High Voltage Engineering*. Aug 2015. 1.2

[34] R. Pintelon and J. Schoukens: *System Identification: A Frequency Domain Approach*. New York: IEEE Press, 2001. 2.1, 2.1, 2.2.1.3, 2.2.2.1, 2.2.3.3, 2.2.4.1, 6.2

[35] B. Miao, R. Zane and D. Maksimović: System Identification of Power Converters With Digital Control Through Cross-Correlation Methods. *IEEE Trans. Power Electronics*, vol. 20, pp. 1093–1099, Sep 2005. 2.1

[36] A. A. Girgis and R. B. McManis: Frequency domain techniques for modeling distribution or transmission networks using capacitor switching induced transients. *IEEE Trans. Power Delivery*, vol. 4, pp. 1882–1890, Jul 1989. 2.1, 4.3.1, 6.3.1, 6.3.2.1, 6.3.2.1

[37] K. R. Godfrey, A. H. Tan, H. A. Barker and B. Chong: A survey of readily accessible perturbation signals for system identification in the frequency domain. *Control Engineering Practice*, vol. 13, pp. 1391–1402, Mar 2005. 2.1

[38] J. P. Rhode, A. W. Kelley and M. E. Baran: Complete Characterization of Utilization Voltage Power System Impedance Using Wideband Measurement. *IEEE Trans. Ind. Appl.*, vol. 33, pp. 1472–1479, Nov/Dec 1997. 2.2.1.1

[39] J. Bak-Jensen, B. Bak-Jensen, S. D. Mikkelsen: Detection of faults and ageing phenomena in transformers by transfer functions. *IEEE Trans. Power Delivery*, vol. 10, pp. 308–314, Jan 1995. 2.2.1.1, 2.2.1.2

[40] B. Gustavsen: Wide Band Modeling of Power Transformers. *IEEE Trans. Power Delivery*, vol. 19, pp. 414–422, Jan 2004. 2.2.1.1, 2.2.1.2

[41] C. C. Brozio and H. J. Vermeulen: *Off and Online Transformer Frequency Response Analysis Using PRBS Excitation*. Eskom Technology Group Research Interim Report TRR/E/98/EL074, Jul 1998. 2.2.2.2, 2.2.3.3

[42] R. N. Mutagi: Pseudo Noise Sequences for Engineers. *IEEE Electronics and Communication Engineering Journal*, vol. 47, Apr 1996. 2.2.3.3

[43] M. E. H. Amrani, R. M. Dowdeswell, P. A. Pazne and K. C. Persaud: Pseudorandom binary sequence interrogation technique for gas sensors. *Sensors and Actuators B*, vol. 47, pp. 118–124, 1998. 2.2.3.3, 2.1, 2.2.3.3

[44] S. W. Sung and J. H. Lee: Pseudo-random binary sequence design for finite impulse response identification. *Control Engineering Practice*, vol. 11, pp. 935–947, Sep 2002. 2.2.3.3

[45] T. Roinila and T. Messo: Online Grid-Impedance Measurement Using Ternary-Sequence Injection. *IEEE Trans. Ind. Appl.*, vol. 54, no. 5, pp. 5097–5103, Sep 2018. 2.2.3.3, 6.2

[46] A. H. Tan and K. R. Godfrey: The generation of binary and near binary pseudorandom signals: An overview. *IEEE Trans. Instrum. Meas.*, vol. 51, no. 4, pp. 583–588, Aug 2002. 2.2.3.3

[47] B. Peeters *et al*: Advanced shaker excitation signals for aerospace testing. In: *Proc. IMAC 29*. Feb 2011. 2.2.4.1

[48] H. Langkowski, M. Jordan, T. Do. Thanh and D. Schulz: Spectral Grid Impedance Identification on Different Voltage Levels-Challenges and Realization. In: *in 2017 IEEE Power and Energy Cociety General Meeting*. Jul 2017. 2.3, 2.3, 6.2

[49] M. S. Naidu and V. Kamaraju: *High Voltage Engineering*. New York: McGraw-Hill, 1995. 3.2.1

[50] B. Najafi and H. Hakim: A comparative study on nonparametric spectral estimators for application in machine vibration analysis. *Mechanical Systems and Signal Processing*, vol. 6, no. 6, pp. 551–574, Oct 1991. 4.3.1, 4.3.1

[51] B. P. Lathi and Z. Ding: *Modern Digital and Analog Communication Systems*. New York: Oxford University Press, 2010. 4.3.1, 6.4.3.2

[52] S. M. Kay: *Modern Spectral Estimation:Theory and Application*. Englewood Cliffs, New Jersey: Prentice Hall, 1988. 4.3.1

[53] P. Stoica and R. Moses: *Spectral Analysis of Signals*. Upper Saddle River, New Jersey: Prentice Hall, 2005. 4.3.1

[54] G. S. Miljković, I. S. Stojković and D. B. Denić: Generation and Application of Pseudorandom Binary Sequences using Virtual Instrumentation. *Automation Control and Robotics*, vol. 10, pp. 51–58, May 2011. 5.3.2

[55] ADVANTEST: DSP-Based Testing Fundamentals 50 PRBS (Pseudo Random Binary Sequency). 2013. 5.20

[56] SILICONLABS: 0.5 and 4.0 amp ISO drivers (2.5 and 5 kVrms). 2012. 5.3.3

[57] IXYS: IXGH24N170 Advance Technical Information. 2008. 5.3.3

[58] ONSemiconductor: RHRP30120 Data Sheet. 2017. 5.3.3

[59] L. Ljung: *System Identification: Theory for the User*. Upper Saddle River, NJ: Prentice-Hall, 1999. 6.2, 2, 4

[60] M. Sumner, B. Palethorpe, D. W. P. Thomas, P. Zanchetta and M. C. Di Piazza: A Technique for Power Supply Harmonic Impedance Estimation Using a Controlled Voltage Disturbance. *IEEE Trans. Power Electronics*, vol. 17, no. 2, pp. 207–215, Mar 2002. 6.3.1, 6.3.2.1, 6.3.2.1, 6.3.3

[61] K. O. H. Pedersen, A. H. Nielsen and N. K. Poulsen: Short-circuit impedance measurement. In: *IEE Proc.-Gener. Transm. Distrib.* March, 2003. 6.3.1

[62] U. Hassan and S. Anwar: Reducing noise by repetition:Introduction to signal averaging. *European Journal of Physics*, vol. 31, no. 3, pp. 453–465, Mar 2010. 6.3.5

[63] G. R. Walsh: *Methods of Optimization*. England: John Wiley and Sons, 1975. 6.4.3.5

[64] M. S. Bazaraa, H. D. Sherali and C. M. Shetty: *Nonlinear Programming: Theory and Algorithms*. LibreDigital, 2006. 6.4.3.5